Doctoral Dissertation

Doctoral Program in Mechanical Engineering (35^{th}cycle)

Modeling and investigation of thermal conductivity of GF nanocomposites by molecular dynamics simulation and micro-mechanics

By

Sajedeh Khosravani

******

Supervisors:

Prof. Erasmo Carrera

Prof. Mohammad Homayoune Sadr

Advisor:

Prof. Alfonso Pagani

Doctoral Examination Committee:

Prof. Maria Cinefra, Referee, Politecnico di Bari, Italy

Prof. Ali Moosavi, Referee, Sharif University of Technology, Iran

Prof. Roham Rafiee, Referee, University of Tehran, Iran

Prof. Aliasghar Katbab, Referee, Amirkabir University of Technology, Iran

Prof. Hamid Reza Ovesy, Referee, Amirkabir University of Technology, Iran

Politecnico di Torino

2023

Declaration

I hereby declare that, the contents and organization of this dissertation constitute my own original work and does not compromise in any way the rights of third parties, including those relating to the security of personal data.

Sajedeh Khosravani
2023

* This dissertation is presented in partial fulfillment of the requirements for **Ph.D. degree** in the Graduate School of Politecnico di Torino (ScuDo).

I would like to dedicate this dissertation to my beloved husband, Mani and my dear mom, Soori

Acknowledgements

I would like to express my special appreciation and thanks to my first supervisor, Professor Erasmo Carrera, who is a scientist with ethics who has ever cooperated with me throughout the Ph.D. duration. I would like to thank my second supervisor, Professor Mohammad Homayoune Sadr; you have been a tremendous mentor to me and supported me in the progress of the dissertation with your valuable guidance. I would also like to thank Professor Alfonso Pagani for his brilliant advice and comments. Your advice on both research as well as on my career has been priceless.

Abstract

In this study, firstly, the graphene foam (GF) and polymer composite structure have been produced in the laboratory. Raman spectroscopy and scanning electron microscope (SEM) images characterized the synthesized GFs structures. Then, using the results of SEM images, the polymer matrix and GF structure were simulated in the nanoscale by a new four-step method. Particularly, four types of GF with increasing mass density and decreasing porosity and three groups of polymers with different chain unit sizes have been investigated. Mechanical and thermal properties of GFs and polymer matrices have been calculated using molecular dynamics (MD) and developed codes. By simulating the tensile test by introducing different strain rates to the GFs, it was found that changes in the strain rate do not affect the value of their Young modulus. Non-equilibrium molecular dynamics (NEMD) method has been used to compute the thermal properties of GF groups and polymer matrices. The thermal conductivity (TC) amount has been investigated by defining the hot source and the cold sink on both sides of the simulation boxes. Thermoelastic properties were calculated as temperature dependent for all GF groups by MD platforms. Generally, GFs' coefficient of thermal expansion (CTE) increased with temperature and porosity percentage. By calculating the specific heat of GFs, it was discovered that the specific heat also increased as the temperature increased. By a slight change in mass density and percentage of porosity at the nanometer scale, significant changes occur in the Young modulus of GF samples, resulting in their mechanical and thermoelastic properties acting differently from each other. Furthermore, it was found that GFs with the highest porosity have the most significant specific surface area. The specific surface area decreases with decreasing porosity percentage. On the other hand, the TC of the PDMS matrix increased with the increasing number of chain units. Also, by reducing the percentage of porosity, GF's TC has improved significantly. It was found that two main factors affect the TC of GFs, the first factor being the number of foam connections and the second one being the presence

of defects. In fact, the groups of GF in this study with different connectivity and various defects show different TC values. Therefore, we can argue that the mass density (or pore size) and the number of defects in determining the TC almost cover each other. The effect of different potentials and the similarity of their results with experimental works were also investigated. It should be mentioned that although the simulated GFs with Tersoff potential have shown higher TC, the accuracy of Airebo potential was more elevated in considering all interatomic interactions in carbon atoms, so, Airebo's potential is preferred. Overall, GF's network structure creates an excellent TC while being lightweight and low-density, causing satisfactory heat transfer. A multiscale method has been used to calculate the mechanical and thermal properties of GF/Polymer composites. By considering repeating unit cells (RUC), for the first time, mechanics of structure genome (MSG) based on Carrera unified formulation (CUF) was used to calculate the effective properties of GF/polymer composites by using the properties of their components in the MD platform. Tensile testing highlights the effect of GF drying percentage on the composite and shows a 138% and 48% increase in the Young modulus and tensile strength compared to the neat polymer. After comparing the effective mechanical properties of composites with the multiscale method used in the present study, the method's accuracy was ensured. It was uncovered that the composite consisting of GF with the highest density and the lowest porosity has the lowest CTE. Also, the heat capacity of the composite depends not only on the heat capacity of the components but also on the Young modulus, CTE, and geometry. The effective TC of the composite is increased by expanding the chains of the polymer matrix and decreasing the porosity of the three-dimensional network of GF. It must be mentioned that GF's density can directly control the volume percentage of reinforcement in the composite. In GFs, due to lack of agglomeration, the TC increases with increasing volume fraction.

Contents

List of Figures

List of Tables

Chapter 1

Introduction

1.1 Introduction

In recent years, nanotechnology has become one of the most important research areas in new technologies. This knowledge explains the unique properties and behavior of particles smaller than 100 nm. Nanotechnology is the science of designing, manufacturing, and utilizing nanostructures or nanomaterials and examining the relationship between the various properties of materials (physical, chemical, mechanical, electrical, etc.). This knowledge, by using different sciences such as chemistry, physics, materials science, defense industry, biology, and engineering, follows four main objectives consisting of the synthesis of nanostructures, study of the relationship between material properties and their nanometer dimensions, design, and manufacture of nanodevices and design of new structures using nanomaterials. Therefore, considering nanomaterials' properties, the use of this technology has made research in nanotechnology a scientific and industrial challenge for researchers. A group of nanostructured materials that have great potential for use in various industries are nanocomposites. Nanocomposites are composite materials in which the dimensions of one of their components are in the nanometer range (1 to 100 nanometers). In other words, they are composites that retain their composite properties in dimensions below microns. It should be noted that adding singular nanoparticles to a field will not lead to extraordinary properties, but the composition must have special conditions. In the case of nanocomposites, a synergistic effect must be satisfied, and a bond must be established between the nanoparticles

and the matrix. The nanostructured phase used in nanocomposites can be made of zero-dimensional nanomaterials (such as quantum dots), one-dimensional (such as nanotubes and nanofilaments), two-dimensional (such as nanocoatings), and three-dimensional (such as Nanostructures). In general, nanocomposites can exhibit improved mechanical, electrical, optical, electrochemical, catalytic, and structural structures. Composites with different molecular arrangements, high specific contact surfaces, and high surface energy will experience much wider and newer applications. Recently, much attention has been paid to the use of graphene foam (GF) in various applications of technology, such as electrochemical storage devices, adsorbents, separators, and chemical sensors. Due to the combination of the properties of porous materials and two-dimensional graphene sheets, the amazing mechanical and thermal properties of three-dimensional GFs have attracted the attention of materials, metallurgy scientists and energy engineers. Graphene is known as an emerging two-dimensional nanomaterial for many applications. Assembling graphene sheets into three-dimensional structures is an attractive way to activate their macroscopic applications and preserve their components' exceptional mechanical and physical properties. Among the important properties of composites reinforced with GF, are high strength while low weight, high resistance to corrosion, and the property of radar waves, etc. This feature is used to build aircraft and submarines that cannot be detected by radar.

1.2 Problem Definition

Due to the amazing thermal properties of nanoparticles, these materials are in constant demand. Although nanocomposites made of two-dimensional graphene sheets have unique mechanical, thermal, and electrical properties compared to polymers, there are several major challenges in developing the application of this type of nanocomposite. Among these challenges, pointed to the irregular and uneven distribution of graphene sheets inside the resin and the accumulation of graphene sheets on the continuation and reduction of the modulus, strength, and thermal conductivity of the nanocomposite. There are solutions to solve these problems, which can be functionalized on the surface of graphene sheets or modified on the surface of graphene or polymer chains, which also changes their properties. But another solution scientists have developed is to put nanographene together to form a three-dimensional

graphene network in the form of graphene hydrogel, graphene aerogel or foam, and a thin-walled graphene film. Using GF and the electrical and mechanical properties of this type of graphene, research has been done in the form of experimental work, but there is a difference in the study of heat transfer in experimental, analytical, and numerical work. Also, some parameters' effects have not yet been discovered in experimental research. Therefore, the effective parameters in GF's mechanical, thermomechanical, and thermal behavior and how each parameter impacts their specific mechanisms for experimental work are still unknown. Given the complexities and experimental studies at the nanoscale, it provides simulation for selecting more attractive experimental options. Therefore, in this study, an attempt has been made first to calculate the mechanical and thermal properties of graphene foams and reinforced composites based on them using numerical methods. Then the effect of different parameters, including porosity percentage and length of polymer chains, on the effective mechanical and thermal properties will be done. All the calculations of this study are done using both nano and macro scales and using multi-scale methods.

1.3 Necessity of Research Fulfilment

Like many types of research that begin, construction methods are discussed first, then properties are investigated by experimental works, and finally, due to the high cost of experimental investigations, numerical modeling is used to determine its properties. In this study, it has been tried to use numerical methods with high accuracy and in accordance with experimental outputs in order to precisely investigate the properties of GF nanocomposites. One of the essential objectives of this research is to simulate GF in molecular dynamics (MD) platforms by selecting the potential in accordance with the laboratory data available in the references. In many cases, the results of numerical simulations do not fully comply with experimental methods. As of yet, little analysis has been done on the thermal properties of this particular type of nanocomposite. Some parameters are still not identified in experimental work because it is a complex and costly task. Hence, the primary purpose of this study is to investigate their properties with the least simplification compared to the laboratory model. Among the innovations of this research is the random structure of GF, which leads to variable pore size in each sample simulating the initial structure of GF, as well as obtaining the coefficient thermal conductivity (TC) of the polymer matrix

through MD. In this research, the mechanical and thermal properties of random GFs are calculated at the nanoscale using MD. Specifically, the performance of foams characterized by increasing mass density and decreasing pore size is investigated. The process of simulating three-dimensional graphene by developing python code and utilizing MD software, and examining their properties by considering the maximum and most consistent potential compared to the experimental model is accomplished in this research. The impact of effective parameters (temperature and sintering conditions), porosity percentage (increasing mass density and decreasing pore size), different chain units in a polymer matrix, and volume or weight ratio on the thermal conductivity of GF-reinforced polymer composites have been studied. The main challenge in this issue was first to randomly simulate the initial structure of GF in MD software by utilizing the scanning electron microscopy (SEM) image process from the synthesis of GF in this study. After that, the composite's effective properties were analyzed using the multi-scale method with high accuracy. Finally, a comparison between the results of MD and the micro-mechanical model with experimental works from this study and literature has been performed.

1.4 Purpose of Thesis

The main purpose of this dissertation is to calculate the thermal conductivity of GF/polymer composites. For this purpose, an efficient method has produced a repeating unit cell (RUC) consisting of porous GF and a polymeric matrix material. Atomic models have been selected in MD simulations to investigate GFs' mechanical and thermal behavior. Porous GFs have complex geometries formed by random networks of graphene nanosheets and polycrystalline grains. Therefore, producing their computational atomic models is a very challenging problem that must be solved to perform numerical experiments. Due to the lack of quantitative studies on the mechanics and thermomechanics of these materials in the literature, the other major goal of this study is to investigate the mechanical and thermomechanical behaviour of GF and GF/polymer composites. From this perspective, the ultimate goal of this dissertation is a deep understanding of the mechanisms of resizing and porosity of GFs on their properties. It is essential to have the necessary information about the dependence of mechanical, thermomechanical, and thermal performance on topological properties in order to produce outstanding new materials. It must be

mentioned in the scope of this dissertation experiments were performed to validate numerical mechanical properties.

1.5 Thesis Outline

This thesis consists of 8 chapters, the specific objectives and outline of each chapter are given below. The second chapter contains general thematic literature. This chapter covers the following topics: graphene, graphene oxide (GO), and their fabrication methods. As well as nanoporous materials and their properties, in addition to GFs and synthesis methods of these types of foams, also explanations about polymer nanocomposites are included in this chapter, too. The third chapter provides polymer nanocomposite modeling methods, which contain the role of computer simulation and essential tools in nanocomposite modeling. This chapter also expresses modeling techniques in continuum mechanics and classification atomic methods. Multiscale methods and repeating unit cells are also defined in this chapter. The fourth chapter has explained the MD simulation thoroughly and discussed the history and future of this simulation. In this chapter, the limitations of this simulation regarding using potentials and one of the most popular platforms of this simulation, namely LAMMPS software, have been scrutinized. The fifth chapter explains the micromechanical method used in this study. This chapter incorporates the mechanical, thermomechanical, and thermal equations of this method. The sixth chapter incorporates the experimental synthesis methods of GFs and GF/polymer composites. The required materials and the GF/polymer composites fabrication method are described in detail in this chapter. The seventh chapter of the simulation algorithm of GFs and PDMS has been investigated in MD software. This part fully explains the method of calculating mechanical and thermal properties. The eighth chapter includes the results and discussion of experimental outputs and numerical calculations for mechanical properties, thermomechanical properties, and thermal properties, respectively, of GFs and GF/polymer composites. Finally, a summary conclusion and suggestions have been proposed.

Chapter 2

Overview

2.1 Introduction

Nanoscience and nanotechnology deal with very small scales that can be applied to all disciplines such as chemistry, physics, materials science, and engineering. Nanotechnology uses nanoscience to control nanostructured phenomena to achieve a targeted goal. Exciting and highly accelerated advances in nanoscience have been made due to the ability to control and observe structures on very small and short-time scales and highly developed computational capabilities. In many technology fields, nanomaterial science is a fundamental block to further advances and innovations. In particular, the mechanics of nanostructured materials is an important area to be understood due to the fact that many nanoscale phenomena are controlled. Nanomaterials consisting of structural elements in the range of 1 to 100 nanometers such as particles, tubes, fibers, or rods of nanoscale can be considered the main nanotechnology products. One of the main reasons for the great interest in these materials in the academic and industrial environment in recent years is mainly due to the incredible diversity of properties observed in the continuous and nanoscale. Due to these attractive properties, nanomaterials have great potential to create effects in many fields, such as aerospace, medicine, electronics, etc. While some nanomaterials are naturally occurring, many nanomaterials can be classified as engineered nanomaterials designed for production and are currently being processed for commercial use. Many examples of nanomaterials in cosmetics, sports goods, clothes resistant to stains and cold, tires, electronics, and many other items that are used in daily

life [9]. In addition, nanomaterials are used for imaging, drug delivery, and diagnostic purposes for medical applications. Engineered nanomaterials are materials designed and manipulated at the nanoscale to acquire new properties compared to their counterparts. Two main reasons can explain the different properties observed in nanomaterials designed at the molecular level. One of these is the dramatic increase in surface area due to at least one nanoscale dimension in the nanomaterial topology. Increasing the surface area causes chemical reactivity of structures, which affects materials' mechanical, electrical, and thermal behaviour. Another reason that can be used to explain scale-dependent behaviour is the quantum effect. At the atomic level, quantum effects play a much more critical role in nanomaterials' optical, electrical, mechanical, and magnetic behaviour. Basic properties of materials such as Young's modulus are measured using macro-scale or, recently, micro-scale experimental specimens that provide no nanoscale information. Recently, the appearance of nanomaterials in the commercial arena has been increasing. In addition, the range of products available covers a wide range of different areas. Nanomaterials can be found in cosmetics, self-cleaning glass, wrinkle-free or stain-resistant textiles, and many other applications. For example, new UV barrier coatings are used on glass bottles to prevent sunlight damage to beverages. The surface-to-volume ratio of nanoparticles leads to remarkable improvements in chemical catalysis. The range of applications of nanoparticles in catalysis is vast, from fuel cell applications to catalytic converters and photocatalytic devices [10]. The popularity of nanophase ceramics is mainly due to their higher ductility at high temperatures compared to coarse-grained ceramics. Metal nanopowders are used to produce porous coatings and anti-gaseous materials [11]. They are also good candidates for bonding metals due to their high-value cold weld properties in addition to their elasticity. With the uninterrupted advancement in nanotechnology, nanostructured applications that enable mechanical, electrical, magnetic, optical, and electronic functions have increased. As mentioned, nanoscale materials are structurally organized with at least one dimension less than 100 nanometers. Nanomaterials can be classified based on the number of nanoparticles that make up the nanostructure. In this regard, nanostructures such as nanofilms and nanowires are organized into one-dimensional nanomaterials. Nanotubes or fibers are examples of nanostructures in two dimensions. Similarly, nanoparticles, quantum dots, and fullerenes have nanostructures in all three dimensions [12]. Fig. 2.1 provides some illustrative examples for dimensional classification. With all of this in mind, nanomaterials can be single, melted, or agglomerated in various forms,

such as spherical, tubular, or irregular. The classification of nanomaterials can also be done based on the phase composition of the nanomaterials. Single-phase materials are composed of only one element, such as crystalline or amorphous particles [13]. However, multiphase or hybrid nanomaterials are formed by more than one unit, such as nanocomposites or coated particles. As the study by Katbab et al. [14] showed that adding carbon black and graphite layers controlled the conductivity network and electronic properties of silicone rubber-based composites.

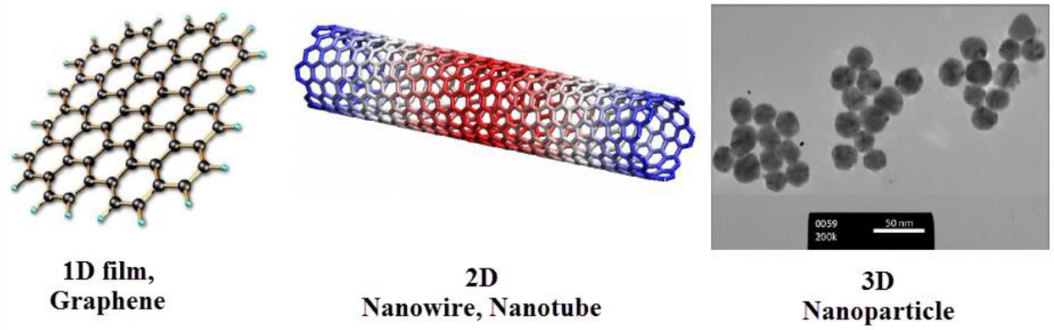

Fig. 2.1 Classification of nanomaterials [1].

2.2 Graphene

Carbon atoms are the building blocks of many chemicals and are the basis of various technologies. Carbon atoms have an electronic structure of $1s^2/\ 2s^2\ 2p^2$ in terms of the order in which the orbitals fill. Therefore, they have 4 free electrons in their last layer, which allows the conversion of four bonds for these atoms. The bonds that these atoms form are seen in different forms in different compounds and therefore create different properties. In a graphene sheet about one atom thick, each carbon atom is bonded to two other carbon atoms. These three bonds are on the same plane, and the angles between them are equal to 120 degrees. In this case, the carbon atoms are placed in a position that forms a network of regular hexagons. Of course, this is the most ideal form of a graphene sheet. Sometimes the shape of this sheet changes to form pentagons and hexagons.

In a graphene sheet, each carbon atom has an off-plane bond. This bond is a good place for some functional groups as well as hydrogen atoms. The bond between the carbon atoms here is covalent and very strong. Graphite is a layered crystal lattice

structure formed by stacking parallel two-dimensional graphene sheets, as shown in Fig. 2.2. Graphene sheets are held together in graphite by weak van der Waals forces with a distance of 0.335 nm. The P_z orbitals of the carbon atoms overlap best when they are parallel. Therefore, the graphene sheet has the lowest energy when it is completely flat. The π orbital is distributed all over the graphene sheet and causes its thermal and electrical conductivity.

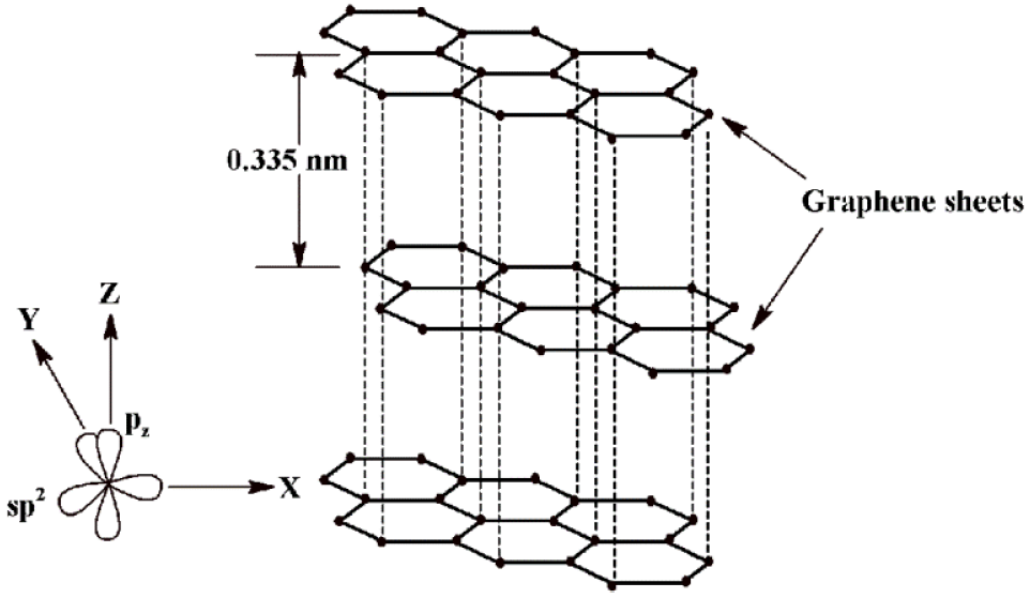

Fig. 2.2 The layered structure of graphite whose carbon atoms are tightly connected in hexagonal rings.

Due to the high mechanical, thermal and electrical properties of two-dimensional graphene, and also due to its Young modulus and tensile properties, it is widely used in the reinforcement of composites and nanocomposites [15].

2.3 Graphene oxide

Graphene oxide (GO) is the favorably oxidized product of graphene possessing different oxygen-including functional groups such as carbonyl, epoxy, hydroxyl, and carboxyl. These groups, located on both the edge and basal plane of the nanosheets, shown in Fig. 2.3, schematically convert the sp^2-bonded graphene network to a mix of sp^2 and sp^3 hybridized carbon. It should be mentioned that there is no

definitive structure of GO and this figure only is an example. These introduced sp^3 defect zones deform the inherent conjugated π system and overall strength and conductivity. Regardless, these groups make graphene oxide positively attractive as a multifunctional material for many applications, as it can be easily adjusted with multiple functional groups [16].

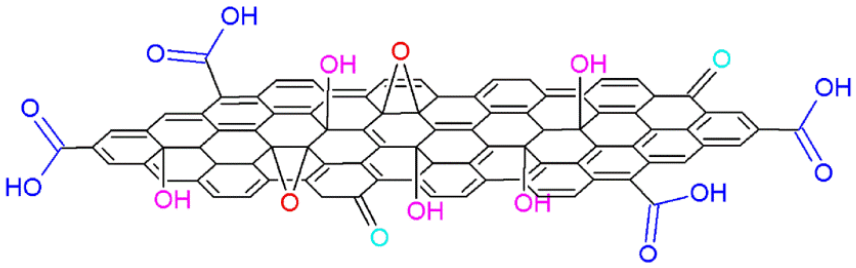

Fig. 2.3 Schematic structure of graphene oxide.

2.4 Synthesis Methods of Graphene and Graphene Oxide

There are several methods for producing graphene, the common principle of some of which is to eliminate the force between the graphene plates in the graphite and to separate them to achieve single layers of graphene or graphene oxide (such as peeling off a large piece of rock to achieve a small sculpture) which is called the top-down method, a number of other methods are based on stacking carbon atoms one by one (such as building a wall by putting bricks together), are also called bottom-up methods. Today, a wide variety of methods are used to make graphene, the most common of which are micromechanical scaling methods, growth on metals methods, chemical vapor reduction, and chemical methods. Some other methods, such as splitting carbon nanotubes, have recently been used to produce graphene-shaped nanofibers and to fabricate them with microwaves [17].

Flake graphite is the most common source of graphite used for oxidation, which contains numerous localized defects. However, the precise and clear explanation of the oxidation mechanism is an ongoing challenge due to the complexity of graphite and its intrinsic defects. Fig. 2.4 shows the schematic illustration of GO synthesis. The exact chemical structures of GO differ mainly due to the complexity of the

material and its amorphous nature. Despite these obstacles, several structural models have been presented to understand the structure of GO, which mostly includes the topic of the chemistry of materials, which is out of the scope of this research, but for more information, can refer to the reference of [18].

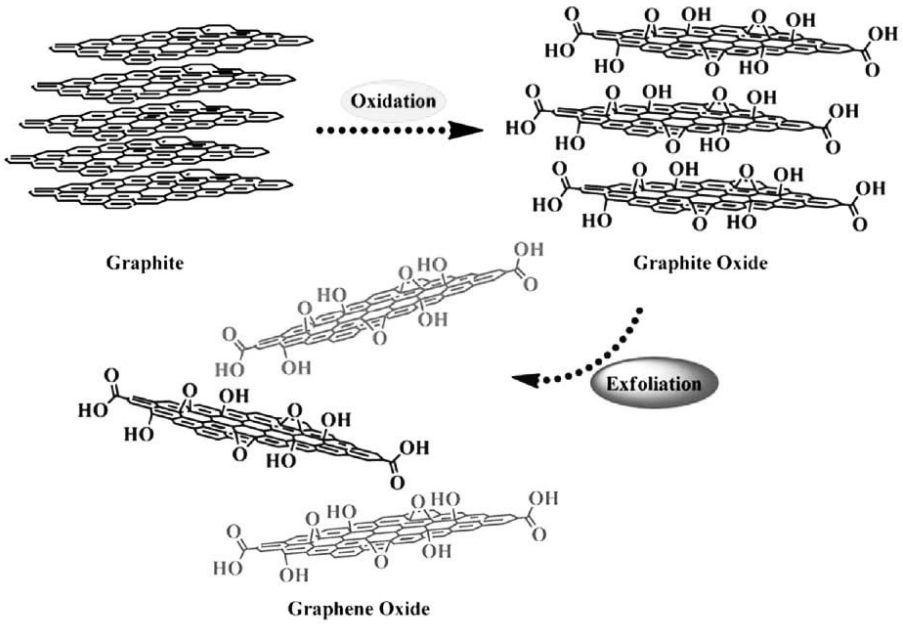

Fig. 2.4 Synthesis of graphene oxide.

2.5 Nanoporous Materials

Nanoporous materials are generally identified as nanoscale solids that contain a porous topology at longitudinal scales of less than 1 μm [19]. Materials classified as nanoporous materials are composed of nanoscale cellular structures through which there are open channels or cavities that directly affect the behavior of materials. Large amounts of nanoporous materials are present in nature, especially in biological systems and minerals. For example, biologically living cell walls are a type of nanoporous membrane that has significant complexities due to its responsibilities in living organisms. With advances in nanotechnology for manipulating and visualizing objects at the nanoscale, the ability to control the pore size of these materials at the nanoscale has increased. Since the size and composition of the nanoporous structure can be changed, its physical and chemical properties can also be changed.

Nanoporous materials show different functionalities according to the properties of nanopores such as their shapes, sizes, and amounts. Pores are defined as voids or holes with different shapes (e.g., cylinders, balls, slits, hexagons, spheres, etc.) in a solid material. Pores may exist as isolated cells or interconnected with each other through holes in the cell walls. The pores inside a porous material can be open or closed. Open pores are a network of interconnected pores, but in the case of a closed pore system, the pores are not interconnected. Therefore, in applications such as catalysis, filtration, and adsorption, porous materials with an open-pore shape are much more desirable. On the other hand, closed pore systems are preferred in light and heat insulation or lightweight structural applications. In general, the morphology of nanoporous materials can be simplified to defined geometries, such as a cylindrical hole, in order to perform a simplified analysis. According to the size of the holes throughout the porous network, if the hole diameter is less than 2 nm, the porous material can be classified as microporous. It is mesoporous if the hole diameter is between 2 and 50 nm. And if the diameter is larger than 50 nm, it is large porous [20]. This classification was developed by the International Union of Pure and Applied Chemistry (IUPAC) to reach an agreement on the category of pores. Fig. 2.5 shows some models related to this classification.

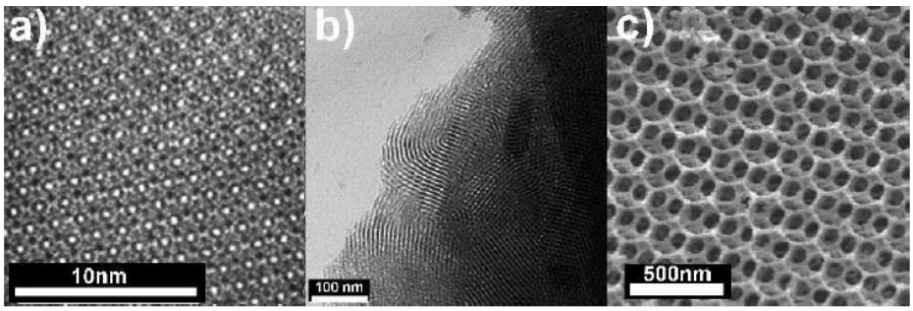

Fig. 2.5 Silica nanoporous materials in three different types. (a) A microporous material: zeolite, (b) A mesoporous material, (c) A macroporous material [2].

2.5.1 Properties of Nanoporous Materials

Due to the new structural properties and interconnected surface at the atomic scale, the use of nanoporous materials as energy storage and adsorption medium is increasing day by day. In addition, porous materials are of considerable importance in nanoscience and nanotechnology due to their adsorption capacity and interaction

with atoms and molecules [21]. The basic properties of nanoporous materials can be depicted as long as their microscale properties are understood. In this regard, atomic simulations such as molecular dynamics simulations play an important role in supporting experimental studies. As the porosity, pore size, pore size distribution, and composition of nanoporous materials vary, so do the properties of the pores and their surface area, which changes their applications. For example, to be a good adsorbent, it must have high adsorption capacity, selectivity, good mechanical properties, and acceptable stability and durability. High adsorption capacity is mainly due to the characteristics of the specific surface area, surface chemistry, and pore size. Similarly, the selectivity required to separate the desired material from a multicomponent mixture and the type of adsorbent strongly depends on the pore size, shape, and pore size distribution. Another required feature is excellent mechanical properties that help the adsorbents withstand wear, erosion, and crushing. In addition, due to the abrasive chemical and thermal environments, the stability and durability of the adsorbents are critical to their long-term performance. Numerous factors affect the degree to which these requirements are met for nanomaterials, such as manufacturing methods and conditions, material morphology, etc. The three-dimensional network structure of nanoporous materials provides a suitable environment for selecting and separating different types of molecules. One of the most important characteristics of nanoporous materials is their very large surface area, which is frequently mentioned in the text. Such a large surface makes it highly sensitive to changes in environmental conditions such as temperature, light, and humidity. Due to this advantage, nanoporous materials are widely used as sensors and actuators.

2.5.2 Graphene Foam

Graphene foam (GF) is one of the carbon foam structures that consists of several nano-shaped plates of graphene and a large number of cavities are formed in its connection structure [22]. While the thickness of the graphene layers plays an important role in its properties, the use of graphene in the macro dimension is always a challenge, to do so they turn the graphene into a three-dimensional state to avoid problems in the macro dimension. To convert two-dimensional graphene to a porous structure and macroscopic three-dimensional layers are presented, which will be explained later. The most important properties of GF are energy storage, catalysts, absorption systems, lithium batteries, fuel cells, separating filters, etc.[23]. In the

aspect of separation by nanofoams, Moosavi et al. [24] simulated a single-layer graphene nanofoam to separate salt from the sea using MD. They investigated the effects of pressure and size of foam nanopores on desalination performance. The results show that increasing the pressure and diameter applied in the nano-cavities increases the water flow through the membrane while the salt rejection decreases. Graphene is ideally a completely two-dimensional, single-layer nanostructured structure of carbon atoms bonded together by covalent bonds to form a perfectly flat hexagonal lattice. In practice, achieving such a structure is complicated for two reasons: The first reason is that it is very difficult to control the conditions for separating a single layer of graphene. Usually, a preparation called graphene consists of sets of several layers of graphene, each containing a different number of plates. Another reason is that graphene does not have a perfectly flat atomic structure; graphene plates are flexible, that is, they bend or wavy [25]. Fig. 2.6 shows the different types of carbon-based nanomaterials [26]. As mentioned in the first part of the introduction, the carbon atom has different deformations that these properties transfer properties to the carbon atom. One of these properties is the presence of hollow structures in the carbon atom [27]. Among all the geometries of carbon atoms, such as fibrous, spherical and angular, the carbon foam model has a better and more cohesive structure. Due to its cellular structure, this material has unique properties such as surface increase, which is accompanied by the basic characteristic of carbon properties, very light weight, high temperature stability, real hydrophobic surface, high thermal resistance, excellent electrical conductivity, etc. In the bulk property of carbon, mechanical and electrical properties can be changed by changing the structure of this material from graphite to amorphous or to a directional property. In carbon foam, properties can be changed by changing the cell structure [28].

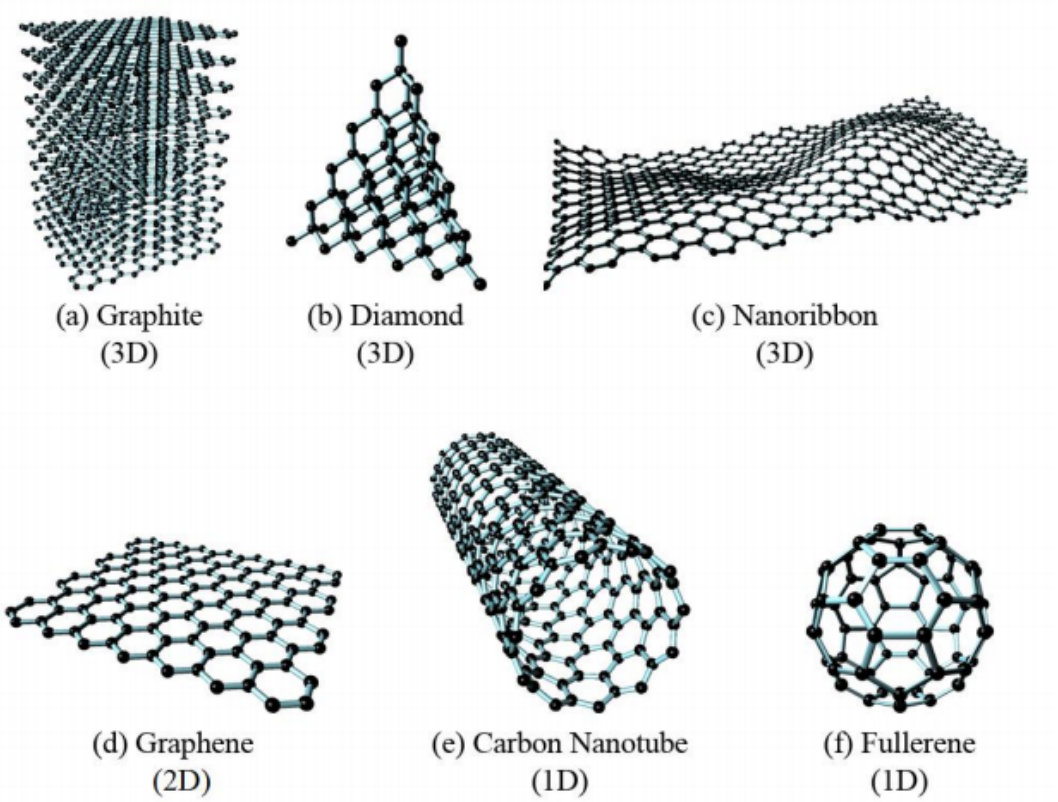

Fig. 2.6 Carbon-based nanomaterials [1].

2.5.3 Graphene Foam Synthesis Methods

As mentioned, there are different manufacturing methods for creating the structure of GF, each method creates different properties of GF according to the specific conditions that are considered. The structures used to make graphene are available in the form of graphene oxide foam, aerogel GF, polycaprolactone copolymer GF, continuous porous graphene oxide model, and graphene oxide porosity reduction model. It creates something different. For example, the heat reduction method creates a more compact porous structure than the chemical deposition method. These structures change the properties of GF material and if the properties of this material are obtained according to experimental works, of course, different results will be obtained [29]. There are several manufacturing methods for making GF. The most famous method for producing GF is chemical vapor deposition. Trinsoutrot et al. [30] first produced this structure on nickel foam in 2014; of course, graphene can

be grown on the GF itself, and another structure can be created. In addition to the chemical deposition method, other fabrication methods are used, such as the heat axis pattern. In this method, materials such as polystyrene, silica, and hexane are used as samples, and the process of thermal reduction leads to the production of this structure [31]. To date, several different methods for assembling graphene sheets into porous and layered three-dimensional structures have been identified, including direct current assembly [32]. The exploitation of graphene-based materials faces an important scientific and technical challenge. Like other polymeric or molecular materials, the performance of graphene-based materials is strongly influenced by the arrangement of the individual sheets. Due to the van der Waals attraction and agglomeration inevitably occurs in graphene [23]. As a result, many of the unique properties of graphene, such as high specific gravity and specific electron current behavior, were significantly compromised or not even available in a set. The performance of graphene films has not yet been significantly improved to compete with porous carbon materials for large-scale use in energy storage devices. It is worth noting that graphite is an assembly of graphene, but due to the density of its layers, it lacks many of the attractive features of separate sheets of graphene. Preventing graphene layers from clumping during fabrication. It is essential that separate sheets in multilayer graphene structures act as graphene, not graphite. Layered dispersion method, chemical graphene dispersion method is prepared by chemical reduction of graphene oxide solution obtained by chemical oxidation and peeling of natural graphite. Direct pattern method and 3D printing method, among which, the 3D printing method is more reliable in terms of preparing large-scale graphene [33]. In laboratory methods of synthesis graphene hydrogel and GF, the common principle in the production of graphene is to eliminate the force between the graphene plates in the graphite and to separate them to achieve the graphene and graphene oxide monolayers. Graphene oxide is converted to graphene hydrogel using one of the reducing agents, such as hydroxide acid, paraffin diamine, ethylenediamine, and ascorbic acid and then cooled in a freezer and converted to graphene aerogel or GF [5].

2.6 Polymer Nanocomposites

Nanocomposites are composite materials whose dimensions of one of their components are in the range of nanometers (1 to 100 nm); or other words, this composite maintains its properties in sub-micron dimensions. The need to reduce fuel consumption due to economic justifications in various fields has increased the demand for new and lightweight materials such as polymers. But on the other hand, due to the lower strength of polymers compared to metals, their reinforcement seems necessary. Reinforcement of polymers with conventional materials damages the two main properties of polymers, namely lightness and ease of processing. Therefore, in recent research, small amounts (less than 10% by weight) of nanoparticles are used as reinforcers in polymers. Nylon 6 was the first polymer used by Toyota in 1990 to make nanocomposites, but today thermoset polymers such as epoxy, polyamide, and thermoplastic polymers such as polypropylene and polystyrene are used as the base material for these composites. These types of composites consist of a polymer resin (large molecule reinforced plastic) as a base and filaments as a reinforcing agent. The characteristics of this group of composites are diverse and wide application, good properties at ambient temperature, ease of construction, and low cost. An important issue in polymer nanocomposites is the uniform phase distribution of the nanometer amplifier in the polymer field. The surface activity and material of nanometer particles used in polymers should be such that the rate of polymerization and the starting point of polymerization can be controlled because, during polymerization, the reinforcing nanometer elements may become lumps, which means creating a heterogeneous nanocomposite. In most cases, the properties will be severely reduced. Many efforts are now being made to facilitate the distribution of nanoparticles and make them uniform. Fig. 2.7 shows the schematic steps of preparing polymer/nanoporous materials composite [34].

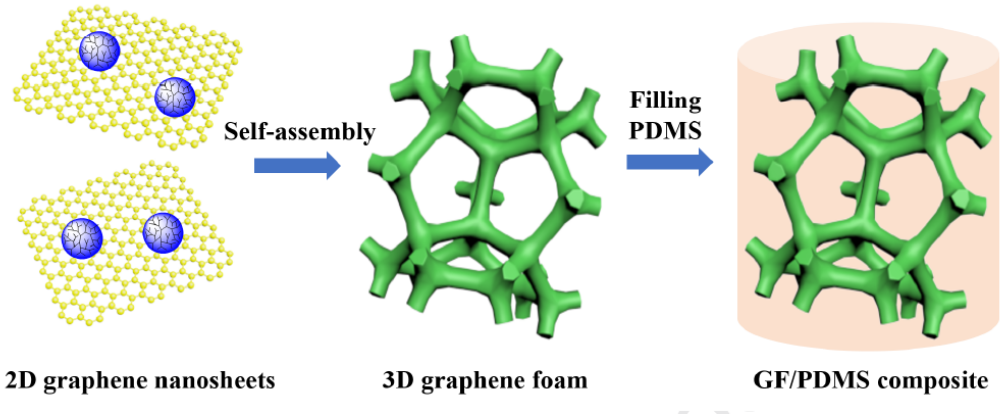

Fig. 2.7 Schematic steps of preparing polymer/GF composite.

The effect of the intermediate phase in the presence of nanoparticles on the properties of nanocomposites is significant. Nanoparticles in the form of perturbations in the polymer cause the intermediate phase, due to which they change the overall properties of the system dramatically. Determining the exact thickness of the middle layer is a complex and controversial task that, according to experimental, the properties of the middle layer are different from the matrix and cause the properties of the composite to change. Nanoparticles are mainly used as reinforcing materials in nanocomposites; adding nanoparticles increases and improves the properties of the base material.

Chapter 3

Modeling Methods of Polymer Nanocomposites

3.1 Introduction

Considering the hierarchical structure of nanocomposites, determining the properties of nanocomposites is one of the challenging issues of the present era. There are new methods in the field of modeling and determining the properties of these materials. This section examines some important issues related to the modeling of nanocomposites and the classification of modeling methods.

3.2 The Role of Computer Simulations

Simulation is a calculation process based on predetermined laws (physical-chemical). In physics, we sometimes come across problems with a large number of particles that we know the governing differential equation for and want to solve. As we know, it is analytically impossible to solve several equations with multiple equations and multiple unknowns, and on the other hand, solving them numerically is complex, and one must use Newton-Raphson-like algorithms, which require the inversion of a large matrix at each step, which is undoubtedly necessary It is exceptionally high computational volume. In such cases, instead of a numerical solution, simulation is the best option. So, having the initial conditions, we move on to the differential

equations and, at the same time, developments to get the solution to the problem. One of the advantages of issues of this type, which are known as particle problems, is that the answers obtained from the simulation are independent of the initial conditions, and after a while, the system forgets its initial conditions, which means that any specific solution can be found in such problems.

3.3 Some Important Issues in Nanocomposite Modeling

- Agglomeration
  Experimental evidence shows that one of the main limitations in the full utilization of the structural and functional properties of nanocomposites is the density of nanofillers, which reduces the high density of charge transfer particles from the matrix to nanoparticle fillers, which will affect all properties.

- Morphology
  The properties of polymer nanocomposites are highly dependent on their morphology. For example, in the fabrication of silicate polymer nanocomposites, three different thermodynamic morphologies are obtained, which depend on the interactions of the polymer matrix and silica layers, the volume fraction of the fillers. Macroscopic properties are greatly influenced by morphology, so modeling is essential. On the other hand, evidence is needed to investigate the effect of factors such as porosity (increasing mass density and decreasing pore size), aspect ratio, distribution of nanoparticles within the polymer matrix, and volume or weight ratio on properties.

- Interface
  In order to obtain the effect of the intermediate phase (interface) between the matrix and the fillers, an accurate and enlightening study at the molecular level will be needed because laboratory research in the nanoscale is difficult in this case. As a result, other methods are needed for an investigation. It should be acknowledged that by predicting surface features, the effect of molecular and supramolecular interactions of particles can be determined [35]. Molecular analysis can be a suitable candidate for this topic from nano to micro scale.

3.4 Simulation Techniques and Strategies

The methods based on material continuity include the following techniques for composite materials:

- Finite element method (FEM)
- Boundary element method (BEM)
- Developed micromechanical method

Computational chemistry methods in which the laws of continuum mechanics are not valid include the following techniques:

- Molecular mechanics
- Molecular dynamics

And modeling strategies include:

- Nanostructure strategy
  This strategy is an attempt to consider the morphology of nanofillers at the nanoscale, where continuity is assumed. An advantage of nanostructure modeling compared to microstructure is that in this method, a more accurate and precise analysis of matrix and fiber interactions is considered. As a result, this method shows a more realistic model. Molecular properties are not considered here, so there are no molecular interactions.
- Molecular strategy
  Molecular modeling is created by combining three models: micromechanical, nanostructure, and molecular. Molecular dynamics is an example of this type of strategy. This method requires high computing power to consider physical and chemical interactions. This method is based on the structure of the unit cell and equivalent chain cell, and the initial equilibrium conditions are determined through molecular dynamics.
- Micromechanical strategy
  Micromechanical strategy is a method of determining the properties of composite materials by analyzing their components. Micromechanical methods are

used to evaluate the properties of composite materials based on the properties of their components. In this method, chemical and physical interactions between the matrix and nanoparticles are not considered, but the effects related to the nano component are considered.

High-effective properties polymer composites are commonly used in various industries for structural applications, renewable energy systems and electronic systems. Due to the low thermal conductivity (TC) of polymers, the placement of particles with extremely high TC in the polymer matrix makes it possible to make composites with high effective TC. In this study, the properties of the composite is the same as the effective properties of the composite. Mechanical and TC in recent years has been calculated using two powerful tools. That is, atomic methods are referred to here as molecular dynamics methods and analytical methods as micromechanical models. The properties of polymer composites is determined by several factors, including particle and matrix properties and microscopic structures [36]. To understand the effect of these factors on the TC of polymer composites, modeling methods are powerful tools. Modeling methods can be used in conjunction with experimental data to quantitatively and qualitatively analyze the composite. Here, first, the classical theoretical models of TC for polymer composites are introduced. Then, new simulations models are described. The theoretical modeling method can describe heat transfer mechanisms while the simulation method can accurately describe the properties of microstructures.

3.5 Classical Theoretical Models

The classical theoretical model for composites is divided into two main categories:

- Effective Medium Approximation
- Micromechanical method

The Effective Medium Approximation model is the Maxwell-Garnett model [37], which is suitable for subtracting low volumes of particles or particles that are spaced apart. Fricke's model [38] extended Maxwell's model with elliptical particles. Many researchers have developed the Maxwell model, such as Hasselman [39] which took

into account the effect of interface and particle size. The improved Brugman model of the Maxwell model is obtained by adding the effect of thermal interaction, which is applicable for a higher volume fraction. Then, according to Bergman's model, the effect of thermal resistance between the particle and the matrix, which is its symbol, is considered [40]. Bergmann's model is more suitable for complex composites when the composites are two-stage. Also known as a three-dimensional block structure. The relationship diagram of classical theoretical models is shown in Fig. 3.1 [37].

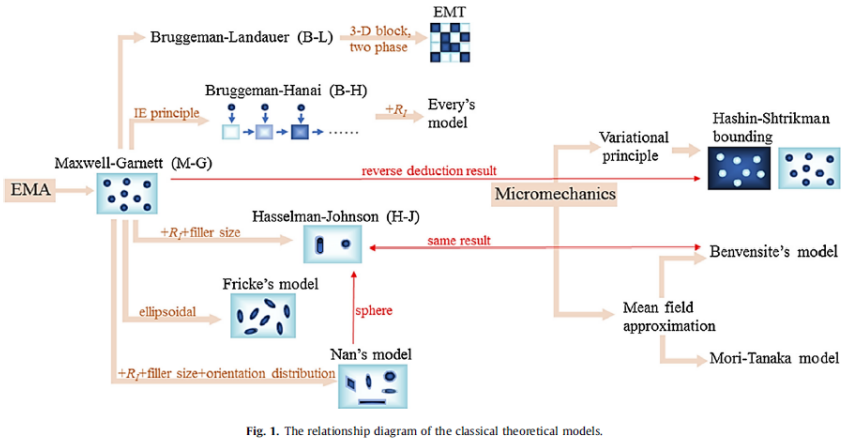

Fig. 1. The relationship diagram of the classical theoretical models.

Fig. 3.1 The relationship diagram of classical theoretical models

3.6 Computational Continuum Modeling

Computational continuum modeling includes FEM and BEM. Although these methods do not give a completely accurate answer, they can provide high-precision estimates for a wide range of hypotheses.

3.6.1 The Finite Element Method

The FEM can be used to numerically calculate the properties of a large volume of material based on geometry, properties, and volume fraction. FEM divides the material into representative volume elements (RVE) to determine the range of stress and strain. The size of the analysis and the element type determine the solution's accuracy. RVE in the nanoscale with different shapes is used to simulate the properties. However, the high complexity of the model, expensive software,

and time-consuming simulation limit the use of this method. The finite element micromechanical method is widely used to predict the properties of nanostructured composites. Li et al. used the FEM to show the stress concentration at the end of nanotubes, and matrix [41]. Zhang et al. investigated the thermal behavior of polymer composite filled with GF, and the effect of their contact thermal resistance using the FEM [42]. Chen and his colleagues used different shapes of the representative volume element to understand the material properties[43]. One of the concepts of particular importance in computational mechanics and modeling issues today is the volume representative element. This concept plays a fundamental role in modeling in different structural parts, especially in modeling composites and nanocomposites.

3.6.2 The Boundary Element Method

The BEM is a continuous mechanical method that includes solving boundary integral equations to evaluate the stress-strain range. In this method, the elements are used only on the boundaries (unlike the FEM, where the elements cover the entire volume). Therefore, BEM has fewer calculations than the FEM. BEM can be used from micro to macro scale modeling. Also, this method assumes continuity of matter, and the details of molecular structure and atomic interaction are ignored [44].

3.7 Classification of Atomistic Method

Atomistic methods can be divided into two categories:

- Classical methods
- Quantum methods

Among the classical methods, molecular dynamics and coarse grain simulation methods can be mentioned, both of which follow the same logic and are the target of this research. In the following, this method will be explained in detail. Among the quantum methods, we can mention the density functional theory (DFT) methods and Ab initio quantum chemistry methods, which are limited to investigating properties in the picosecond time range and angstrom size, so currently, these methods are primarily used in studies related to electronic and phononic properties. The DFT

method is a theory in the framework of quantum mechanics used to investigate the electronic structure of materials in systems that consist of more than one particle. In this theory, explaining phenomena such as intermolecular forces, especially the van der Waals force, the forbidden band in semiconductors, charge transfer in an excited state, etc., is not completely possible with this method. The term ab initio, which means from the beginning, was first used in quantum chemistry by Robert Parr and his assistants in a quasi-practical study of the excited states of gasoline [45].

3.8 Multi-scale Method

The multiscale model creates different temporal scales and different dimensional scales through a combination of different methods. Some researchers have combined micro and macro scales, and some have combined nano and micro scales and used their study to obtain properties. Clancy et al. [46] used a multiscale model to estimate the thermal resistance between nanoparticles and a polymer matrix. Tang et al. [47] investigated the effect of hydrocarbon chain application on the thermal resistance between graphene and the matrix using a compact multidimensional model based on the theoretical model. The effect of bond density on the TC of graphene and composite was also considered. Rafiee et al. [48] have also used a computational multiscale hierarchical approach to determine the elastic response of polymer composites based on an innovative filler consisting of nanoporous alumina powder on a micro-scale. For this, they have used the concept of RVE at the micro-scale in two stages using FEM and then at the macro scale using a combination of micromechanical laws. A multidimensional model has been developed by Mortazavi et al. [49] to study TC. In this model, the TC of expanded graphite is obtained by simulating molecular dynamics, and the TC of the composite is calculated by FEM of a volumetric representative element.

3.9 Repeating Unit Cell

The Repeating unit cell (RUC) plays the main role in determining the effective properties of composite materials according to its predictions. Numerical homogenization provides accurate estimates of the effective properties of composite materials when

combined with RUC. In computational homogenization, RUC refers to a collection of random material volumes that, by an averaging method, represent the effective material properties within a specified tolerance. In this study, the ability to define an RUC, the same as the RVE in literature, is used to obtain accurate, effective properties. Simulations of composite materials in macroscopic sizes require ultra-advanced computing servers to obtain their properties. Therefore, with the RUC definition, the computational volume with high accuracy is greatly reduced. The volume of RUC is placed under periodic boundary conditions. Here, the RUC has been determined based on the data obtained from the experimental section in unit dimensions.

Chapter 4

Molecular Dynamics Simulation

4.1 Overview of Molecular Dynamics Simulation

As mentioned in previous chapters, in this dissertation, molecular dynamics (MD) simulation is used to investigate the mechanical, thermomechanical, and thermal behavior of graphene nanofoams. In this regard, this section provides an overview of the MD method and related topics. Numerical experiments, that is, computer simulations, are today important tools in advancing scientific research and development. In the past, real experiments and theoretical work were the main frameworks for the advancement of science. In an experimental study, the system under study is subject to certain boundary conditions and the desired parameters are measured and stored numerically. In a theoretical work, a physical system with governing mathematical equations consisting of system drive parameters is represented. In order to validate the mathematical model formed in the theoretical study, the stability or predictive capacity of the model must be demonstrated by a few simple cases that make solvable mathematical equations possible. However, to obtain solvable mathematical equations, simplistic assumptions are often used to eliminate system complexities that take us away from real-world problems. Previously, theoretical models could only be considered in limited cases. In addition to experiments and theoretical studies, high-speed computers that appeared in the 1950s introduced a new method, numerical experiments, in the field of scientific research. In numerical experiments, or computer simulations, there is still a theoretical model that controls the simulation, but calculations are performed numerically by high-speed computers

within the framework of algorithms developed in a suitable computer language. With numerical experiments, much more complex phenomena can be injected into the numerical system, which leads to the study of more realistic systems. Numerical simulations are conceptually in a position between experiment and theory. On the other hand, the validation of a numerical model is more like a real physical experiment in the method of evaluating simulation results, which conveys the concept of computer simulation to experiments. The MD method is a computer simulation method for obtaining the time paths of a set of atoms that interact numerically by solving their equations of motion. This is a very effective technique for examining the atomic scale and macro-scale properties of nanomaterials such as nanowires, carbon nanotubes, nanosheets, or biomolecules, as shown in Fig. 2.6. In MD simulation, atoms are thought of as a point mass that are joined together by springs. In this method, the springs represent the bond between the atoms. Force fields or potentials are used to obtain the time course of atomic positions and velocities. The MD method uses Newton's law of classical mechanics, which is Newton's second law, to derive equations of motion:

$$F_i = m_i a_i \tag{4.1}$$

equation 4.1 is defined for each atom i that consists of N atoms in an atomic system. In this equation, m_i is the atomic mass, $a_i = \frac{d^2 r_i}{dt^2}$ acceleration and F_i is the force exerted on atom i, obtained by interaction with other surrounding atoms. Thus, unlike the Monte Carlo method, which essentially depends on the random sampling of solutions to obtain numerical results, MD is a definitive method in which the variables of the atomic phase space at the current time stage are calculated using the previous time stage. Statistical physics maintains the relationship between the microscopic properties and the thermodynamic properties of a physical system.

4.2 History and Future of MD Simulations

Gibson et al. in 1960 were among the first to use MD simulation of a system consisting of 500 atoms. They performed this simulation using continuous force potentials and with finite-difference time integration to find the effect of defects in radiation damage [50]. In 1964, Rahman simulated another system consisting of 864 atoms of liquid Argon with Leonard Jones potential using MD simulation [51].

Since the performance of the properties of biomolecules is completely dependent on their dynamic behaviour, MD simulations are very useful. For this purpose, MD simulation is especially used in the pharmaceutical industry. Extracting the characteristics of a thermodynamic system that is physically possible is one of the most prominent advantages of MD simulations for researchers. As computing power increases day by day, the ability to solve complex problems numerically also increases. In addition, because simulation and computer calculations are always more economical than experimental tests, the MD method is very efficient in the development of obtaining new materials. This method is also very cost-effective and popular for analyzing failure mechanisms at the nanoscale. Ovesy et al. [52] have used MD simulation to describe the mechanical properties and failure behaviour of van der Waals transformation structures consisting of single-layer graphene and hexagonal boron nitride (hBN) sheets. The MD simulation method is a very important method for the design of new materials in all industries related to materials such as lubrication, catalyst, electronics, and chemical engineering or nanoelectromechanical device design. Although the current use of the MD method is limited to the academic field, with the exception of designing pharmaceuticals and polymers, in the coming decades, the MD simulation technique will replace today's computational tools in the industry, as shown in Fig. 4.1, examples of industrial devices are designed and simulated by MD platforms [53].

Fig. 4.1 Molecular device design examples (a) Gear chain and (b) Planetary Gear.

4.3 Limitations of MD

Although the MD method is a convenient and high-precision tool in the molecular world, there are limitations. The first limitation of the MD technique is using

Newton's classical laws instead of Schrodinger's equation, which can exert quantum effects. It should be noted that systems at the atomic level are governed by quantum laws instead of classical macro-scale laws. The classical approximation to the atomic world can be defined by the thermal wavelength of de Broglie thermal wavelength [50]. Due to the classical approach used in MD, the classical approximation is not sure for very light elements such as He and Ne. Another issue with MD simulation is the calculation of forces. Since the interaction between atoms leads to the forces acting on the corresponding atoms that direct the motion of the atoms in the system, it is essential to calculate the forces acting on the atoms to obtain the actual physical response. The forces are usually calculated with the gradient of a potential function that depends on the coordinates of the system atoms. Therefore, the degree to which MD simulations are close to reality depends strongly on the capacity of the potentials to obtain the material response under the boundary conditions used in the simulation. MD simulations combine with statistical mechanics to derive a classical system's macro-scale equilibrium and microstructural properties. Fig. 4.2 shows the significant calculations that are performed in MD calculations. Accordingly, three essential steps form the fundamental framework of MD. In the first step, initial positions and velocities are assigned to each atom in the system. Then, the particles in the simulation box interacted with each other via a potential function, and the forces on each atom were calculated based on the applied potential. For this reason, the potential used for the simulation is a critical aspect in determining how realistic the simulation is. Due to computational efficiency, potential calculations are not performed between all atoms. Instead, by defining the neighborhood radius for each atom, only a number of atoms within the neighborhood are used to determine the interatomic forces. In the second step, Newton's second law, $F = ma$, is used to obtain the velocities and positions of the atoms for the next time steps. The time evolution of atoms leads to the movement of atoms in the simulation box, which creates a path in space. In the third step, the position and moment of the atoms are used to determine the physical quantities of the system by using the concepts of statistical mechanics. According to statistical mechanics, the macroscale properties of a system are the norm of the corresponding quantity over all possible quantum states, which is called the ensemble average. An ensemble can be considered an imaginary set of distinct quantum states, all of which have the same macroscopic properties, such as temperature and pressure. In additional words, for a defined system, there exist different quantum states (i.e., the phase space of the atomic

system) that satisfy the same macroscopic properties. An ensemble is a set of all quantum states that have the same macroscopic property. The Ergodic hypothesis expresses that the ensemble averages of system characteristics are equal to the time averages. Therefore, by taking the time average of the measurements acquired by MD simulation, macroscopic physical quantities can be obtained. Another limitation of MD calculations is the high computational volume in larger dimensions. Because MD calculations are only comparable at the nanoscale, higher-scale computations require multi-scale methods, which will be discussed in more detail below.

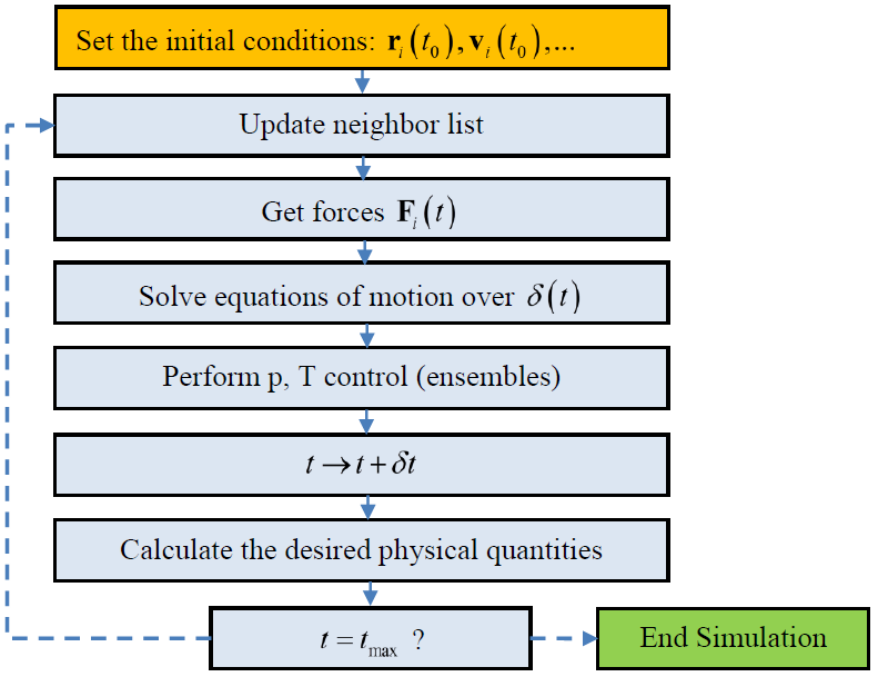

Fig. 4.2 MD simulations workflow.

4.3.1 Interatomic Potentials

The interatomic potentials that can be used to describe atomic interactions in MD simulation can be considered the heart of simulation [51]. The most general form of atomic potential is presented as follows:

$$U(r_1, r_2, \ldots, r_N) = \sum_i U_1(r_i) + \sum_{i,j>i} U_2(r_i, r_j) + \sum_{i,j>i,j>j} U_3(r_i, r_j, r_k) + \ldots \quad (4.2)$$

In Eq. 4.2, U_1 defines the one-body potential that represents external force fields such as the gravitational field. The second expression in the equation. 4.2, U_2 describes a two-body potential that formulates the dependence of the interatomic potential on the distances (r_{ij}) between pairs of atoms (r_i and r_j) in the atomic system, as shown in Fig. 4.3 (a). The third expression in the equation Eq. 4.2, the three-body potential (U_3), as shown in Fig. 4.3 (b), and higher-order potentials add total energy to the system potential energy related to the geometry of the atomic arrangement in the system. Inter-atomic potential functions can be obtained experimentally or based on numerical quantum mechanical approximations. Semi-experimental interatomic potential functions are also obtained by parameterizing experimental data and ab initio data. Force field time calculations are the most important part of MD simulation. generally, two different approaches can be classified to select the interaction between atoms and molecules. In the first approach, a function depends on interatomic positions (i.e, distances and relative angles) and parameters that are fitted to the potential function to plot the real properties of the system [54]. In this approach, the dynamics and behavior of electrons are not directly included in the potential functions. However, in the second approach, which is theoretically richer but computationally more expensive, the electronic structure is considered and the forces acting on the atoms are calculated based on quantum mechanical behavior. The second approach is based on the simulation of MD from the beginning. Classical MD is based on the first approach. Therefore, the forces acting on the atoms are obtained from the gradient of the potential function to the displacements:

$$F_i = \frac{\partial}{\partial r_i} U(r_i) = -\left(\frac{\partial U}{\partial x_i}, \frac{\partial U}{\partial y_i}, \frac{\partial U}{\partial z_i}\right) \tag{4.3}$$

As mentioned earlier, in MD simulation, it is important to use the appropriate interatomic potential that defines the proper interaction forces between the system atoms.

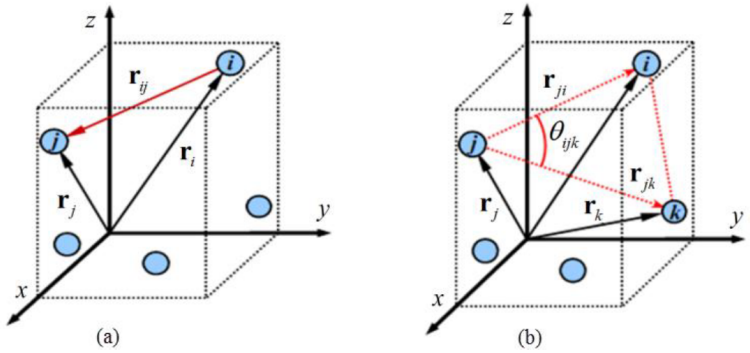

Fig. 4.3 (a) Two and, (b) three-body potential parameters

4.3.2 Leonard-Jones potential

One of the most well-known potentials used for the van der Waals system is the Leonard-Jones potential, the formula of which is given below (see Fig. 4.4).

$$u_{LJ}(r_{ij}) = 4\varepsilon \left[\left(\frac{\partial}{r_{ij}} \right)^{12} - \left(\frac{\partial}{r_{ij}} \right)^{6} \right] \tag{4.4}$$

The Leonard Jones potential is a function of two parameters, the ε interaction energy and the equilibrium distance, which is ∂ [55]. These parameters are selected according to the specific physical properties of the system.

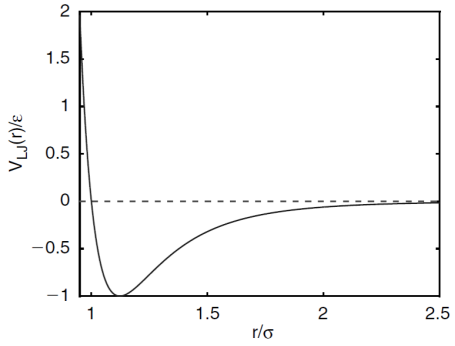

Fig. 4.4 Lennard-Jones potential [3].

4.3.3 Adaptive Intermolecular Reactive Emprical Bond-order Potential

Adaptive Intermolecular Reactive Emprical Bond-Order (AIREBO) Potential is an experimental potential used to model carbon-hydrogen interactions that developed by Stuart et al. [56]. This potential is an extended version of potential he Brenner's Reactive Emprical Bond-Order (REBO) [57] that incorporates non-bonded atomic interactions. The basic formula for AIREBO potential is as follows.

$$E = E^{REBO} + E^{LJ} + E^{tore} \tag{4.5}$$

As can be seen from equation 4.5, AIREBO is a combination of the REBO bond E^{REBO}, the Lenard-Jones potential E^{LJ} and the torsional potential E^{tore}, respectively. E^{REBO} part of the AIREBO bond represents covalent bond interactions,and is short-range potential.

$$E^{REBO} = V_{ij}^{R}(r_{ij}) + b_{ij}V_{ij}^{A}(r_{ij}) \tag{4.6}$$

In Eq. 4.6, V_{ij}^{R} and V_{ij}^{A} show the repulsive and attractive pair potentials, and b_{ij} is the expression of the bond order. Factors such as the presence of neighboring atoms and the type of hybridization that affect the covalent bond interaction conditions are described in this term. The Leonard-Jones representation E^{LJ} used in the AIREBO potential includes the potential Lenard-Jones term V_{ij}^{LJ} and the sine (S) and cosine (C) switch functions.

$$E_{ij}^{LJ} = S(t_r(r_{ij}))S(t_b(b_{ij}^{*}))C_{ij}V_{ij}^{LJ}(r_{ij}) + [1 - S(t_r(r_{ij}))]C_{ij}V_{ij}^{LJ}(r_{ij}) \tag{4.7}$$

where

$$V_{ij}^{LJ}(r_{ij}) = 4\varepsilon_{ij}\left[\left(\frac{\partial_{ij}}{r_{ij}}\right)^{12} - \left(\frac{\partial_{ij}}{r_{ij}}\right)^{6}\right] \tag{4.8}$$

The torsional potential expression of E^{tore} is given by Eq. 4.8 is generated by four neighboring atoms and depends on a dihedral angle that includes cosine switches varying from 0 to 1.

$$E^{tore} = \frac{1}{2}\sum_{i}\sum_{i\neq j}\sum_{k\neq i,j}\sum_{l\neq i,j,k} w_{ij}(r_{ij})w_{jk}(r_{jk})w_{kl}(r_{kl}) \times V^{tors}(\omega_{ijkl}) \tag{4.9}$$

$$V^{tors}(\omega) = \varepsilon\left[\frac{256}{405}\cos^{10}\left(\frac{\omega}{2}\right) - \frac{1}{10}\right] \tag{4.10}$$

4.3.4 Embedded Atom Method

Embedded atom method (EAM) expresses interatomic interactions that is a quasi-empirical model and interacts with each atom in the simulation box as embedded in a host lattice environment consisting of all other atoms [58]. In this method, the total energy of a metal system composed of N atoms is obtained by the following relation:

$$E_{tot} = \sum_{i}^{N} E_i \tag{4.11}$$

Where E_i is the energy term for atom i th in the system, it is calculated as follows.

$$E_i = \frac{1}{2}\sum_{j}\phi(r_{ij}) + F(\bar{\rho}_i) \tag{4.12}$$

Where the first term $\phi(r_{ij})$ is a function of atomic displacements and represents the atomic pairwise interaction. The second term $F(\bar{\rho}_i)$ expresses the effect of electron density, also called the embedding energy function.

$$\bar{\rho}_i = \sum_{j}\rho(r_{ij}) \tag{4.13}$$

The embedding energy function is calculated as the sum of the pairwise interaction terms $\rho(r_{ij})$ and depends on the local electron density $\bar{\rho}$. Because the actual values of the terms $\phi(r_{ij})$, $\rho(r_{ij})$ and F are not exactly known, their parametric shapes are used [55]. This study uses the EAM and AIREBO potentials to simulate GF and Au polycrystalline.

4.4 LAMMPS

The LAMMPS (Large-scale Atomic/Molecular Massivle Parallel Simulator) is a classic open-source MD code developed by a joint research study consisting of US Department of Energy (DOE) laboratories and three companies [59]. Using LAMMPS, many nanoscale systems, including atomic, polymeric, biological, metallic, granular, and coarse-grained systems, can be modeled with force field potentials. LAMMPS can be used to model systems with a small number of particles, up to millions or even billions of particles. Previous versions of LAMMPS were written in F77 and F90, and the latest versions of LAMMPS were written in C^{++}. Because it was programmed to be updated by others, researchers could modify the code to extend new force fields, atomic types, or boundary conditions, and other capabilities. LAMMPS can simulate any system made up of individual particles, and potentials describe the interaction between particles. LAMMPS solves Newtonian equations of motion for a set of atoms, molecules, or macroscopic particles that interact with each other by short or long-range forces and uses neighboring lists to perform force field calculations.

Chapter 5

CUF Micromechanical Model

5.1 Introduction

This chapter presents a multi-scale method for investigating the elastic, thermoelastic, and thermal properties of polymer nanocomposites reinforced with GF. The effects of mass density and porosity on the properties of GF/polymer composites have been analyzed using multi-scale modeling and the concept of RUC. An RUC of SEM images from laboratory samples is considered. This model has brought very accurate and reliable results for similar research. This chapter also defines the Carrera unified formulation (CUF) finite element methods and micromechanical modeling based on the mechanics of structural genome MSG.

5.2 Thermoelastic of CUF-MSG Micromechanical Method

A high-efficient micro-elastic model based on the analysis of heterogeneous composite materials has been used to calculate the thermoelastic properties of graphene foam/polymer composite. In this model that is based on CUF [4] and mechanics of structure genome (MSG) [60], the properties of the composite, including Young modulus, Poisson ratio, coefficient of thermal expansion are calculated using the properties of the composite components by a unit cell. The meaning RUC is the smallest volume that includes all the information required to identify the properties of materials. Hence, the micromechanical model can be obtained from an imagi-

nary composite material that occupies three-dimensional space and is composed of an infinite number of unit cells. MSG is based on variational asymptotic method (VAM)[61, 62]; VAM provides efficient solutions to structural problems by performing an asymptotic expansion on one or more small parameters that can find the stationary points of a function and obtaining the effective elastic properties and the local solutions of periodically heterogeneous materials with great accuracy and efficiency [62]. CUF has been developed for beams, plates, and shells. Although 1D models are used in the present research, they have been demonstrated to provide the same accuracy as conventional solid elements with reduced computational efforts. It can be seen in references [63, 64]. Accordingly, the main direction of the micro-scale constituents (e.g., the fiber direction in the case of fiber-reinforced polymers or inclusions) is discretized using one-dimensional finite elements. In contrast, the cross-section is hierarchically enriched with a set of polynomials with non-local capabilities. In addition, the implementation of a non-isoparametric mapping technique permits the representation of the exact geometry of the constituents with no additional costs [65].

According to CUF, the 3D displacement field can be expressed as follows:

$$\mathbf{u} = N_i(y)F_\tau(x,z)\mathbf{u}_{\tau i} \tag{5.1}$$

Where N_i and F_τ are the shape function and cross-section expansion function, respectively, which characterize the model kinematics, and $\mathbf{u}_{\tau i}$ is the vector of generalized unknowns. Fig.5.1 shows the shape functions N_i and N_j extend the solution from the nodes to the axis. Expansion functions F_τ and F_s develop the answer from the nodes to the cross-section of the bar.

This work employs an efficient thermoelastic micromechanical model for the prediction of purely elastic properties (Young modulus and Poisson ratio), as well as thermal properties, such as the coefficient of thermal expansion (CTE) and specific heat at constant volume. According to micromechanical analysis, the RUC is much smaller than the global structure in terms of size. Here, $\mathbf{y} = \mathbf{x}/\delta$, which δ is an undersized scale factor that indicates RUC's size. $\mathbf{x}$ and $\mathbf{y}$ are the global and local reference systems, respectively.

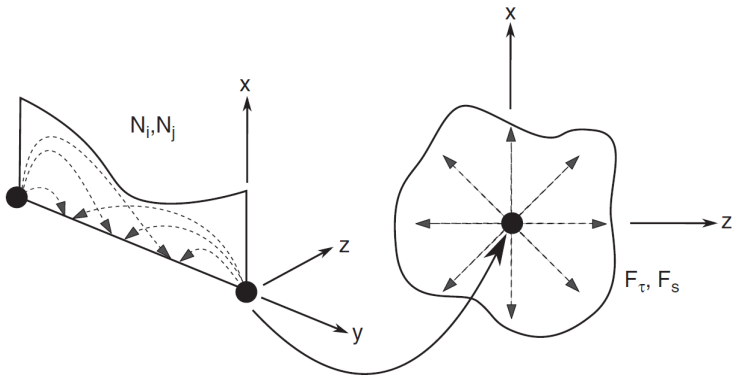

Fig. 5.1 Schematic of axial approximation by (N_i and N_j) and cross-sectional expansion by F_τ and F_s [4].

The proposed model assumes that the arrangement of the constituents follows a periodic pattern (RUC), which represents the minimum geometrical building block that can be repeated over the space to shape the material's higher scales, Fig. 5.2. Additionally, the following two assumptions are made:

- An average amount aboard the RUC volume in the local solutions is related to the macroscopic problems in the global solution. Applying this issue to $\mathbf{u}(\mathbf{x};\mathbf{y})$, Eq. (5.2) will be appear:

$$\bar{\mathbf{u}}(\mathbf{x}) = \frac{1}{V}\int_V \mathbf{u}(\mathbf{x};\mathbf{y})dV \tag{5.2}$$

  where $\bar{\mathbf{u}}(\mathbf{x})$ conveys the vector of average displacement in global coordinates and V represents the cell's volume.

- The effective material properties obtained from the RUC analyses depend neither on the loading and boundary conditions nor the geometry of the microscale problem.

Once considered these hypotheses, the MSG is depicted. MSG, first introduced by Yu [60], exploits the VAM [62] for solving problems that involve smaller parameters. MSG proposes a solution to the stationary value problem by minimizing the difference between the homogenized material's strain energy and that of the

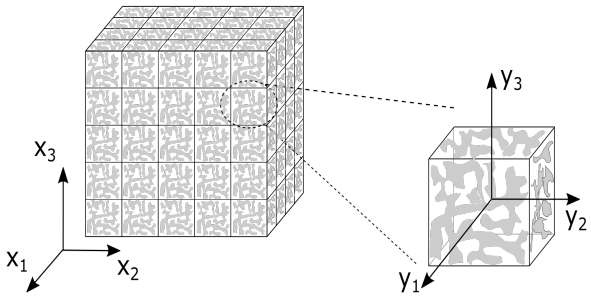

Fig. 5.2 Coordinate reference systems of a periodic heterogeneous material and its RUC.

heterogeneous material. It is expressed in the following functional:

$$\Pi = \frac{1}{2}\left\langle C_{ijkl}\varepsilon_{ij}\varepsilon_{kl} + 2\beta_{ij}\varepsilon_{ij}\theta + c_v\frac{\theta^2}{T_0}\right\rangle - \frac{1}{2}\left(C^*_{ijkl}\bar{\varepsilon}_{ij}\bar{\varepsilon}_{kl} + 2\beta^*_{ij}\bar{\varepsilon}_{ij}\theta + c^*_v\frac{\theta^2}{T_0}\right) \quad (5.3)$$

where $\langle\rangle$ designates the average of the volume. The first term of the functional is the strain energy of the heterogeneous material characterized by the RUC, whereas the second corresponds to the equivalent homogenized material. C_{ijkl}, ε_{ij}, and β_{ij} are the elastic tensor, the strain, and thermal stress tensors, respectively. T_0 is the temperature of reference at which the constituent material is stress-free. c_v is the specific heat per constant volume unit, and θ symbolizes the difference between T_0 and the current temperature. It must be mentioned in this part the temperature field is considered constant over the RUC volume. It means there is no thermal conductivity (TC) here.

It is beneficial to formulate the variational over a unit RUC to evade solving the static problem for each point in the global system $\mathbf{x}$. Thus, the precise solution $\mathbf{u}$ can be defined by the totality of the global displacements $\bar{\mathbf{u}}$ and the fluctuation difference as follows:

$$\mathbf{u}(\mathbf{x};\mathbf{y}) = \bar{\mathbf{u}}(x) + \delta\chi(\mathbf{x};\mathbf{y}) \quad (5.4)$$

In which χ illustrates the fluctuation functions around the global displacement. Coordinate systems' difference recreates an essential role in the multiscale problem that calculates the field's derivatives of $\mathbf{u}(\mathbf{x};\mathbf{y})$ as:

$$\frac{\partial \mathbf{u}}{\partial x_j} + \frac{1}{\delta}\frac{\partial \mathbf{u}}{\partial y_j} \tag{5.5}$$

Hence, substituting Eq. (5.5) to Eq. (5.4) the strain is expressed as:

$$\varepsilon_{ij}(\mathbf{x};\mathbf{y}) = \overline{\varepsilon_{ij}}(\mathbf{x}) + \chi_{(i,j)}(\mathbf{x};\mathbf{y}) \tag{5.6}$$

where

$$\overline{\varepsilon_{ij}}(\mathbf{x}) = \frac{1}{2}\left(\frac{\partial \overline{\mathbf{u}}_i(\mathbf{x})}{\partial x_j} + \frac{\partial \overline{\mathbf{u}}_j(\mathbf{x})}{\partial x_i}\right) \tag{5.7}$$

and

$$\chi_{(i,j)}(\mathbf{x};\mathbf{y}) = \frac{1}{2}\left(\frac{\partial \overline{\chi}_i(\mathbf{x};\mathbf{y})}{\partial y_j} + \frac{\partial \overline{\chi}_j(\mathbf{x};\mathbf{y})}{\partial y_i}\right) \tag{5.8}$$

Regarding Eq. (5.2), it would be penned $\overline{u}_i = \langle u_i \rangle$ and $\overline{\varepsilon_{ij}} = \langle \varepsilon_{ij} \rangle$ which automatically signifies that $\langle \chi_i \rangle = 0$ and $\langle \chi_{(i,j)} \rangle = 0$. Then, utilizing displacements' field and strain from Eqs. Eq. (5.4) and Eq. (5.6), respectively, and considering the second term of Eq. (5.3) as a constant, the unknown of fluctuation terms will be decrypted by minimizing the below functional:

$$\Pi^* = \frac{1}{2}\langle C_{ijkl}\left[\bar{\varepsilon}_{ij} + \chi_{(i,j)}\right]\left[\bar{\varepsilon}_{kl} + \chi_{(k,l)}\right] + 2\beta_{ij}\left[\bar{\varepsilon}_{ij} + \chi_{(i,j)}\right]\theta + c_v\frac{\theta^2}{T_0}\rangle \tag{5.9}$$

in which $\chi_{(i,j)}$ is the derivatives of the i^{th} fluctuation component with respect to the j^{th} coordinate of the RUC's local reference system $\mathbf{y}$. The innovation of this method is to present an efficient manner to solve the thermo-elastic RUC problem using refined and geometrically accurate beam models.

5.2.1 Refined Beam Models for the Unit Cell Problem

In microstructure, MSG can be used to model a 3D problem with various elements going along the three directions, like particle inclusion composites, or a 2D problem in that the phases change within the plane, similar to composites with fiber-reinforced. Fig. 5.3 presents RUC in a local coordinate system utilizing a special microstructure model that can be scrutinized employing this method. The beam axis, of length L, is set to be the direction of the fiber y_1, while the y_2,y_3-plane determines the

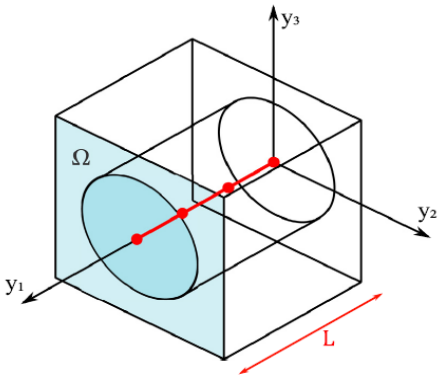

Fig. 5.3 Local coordinate system for RUC problem

cross-section Ω. Here, it is explained that the use of CUF-based 1D models for solving the RUC problem can be developed by considering the fluctuation unknowns χ through the cross-section. Classically, CUF has been used to solve structural problems by expressing the field of displacement in terms of F_τ and $\mathbf{u}_\tau$. Nevertheless, the field of displacements can be substituted by the fluctuation unknowns with no further implications as follows:

$$\chi(\mathbf{x};y_1,y_2,y_3) = F_\tau(y_2,y_3)\chi_\tau(\mathbf{x};y_1) \quad \tau = 1,...,M \tag{5.10}$$

in which τ signifies summation, and M is the order of expansion terms. The structural model's order and, thus, the precision of the solution can be adjusted by a suitable expansion function, as demonstrated in references [30,31]. In this work, hierarchical Legendre expansions (HLE) [66] are used as expansion functions and are coupled with the blending function method in order to achieve a geometrically exact representation of the RUC, as presented in [63, 67].

5.2.2 Hierarchical Legendre Expansions (HLE)

In this thesis, HLE beam models, as specified by Carrera et al. [66], are utilized. To create arbitrary functions throughout the cross-section F_τ, they exploited the hierarchical properties of Legendre-based polynomials. It is clear that the displacement field, and therefore the precision of results, is dependent on the higher-order polynomials. Expansion functions can be classified as vertex, side, or internal. The first-order expansion functions named vertex functions are expressed as:

$$F_\tau = \frac{1}{4}(1-r_\tau r)(1-s_\tau s) \quad \tau = 1,2,3,4 \tag{5.11}$$

in which r and s have values between -1 and 1; Also, r_τ and s_τ describe coordinates of vertex in natural plane.

Higher-order models are obtained by adding more side functions to displacement fields:

$$\begin{aligned} F_\tau(r,s) &= \tfrac{1}{2}(1-s)\phi_{Pb}(r) \quad \tau = 5,9,13,18,... \\ F_\tau(r,s) &= \tfrac{1}{2}(1+r)\phi_{Pb}(s) \quad \tau = 6,10,14,19,... \\ F_\tau(r,s) &= \tfrac{1}{2}(1+s)\phi_{Pb}(r) \quad \tau = 7,11,15,20,... \\ F_\tau(r,s) &= \tfrac{1}{2}(1-r)\phi_{Pb}(s) \quad \tau = 8,14,16,21,... \end{aligned} \tag{5.12}$$

where ϕ_{Pb} is corresponded to 1D internal Legendre type and p refers to the beam theory's polynomial order. For additional information about ϕ_{Pb}, the reader can study [66, 68] in which Legendre polynomials are mathematically described and applied to various FEM problems. Following relations are the definitions of internal functions:

$$\begin{aligned} F_{28}(r,s) &= \phi_4(r)\phi_2(s) \\ F_{29}(r,s) &= \phi_3(r)\phi_3(s) \\ F_{30}(r,s) &= \phi_2(r)\phi_4(s) \end{aligned} \tag{5.13}$$

5.2.3 Unified High-order Finite Beam Elements

The problem is solved with the beam model along the y_1 axis employing FEM. By this approach, the direction of the fiber is divided to 1D elements. So, the fluctuations unknowns $\chi_\tau(\mathbf{x};y_1)$ are interpolated applying with Lagrange polynomials as shape functions $N_i(y_1)$:

$$\chi_\tau(\mathbf{x};y_1) = N_i(y_1)\chi_{\tau i}(\mathbf{x}) \quad i = 1,...,n \tag{5.14}$$

in which n is the beam's total nodes and $\chi_{\tau i}(\mathbf{x})$ is the vector of unknowns.
By representing the global strains as:

$$\overline{\varepsilon}^T = \{\overline{\varepsilon}_{11}\ \overline{\varepsilon}_{22}\ \overline{\varepsilon}_{33}\ 2\overline{\varepsilon}_{23}\ 2\overline{\varepsilon}_{13}\ 2\overline{\varepsilon}_{12}\} \tag{5.15}$$

the geometrical relations can be written as:

$$\varepsilon = \bar{\varepsilon} + \mathbf{D}\chi \tag{5.16}$$

in which **D** is a differential operator described as below:

$$\mathbf{D} = \begin{bmatrix} \partial_{y_1} & 0 & 0 \\ 0 & \partial_{y_2} & 0 \\ 0 & 0 & \partial_{y_3} \\ 0 & \partial_{y_3} & \partial_{y_2} \\ \partial_{y_3} & 0 & \partial_{y_1} \\ \partial_{y_2} & \partial_{y_1} & 0 \end{bmatrix} \tag{5.17}$$

Then, the thermo-elastic relation between stresses and strains is indicated as:

$$\sigma = c\varepsilon - \beta\theta \tag{5.18}$$

in which **C** is the stress-strain connector matrix and $\beta = \mathbf{C}\alpha$, that α is vector of thermal expansion coefficients.

Then, substituting Eq. (5.16) in the Eq. (5.3), the following functional is be obtained :

$$\Pi^* = \frac{1}{2}\int_V \left[(\bar{\varepsilon} + \mathbf{D}\chi)^T \mathbf{C} (\bar{\varepsilon} + \mathbf{D}\chi) + 2\beta(\bar{\varepsilon} + \mathbf{D}\chi)\theta + c_v \frac{\theta^2}{T_0} \right] dV \tag{5.19}$$

It must be noted the periodic boundary conditions must apply to the RUC cross-section's sides ($\chi_\tau{}^+ = \chi_\tau{}^-$), and as vertically wise to the fiber ($\chi_{\tau l} = \chi_{\tau n}$). Also, defining Eq. (5.14) into Eq. (5.10), and the resulting in Eq. (5.19), the functional Π^* is depicted in the format of CUF as follow:

$$\Pi^* = \frac{1}{2}\left(\chi_{sj}^T E^{\tau sij} \chi_{\tau i} + 2\chi_{sj}^T D_{h\varepsilon}^{sj} \bar{\varepsilon} + \bar{\varepsilon}^T D_{\varepsilon\varepsilon} \bar{\varepsilon} + 2\chi_{sj}^T D_{h\theta}^{sj} \theta + 2\bar{\varepsilon}^T D_{\varepsilon\theta} \theta + D_{\theta\theta} \frac{\theta^2}{T_0} \right) \tag{5.20}$$

where

$$
\begin{aligned}
&\mathbf{E}^{\tau sij} = \int_\Omega \int_l (D(F_\tau N_i I))^T C D(F_s N_j I) d\Omega dy_1 \\
&\mathbf{D}_{h\varepsilon}^{sj} = \int_\Omega \int_l (D(F_s N_j I))^T C d\Omega dy_1 \\
&\mathbf{D}_{\varepsilon\varepsilon} = \int_V C dV \\
&\mathbf{D}_{h\theta}^{sj} = \int_\Omega \int_l (D(F_\tau N_i I))^T \beta d\Omega dy_1 \\
&\mathbf{D}_{\varepsilon\theta} = \int_V \beta dV \\
&\mathbf{D}_{\theta\theta} = \int_V c_v dV
\end{aligned}
\tag{5.21}
$$

$\mathbf{E}^{\tau sij}$, $\mathbf{D}_{h\varepsilon}^{sj}$, $\mathbf{D}_{h\theta}^{sj}$ are the thermo-elastic fundamental nuclei of RUC, containing all the structural model information. Furthermore, $\mathbf{D}_{\varepsilon\varepsilon}$, $\mathbf{D}_{\varepsilon\theta}$ and $\mathbf{D}_{\theta\theta}$ are the volume average effective of stiffness matrix, the volume average of thermal stiffness matrix and volume average of material's specific heat, respectively. Hence, by looping via indexes τsij, it can derive the assembled $\mathbf{E}$, $\mathbf{D}_{h\varepsilon}$, $\mathbf{D}_{h\theta}$ matrices. τ and s include the loop on the cross-section and expansion functions according to selected F_τ and the order of expansions. Also, the looping on the i and j indexes rely on the desired shape functions.

The fluctuation unknowns which put in the functional Eq. (5.20) can be calculated by considering the following system:

$$
\mathbf{E}\chi = -\mathbf{D}_{h\varepsilon}\bar{\varepsilon} - \mathbf{D}_{h\theta}\theta \tag{5.22}
$$

Besides, by assuming:

$$
\chi = \chi_0 \bar{\varepsilon} + \chi_\theta \theta \tag{5.23}
$$

where χ_θ and χ_0 are 3×6 and 3×1 matrices respectively, and substituting it in Eq. (5.22), one can introduce below linear system:

$$
\begin{cases}
\mathbf{E}\chi_0 = -\mathbf{D}_{h\varepsilon} \\
\mathbf{E}\chi_\theta = -\mathbf{D}_{h\theta}
\end{cases}
\tag{5.24}
$$

Finally, by substituting Eq. (5.23) in the Eq. (5.20), following equation can be extracted:

$$
\Pi^* = \frac{1}{2}\bar{\varepsilon}^T C^* \varepsilon + \bar{\varepsilon}^T \bar{\beta}\theta + \frac{1}{2}\bar{c_v}\frac{\theta^2}{T_0} \tag{5.25}
$$

with

$$C^* = \frac{1}{\Omega}(\chi_0^T D_{h\varepsilon} + D_{\varepsilon\varepsilon}) \quad \bar{\beta} = \frac{1}{\Omega}\left[\frac{1}{2}(D_{h\varepsilon}^T \chi_\theta + \chi_0^T D_{h\theta}) + D_{\varepsilon\theta}\right] \quad \bar{c_v} = \frac{1}{\Omega}[\chi_\theta^T D_{h\theta} T_0 + D_{\theta\theta}] \tag{5.26}$$

in which $\mathbf{C}^*$ includes the equivalent properties of the material for the homogenized model. It is clear that the effective thermal expansion coefficients can be computed as $\bar{\alpha} = -C^{*-1}\bar{\beta}$.

5.3 Thermal Conductivity CUF-MSG Method

5.3.1 Mechanics of Structure Genome and Carrera Unified Formulation for Micromechanical Thermal Conductivity Problems

Micromechanical analyses allow us to understand how details at the microscopic level of a composite material influence the features of the homogeneous material as a whole. The present micromechanical study is based on the MSG first introduced by W. Yu in [69]. The MSG is based on the Structure Genome (SG) concept, which represents the fundamental block of the problem. The model used for the analysis is called RUC. The RUC represents the smallest entity which contains all the structure's features, such as the volume friction, geometry, and fiber arrangement. The RUC could then be repeated over the global volume to build the entire structure at the meso- or macro-scale. The MSG method is based on the VAM to solve the problem by minimizing the energy between the homogeneous and the heterogeneous material.

The similarities of the repeating components in the SEM images of synthesized GF [5] allow the selection of a micro-scale RUC with the characteristics of the whole GF. Fig. 5.4 displays a zoommed area of the GF and the respective RUC model for the micromechanical analysis. The blue lines in Fig. 5.4(a) demonstrate the boundaries of the proposed UC. Due to SEM images being 2D, the extracted borders are only on one surface of the cubic UC. Hence, the prepared surface is extruded in the third direction to create a cubic shape. Finally, Fig. 5.4(b) shows that the

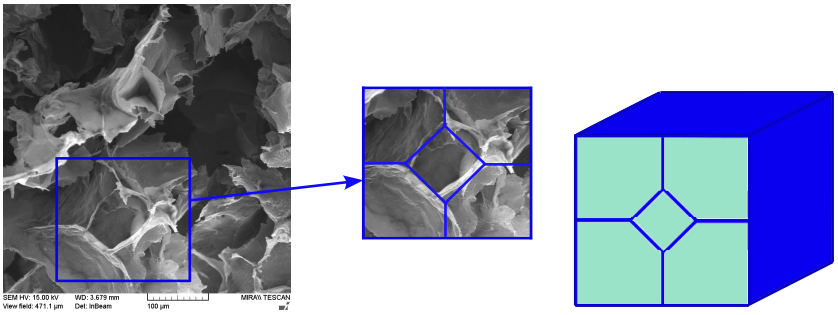

(a) (b)

Fig. 5.4 (a) SEM image of GF [5], (b) Schematic model of the UC consists of GF (blue parts) and matrix (green parts).

proposed RUC consists of two components. The RUC of GF/PDMS composites is considered with a volume fraction of 14% of GF.

In this paper, MSG is coupled with the Carrera Unified Formulation (CUF) to allow an accurate description of the model, providing a high level of precision within a 1D model while still maintaining the same level of accuracy as a 3D model. The formulation changes according to the property to be investigated. For instance, the paper [70] shows a micromechanical analysis to study the elastic properties of different composites, whereas in [71] is reported the thermo-elastic case. The present micromechanical analysis of the TC features utilizes the MSG formulation as done by Tang and Yu in [72] and the CUF-FEM approach to reduce a complex 3D problem in less demanding 2D or 1D models while maintaining the same level of accuracy. The CUF-MSG analysis serves as a tool to retrieve the homogenized TC properties of a particular RUC to compare the experimental data found in the literature.

5.3.2 Formulation of the MSG-CUF Analysis for Thermal Conductivity

A fundamental assumption for micromechanical analysis of the RUC models is the consideration that the boundary conditions, the geometry, and the different loading conditions at the macroscopic scale do not affect the effective material properties of the micro-model. In addition, it has to be considered that the local solutions have an average value over the RUC volume equal to the global solution of the macroscopic

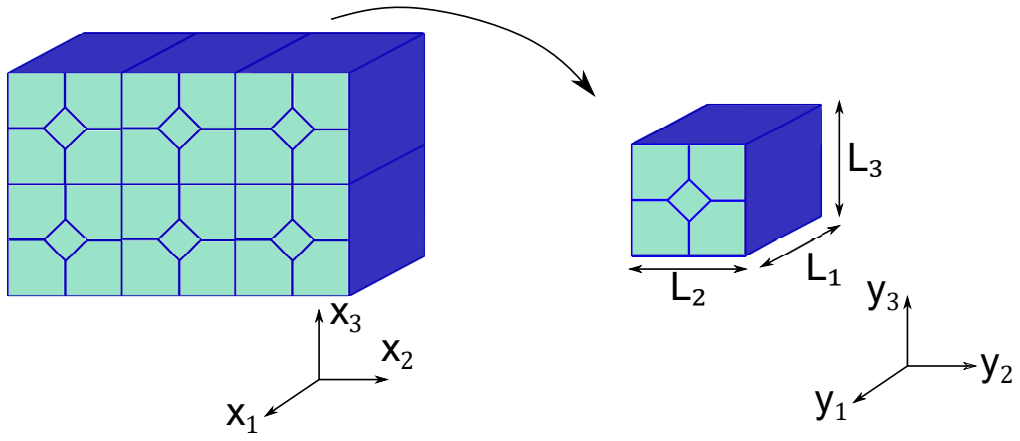

Fig. 5.5 Repeatable unit cells of the complex microstructure forming heterogeneous material.

problem. By applying these hypotheses to the TC problem, it is possible to write:

$$\frac{1}{V}\int_V \phi(\mathbf{x};\mathbf{y})dV = \bar{\phi}(\mathbf{x}) \tag{5.27}$$

where $\bar{\phi}$ represents the global temperature field in the global coordinate system, and V is the total volume of the microstructure. Fig. 5.5 shows the RUC model for the problem considered with the two reference systems **x** and **y**, which represent the global and the local coordinate system, respectively. The PBCs are applied over the RUC model to ensure the continuity of the temperature field between the straight faces:

$$\begin{aligned}
\phi\left(x_1,x_2,x_3;0,y_2,y_3\right) &= \phi\left(x_1+L_1,x_2,x_3;d_1,y_2,y_3\right)\\
\phi\left(x_1,x_2,x_3;y_1,-\frac{L_2}{2},y_3\right) &= \phi\left(x_1,x_2+d_2,x_3;y_1,\frac{L_2}{2},y_3\right)\\
\phi\left(x_1,x_2,x_3;y_1,y_2,-\frac{L_3}{2}\right) &= \phi\left(x_1,x_2,x_3+L_3;y_1,y_2,\frac{L_3}{2}\right)
\end{aligned} \tag{5.28}$$

Note that the origin of the coordinate system **y** is placed at the center of the RUC's face so that the length along the y_1 direction has coordinates (0, L_1).

In the present micromechanical analysis, the local temperature field, ϕ, can be expressed as the sum of the global TC field and a term representing the difference between both as:

$$\phi(x;y) = \bar{\phi}(x) + \delta\chi(x;y) \tag{5.29}$$

where χ represents the fluctuation function scaled with δ, the scale term that characterized the small dimensions of the microstructure considered. The fluctuation function is involved in all the MSG-based micromechanical analyses, allowing the link between the different scales that characterized the problem.

By deriving the temperature field, which depends on the two coordinates $(x;y)$, the relation assumes the following form:

$$\phi_{,i}(\mathbf{x};\mathbf{y}) = \bar{\phi}_{,i}(\mathbf{x}) + \delta\chi_{,i}(\mathbf{x};\mathbf{y}) \tag{5.30}$$

where

$$\bar{\phi}_{,i}(\mathbf{x}) = \frac{\partial\bar{\phi}(\mathbf{x})}{\partial x_i} \qquad \chi_{,i}(\mathbf{x};\mathbf{y}) = \frac{\partial\chi(\mathbf{x};\mathbf{y})}{\partial x_i} + \frac{1}{\delta}\frac{\partial\chi(\mathbf{x};\mathbf{y})}{\partial y_i} \tag{5.31}$$

Thus, substituting the two terms obtained in Eq. (5.31) into Eq. (5.30), the gradient of the TC field will become:

$$\phi_{,i}(\mathbf{x},\mathbf{y}) = \frac{\partial\bar{\phi}(\mathbf{x})}{\partial x_i} + \frac{\partial\chi(\mathbf{x};\mathbf{y})}{\partial y_i} \tag{5.32}$$

where the term $\delta\partial\chi/\partial x_i$ has been neglected, according to VAM [73]. The solution to the MSG problem is obtained by minimizing the difference between the energy of the heterogeneous microstructure and that of the equivalent homogenized material as follows:

$$\Pi = \left\langle \frac{1}{2}K_{ij}\phi_{,i}\phi_{,j} \right\rangle - \frac{1}{2}K^{*}_{ij}\bar{\phi}_{,i}\bar{\phi}_{,j} \tag{5.33}$$

where $\langle\rangle$ represents the volume average. K_{ij} is the second order tensor of the TC referred to the heterogeneous material, and ϕ, are the temperature gradients. The second term of the (5.33) regards the energy of the homogenized material that can be considered invariant. Therefore, the functional to be minimized for the TC problem is represented in the following expression.

$$\Pi_1 = \left\langle \frac{1}{2}K_{ij}\phi_{,i}\phi_{,j} \right\rangle \tag{5.34}$$

The MSG approach combined with the CUF methodology allows for an efficient procedure to compute the TC properties of a microscopic model, thanks to the high-order functions involved in the resolution technique.

Resolution of the CUF-MSG Thermal Conductivity Problem

The micromechanical problem is solved in terms of finite elements. Beam elements describe the RUC main direction. In particular, if homogeneous properties are considered along the main direction, a two-nodes one-dimensional element is enough to capture the microstructure behavior. Otherwise, at least three four-node one-dimensional elements must be employed to capture the change of the constituents along the y_1-direction. The y_1-direction is then interpolated with Lagrange expansion functions:

$$\chi_\tau(x;y_1) = N_i(y_1)\chi_{\tau i}(x) \qquad \tau = 1,2,...,n \tag{5.35}$$

where $\chi_{\tau i}$ is the vector of the nodal unknowns and, n is the nodes number of the beam model selected. Now, it is possible to introduce the global temperature gradient vector as:

$$\bar{\Phi}_{,}^{T} = \left\{ \bar{\phi}_{,1} \quad \bar{\phi}_{,2} \quad \bar{\phi}_{,3} \right\} \tag{5.36}$$

and the local TC gradient can be expressed as:

$$\Phi_{,} = \bar{\Phi}_{,} + D\chi \tag{5.37}$$

where D is the 3×1 differential operator:

$$D = \begin{Bmatrix} \partial y_1 \\ \partial y_2 \\ \partial y_3 \end{Bmatrix} \qquad \partial y_i = \partial(\cdot)/\partial y_i \quad i = 1,2,3. \tag{5.38}$$

By substituting the (5.37) into the (5.34), the energy of the heterogeneous material can be expressed as follows:

$$\Pi_1^* = \frac{1}{2}\int_V (\bar{\Phi}_{,} + D\chi)^T K(\bar{\Phi}_{,} + D\chi) dV \tag{5.39}$$

The matrix of the TC K is:

$$K = \begin{bmatrix} K_{11} & K_{12} & K_{13} \\ K_{12} & K_{22} & K_{23} \\ K_{13} & K_{23} & K_{33} \end{bmatrix} \tag{5.40}$$

According to the CUF, the RUC problem can be addressed by expanding the fluctuation unknowns (χ) over the RUC cross-section in terms of arbitrary expansions functions (F_τ) according to the cross-section's coordinates y_2-y_3:

$$\chi(\mathbf{x};y_1,y_2,y_3) = F_\tau(y_2,y_3)\chi_\tau(\mathbf{x};y_1) \quad \tau = 1,...,M \tag{5.41}$$

where τ indicates summation and M is the number of expansion terms adopted in the kinematic model. In order to solve the RUC problem, the fluctuation unknowns χ in the (5.39) have to be expressed in CUF-FEM terms. Thus, by substituting (5.35) into (5.41) and then all into (5.39), the following expression is achieved:

$$\Pi_1^* = \frac{1}{2}(\chi_{sj}^T F^{\tau sij}\chi_{\tau i} + 2\chi_{sj}^T K_{h\Phi}^{sj}\bar{\Phi},+\bar{\Phi},^T K_{\Phi\Phi}\bar{\Phi},) \tag{5.42}$$

where:

$$F^{\tau sij} = \int_\Omega\int_l (D(F_sN_j))^T K D(F_\tau N_i) d\Omega dy_1 \tag{5.43}$$

$$K_{h\Phi}^{\tau i} = \int_\Omega\int_l (D(F_sN_j))^T K d\Omega dy_1 \qquad K_{\Phi\Phi} = \int_\Omega\int_l K d\Omega dy_1 \tag{5.44}$$

note that, $F^{\tau sij}$ is a 1×1 fourth order tensor, $K_{h\Phi}^{\tau i}$ is the 1×3 second order tensor. These two terms represent the fundamental nuclei of the RUC problem for the TC features. In addition, $K_{\Phi\Phi}$ is the 3×3 matrix containing the average TC matrix. The indices of the fundamental nuclei are essential in the CUF approach, as they serve the matrices assembly of the structure. The indices τ and s deal with the expansion functions that approximate the fluctuation functions over the cross-section of the RUC, whilst i and j deal with the shape function of the FEM model in order to build the matrix of the single elements of the structure. For more detailed information about assembling CUF-based finite elements, please refer to [74]. The accuracy of the resolution model depends on the expansion functions chosen for the analysis. In this work, Hierarchical Legendre Expansion (HLE) [66] is employed as F_τ since they combine hierarchical features with the capability to interpolate the cross-section directly. Thus, in the TC problem, the accuracy of the TC field is achieved simply by adding higher-order functions.

By applying the VAM to the (5.42), it is possible to find the linear system that minimizes the functional (5.42):

$$F^{\tau sij}\chi_{\tau i} = -K_{h\Phi}^{sj}\bar{\Phi}, \tag{5.45}$$

Due to the linearity of the problem:

$$\chi_{\tau i}(x) = \chi_{\tau i0}\bar{\Phi},(x) \tag{5.46}$$

with $\chi_{\tau i0}$ of 1×3 dimensions, which contains the fluctuation unknowns that solve the system:

$$F^{\tau sij}\chi_{\tau i0} = -K^{sj}_{h\Phi} \tag{5.47}$$

Through the resolution of the linear system in (5.47), the present method allows the computation of the TC features of the corresponding homogenized material. The effective TC matrix is:

$$K^* = \frac{1}{V}(\chi^T_{\tau i}K^{sj}_{h\Phi} + K_{\Phi\Phi}) \tag{5.48}$$

where K^* is the 3×3 matrix.

Chapter 6

Experimental Studies on Nanoporous Foams

6.1 Introduction

In recent years, nanoscience has become one of the most significant areas of research in new technologies. This knowledge understands the unique properties and behavior of particles smaller than 100 *nm*. It pursues four main objectives by using various sciences: the synthesis of nanostructures, the study of the relationship between the properties of materials and their nanometer dimensions, the design and fabrication of nanodevices, and the creation of new structures using nanomaterials [75].
Due to the exceptional properties of two-dimensional graphene, researchers have studied it in recent years, and a wide range of techniques for the synthesis of graphene-based materials has been proposed [76]. Experimental data show that the graphene monolayer has a Young modulus and intrinsic tensile strength of about 1000 *GPa* and 130 *GPa*, respectively [77]. One way to utilize graphene sheets and graphene-based materials are to employ them in composite materials. Graphene sheets have been widely applied as reinforcements in polymer nanocomposites. A wide range of polymer matrices has been used for various functional materials. One of the most important of them is epoxy, which is a type of thermoset polymer [78]. Most graphene/polymer composites are prepared by in situ polymerization and solution mixing methods, but the problem is that graphene sheets tend to agglomerate due to the strong van der Waals forces, which reduces networking [79]. Consequently,

the dispersion of the reinforcement in the polymer matrix and the expected properties are not achieved. So graphene is challenged for use in the macro dimension. There are many methods such as surface functionalization of graphene sheets or polymer matrix chains, graphene surface modification, graphene alignment in polymer, and exfoliation of graphene sheets to improve the dispersion of graphene sheets within the matrix [80, 81]. However, none of them can still significantly improve the agglomeration problem, and some of them alter the inherent properties of graphene. On the other hand, an efficient way of dispersing graphene sheets in the polymer matrix in the form of three-dimensional graphene hydrogel, graphene aerogel, and thin-film plates have been introduced to solve the dispersion problem [82, 83]. Three-dimensional graphene is an excellent way to reduce two-dimensional graphene problems. These materials have advanced a lot due to their high performance, such as open porosity, lightweight, high pore connection, large surface area, remarkable strength, etc. [84]. GF is one of the carbon foam structures that consist of several graphene sheets and pores.

6.2 Literature Review

Graphene foam (sometimes called three-dimensional monolayer graphene or sponge graphene) is a new material presented in 2011 [85]. In experimental methods for synthesizing GF, the principle is to remove the force between the graphene sheets in the graphite. However, for production of it, there are many methods such as template directing, cross-linking, chemical vapor deposition, and in situ reduction assembly [86], but some efficient methods are still being improved.

Li et al. [87] used the polymer vacuum injection technique in GF to produce highly conductive composites for practical applications such as electronic devices, sensors, actuators, and electromagnetic shields. Bong et al. [88] used GFs as a filter to separate liquids such as water and oil. This measure was necessary to prevent possible environmental pollution and malfunctions of equipment or facilities in the oil industry. Ni et al. [89] produced GF and graphene sheets-reinforced polymer-based composites using RTM. The process of synthesizing graphene was through self-assembly. The most significant challenge in their method was the dispersion of graphene sheets in the composite. They also mentioned that GF-reinforced composites had higher mechanical properties and thermal stability than those containing

graphene sheets. Zhao et al. [90] investigated the effect of carbon fiber on the mechanical and thermal properties of GF/polymer composites. They demonstrated the significant influence of carbon fiber on the resulting composite network bonds using SEM images. Zhang et al. [42] scrutinized the thermal behavior of a polymer composite filled with GF using the finite element method. They found due to the interconnected structure of GF, which forms effective thermal pathways, the polymer composite reinforced with GF has superior thermal properties. Qin et al. [91] in the assembly of GF showed how to produce solid porous materials lighter than air. They illustrated that these solid materials could use for applications such as helium replacement to fill an incapacitated balloon in critical situations. Pedrielli et al. [6] performed computational research using MD approach on the mechanical properties and thermal conductivity of GFs/carbon nanotube. Their study obtained GFs using simulations same as a topology experimentally by growing graphene on nickel nanoparticles. Rahmani et al. [92] presented a model of GF using simulated polycrystalline copper by MD approach, which is used as a membrane to separate gases.

6.3 Synthesis Methodology

The practical application of porous network materials in some applications such as actuators and sensors requires mechanical stability. Therefore, research on the mechanical behavior of nanoporous materials is vital to improving their role in practical applications. In the literature, there are a large number of experimental studies focusing on the yield strength and elastic modulus of nanoporous materials. The behavior of nanoporous materials is completely different from their bulk counterparts.

In this study, the synthesis of GF with the methods available in the literature to obtain the internal morphology of GFs and also to calculate the tensile strength of GF/polymer nanocomposite has been discussed.

6.3.1 Materials

Graphene oxide powder 99% with 3.4-7 *nm* is provided by US Research Nanomaterials, Inc. Ammonia solution 35%, hydroxide acid 57%, deionized water and Acetone were purchased from Swiss-composite.ch. The goal is to convert graphene oxide to graphene hydrogel using reducers such as hydroxide acid, paraffin diamine, ethylenediamine, and ascorbic acid. Epoxy Araldite LY 5052 and Aradur 5052 in a weight ratio of 100 to 38 respectively are prepared from HUNTSMAN chemical company and used in this work.

6.3.2 Preparation of GF

Macroscopic GF is obtained using graphene oxide solution and a relatively simple and cost-effective synthesis method, namely the hydrothermal method, which is combined with the chemical reduction method of graphene oxide solution and the self-assembly method. The purchased graphene oxide is in graphene oxide layers, which are black in color. The following steps have been taken to convert graphene oxide to graphene hydrogel and then graphene aerogel, the so-called GF. Firstly, 99% graphene oxide is mixed with deionized water for 10 minutes, and placed in an ultrasonic bath and centrifuged at 2000 *rpm* for 1 hour. In the next step, a reducing agent of 1.2 in graphene oxide is added to the solution. The solution is placed in an autoclave for 5 hours at a temperature of $120\,^{\circ}C$ to provide carbon atoms bonding conditions. The graphene hydrogel obtained in deionized water is washed to remove all impurities. The resulting solution is stored in 14% ammonia for 24 hours at room temperature. After this step, as shown in Fig. 6.1, the three-dimensionally prepared graphene is hydrogel graphene containing a large amount of water. It is placed in a freeze dryer for 48 hours at a specific temperature and pressure to dry the graphene hydrogel. Finally, three types of samples of GF with different drying percentages are obtained, which are 100%, 95% and 90% dried GF and named as 100-GF, 95-GF and 90-GF, respectively. It must be mentioned, in this work, four samples of each type of GF are synthesis.

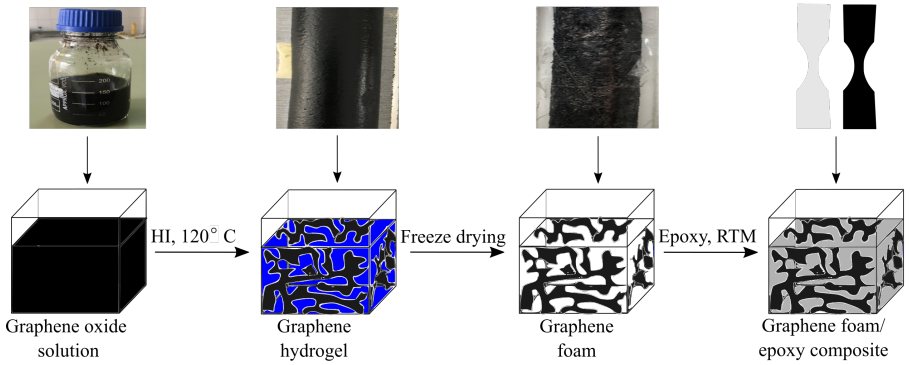

Fig. 6.1 Schematic description of the fabrication process of solution graphene oxide, graphene hydrogel, GF, and GF/epoxy composite.

6.3.3 Fabrication of Epoxy Composites Reinforced by GF

The matrix consists of two parts: Araldite LY 5052, a low-viscosity epoxy resin, and Aradur 5052, a mixture of polyamines. Araldite LY 5052 and Aradur 5052 are clear liquids in the visual aspect, and their density at $25\,^{\circ}C$ (ISO 1675) is 1.17 g/cm^3, and 0.94 g/cm^3, respectively.
Araldite and Aradur are combined in a weight ratio of 100 to 38 and placed in an ultrasonic bath for 10 minutes to obliterate the epoxy bubbles. Next, the temperature of the solution is increased to $70\,^{\circ}C$, with a stirring time is 5 minutes. The synthesized GF is set into the mold, and the prepared epoxy mix is injected into it. The samples are put in a vacuum furnace at the pressure of $60\,kPa$ in two stages for 5 minutes to remove the bubbles and then hardened at room temperature for 24 hours. The mold size is according to the ASTM D638 standard [93]. In applying the tensile test under this standard, it should be noted that this test is used to extract the tensile properties of polymer-based materials and research samples. In addition, this test method is suitable for reinforced and even non-reinforced plastic (polymer) samples under defined environmental conditions. The experimental part including of sample preparation, finishing procedure, and testing. Fig. 6.2 shows the schematic dimensions of the standard model used in this study. The dimensions of the standard ASTM D638 according to type V sample for tensile testing in this study are according to Table 6.1. Each test specimen has a thickness of 1.6 mm. The tensile test is performed by the HOUNSFIELD (H10KS) machine at a speed of 20 ipm for all samples. The maximum limit for this machine is 50 kN force.

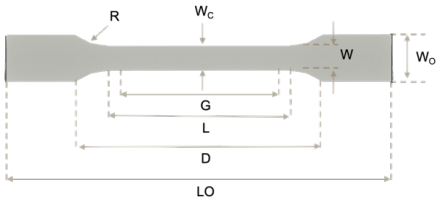

Fig. 6.2 The schematic specimen of the tensile test according to ASTM D638 standard.

Table 6.1 Standard ASTM D638 specimen dimension for tensile testing.

Symbol (see Fig. 6.2)	Dimensions (mm)
W	3.18
L	9.53
W_O	9.53
L_O	63.5
G	7.62
D	25.4
R	12.7

Chapter 7

Atomistic Modelling

7.1 Introduction

Porous nanomaterials that exist in nature both in bulk and in membrane form are one of the categories of nanostructured materials. One example of nanoporous membranes is biological cell walls, which have the ability of selective permeability due to their special morphology. Also, zeolites can be called a bulk nanoporous material that has been used as a catalyst in the industry for years. In recent years, synthetic nanoporous materials have been produced with accurate control of parameters like pore size, pore distribution, porosity, and chemical properties [94]. Due to their unique physical and chemical properties, including extremely high surface-to-volume ratio, exceptional electrocatalytic ability, strain reversibility, and high yield strength, nanoporous materials are popular candidates for medical devices, drug delivery systems, lightweight structural applications, energy absorption devices, and heat sinks [95]. In general, the main goal of nanostructured materials is to reduce the scale of bulk materials to the nanometer scale. But in nanoporous materials, the main interest is to reduce the volume of pores. Most of the essential properties of nanoporous materials come from the structural network of nanopores, such as the size, shape, and intensity of their pores, as well as their surface characteristics. These features make them stand out for different applications and are the reason for the difference between nanomaterials and nanoporous materials. Nanoporous materials' mechanical stability and integrity play an essential role in maintaining their performance in some applications. Therefore, understanding the deformation

mechanisms of nanoporous materials is necessary to calculate the safe lifetime of these materials in scientific applications. Computational studies are easier than laboratory tests due to their low cost. For this purpose, in order to obtain the properties of nanoporous materials, atomic models that represent their morphology are needed. The most important challenge for the numerical simulation of nanoporous materials is their complex morphology, including links randomly connected with different cross-sectional areas. The present chapter shows the computational method developed to generate the atomic model of nanoporous graphene foam (GF) structures and their use in MD simulation to investigate their mechanical, thermomechanical, and thermal behavior. After a detailed literature review of GF nanoporous materials and their atomic modeling, the basic steps of the algorithm are presented. It has been successfully demonstrated that the morphology of nanoporous structures consisting of interconnected networks with random cross-sections can be provided by using a metal substrate. The main idea of this algorithm is to generate sets consisting of random holes under certain restrictions, such as the number of holes and the foam density. It is also shown that the produced foam models are similar to the laboratory-synthesized structural units. After providing a complete description of the atomic modeling process, the results of the MD simulation performed on the atomic GF models with different porosity values are presented.

7.2 MD Simulation of GF and Algorithm Presented for Generated GF

In this work, the structure of GF and its mechanical properties are evaluated by the large-scale atomic-molecular massively parallel simulator molecular dynamics (LAMMPS MD) package [59]. A four-step method has been used to generate the structure of GF. The MD simulation process is briefly shown in Fig. 7.2. In the first step, a metal polycrystalline structure is used for the formation pattern of GF. A random polycrystalline box with dimensions of $10 \times 10 \times 10 nm^3$ consisting of 150 grains of Face-centered cubic (FCC) Au (lattice size = 0.4065 *nm*) is created using Atomsk software [96]. In the second step, the polycrystalline structure is divided into different grains, and some grains are removed randomly, Fig. 7.2(a) and 7.2(b). It should be noted that the final foam density can be controlled by removing the desired number of polycrystalline grains, changing the size of the polycrystals

and the size of the graphene sheets. In the third step, the one-layer graphene sheet created with graphene edge type in a zigzag (x) and armchair (y) directions equal to 0.5 *nm* Fig. 7.1. The simulated monolayers are randomly distributed among the polycrystalline grains by developing a python code, Fig 7.2(c). Next, the AIREBO potential [56] is adjusted between carbon atoms by simulating in atomic phase and periodic boundary conditions. It should be noted that there is no chemical bond between the graphene sheets and the Au atoms, and they are connected using a Lennard-Jones (L-J) potential.

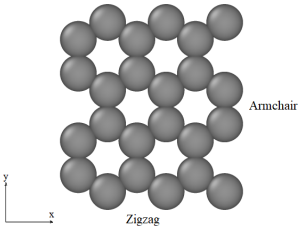

Fig. 7.1 Molecular model of the single graphene sheet.

The process for the simulation of GF in detail is as follows:
There is 1000 single-layer graphene randomly among the Au polycrystalline grains in the box. Each graphene layer has 24 carbon atoms and their bond length is 0.142 *nm*. Carbon atoms with less than 0.75 *nm* distance from Au atoms are removed from the simulation box. At the start of the simulation, the system pressure increases from $1\,atm$ to $1000\,atm$ at $300\,K$ by adjusting the Nose-Hoover barostat and the isothermal-isobaric (NPT) ensemble. The second step uses the canonical (NVT) ensemble for increasing the temperature from $300\,K$ to $3000\,K$. The volume and temperature are kept constant at $3000\,K$ in the third step. In the fourth step, the system's temperature decreased from $3000\,K$ to $300\,K$, and then is balanced at $300\,K$. Each simulation step is performed for $50\,ps$ with a time step of $0.25\,ps$. In this simulation, there are physical bonds between the Au atoms with the graphene sheets. It should be noted that the adaptive intermolecular reactive empirical bond order (AIREBO) potential [56] describes all interactions between carbon atoms in graphene, and boundary conditions are considered periodic in three directions. The Lennard-Jones (L-J) parameters for carbon-Au atoms are obtained by using Lorentz-Berthelot mixing rules from L-J parameters of carbon-carbon and Au-Au atoms [92]. In this study, respectively, the interaction energy and equilibrium distance are $0.0316\,eV$ and $0.3023\,nm$ between Au and carbon atoms. Fig. 7.2(d) shows that in the simulation

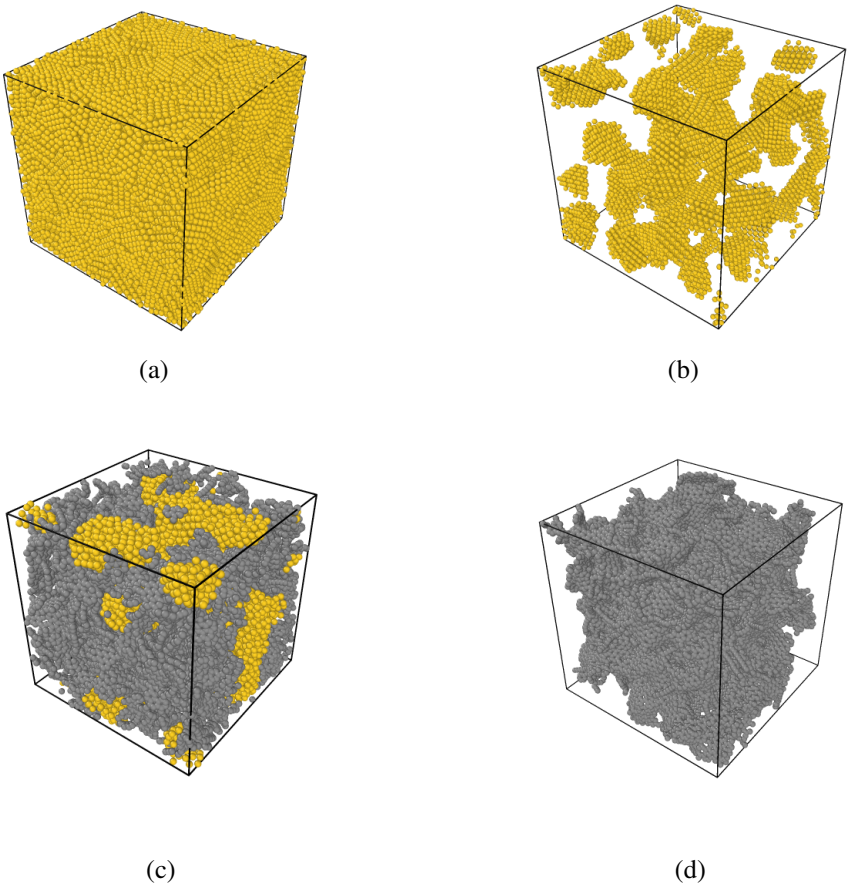

(a) (b)

(c) (d)

Fig. 7.2 The simulation steps for generated GF, (a) The polycrystalline metal lattice is shown to be regular, (b) Several polycrystalline grains by randomization have been removed, (c) Graphene sheets are distributed among the polycrystalline grains and removed if they are too close to the polycrystalline atoms, (d) After heating and cooling cycles, polycrystalline grains are removed and created GF.

box, after forming all the bonds and going through the heating/cooling cycles, the Au atoms are removed, and the final GF is obtained.

7.3 MD Simulation for PDMS Polymer

A linear PDMS chain of 50 -Si-(CH_3)2-O- units for a total of 102 atoms was produced using the cross-platform text-based molecule builder for LAMMPS called Moltemplate. Fig. 7.3 shows the PDMS monomer and simulation of the PDMS nanostructure.

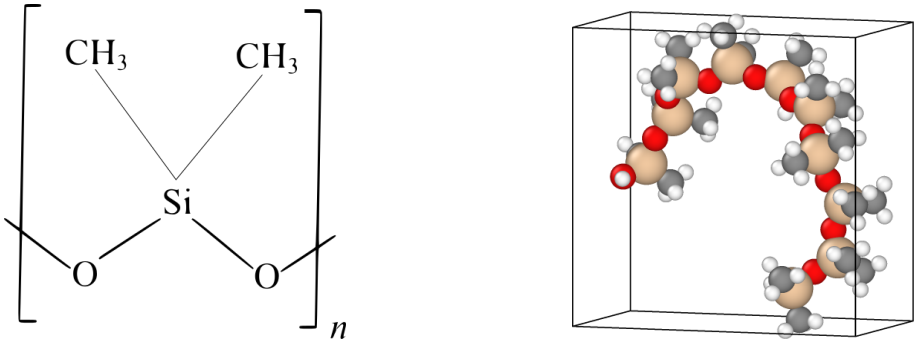

(a) (b)

Fig. 7.3 (a) PDMS monomer, (b) Simulation of the PDMS nanostructure by 10 monomer units.

To establish proper interactions between PDMS chains, PDMS molecules were placed in a larger simulation box with PBC in all coordinates. This system is made of 60 PDMS chains (6120 atoms) and has a volume of about 60 x 60 x 60 $Å^3$. To obtain a dense PDMS, the system is first equilibrated at 300 K using a Nosé-Hoover thermostat (NVT) and then heated to 500 K to transform into nanoparticles and allow atomic repositioning. The system is then cooled to 300 K with a Nosé-Hoover (NPT) barostat and thermostat. The bulk density of the final polymer was set to 0.97 ± 0.05 g/cm^3 to match typical literature values [97]. The Pre-equilibrium and PDMS's optimized structure in amorphous morphology is shown in Fig. 7.4

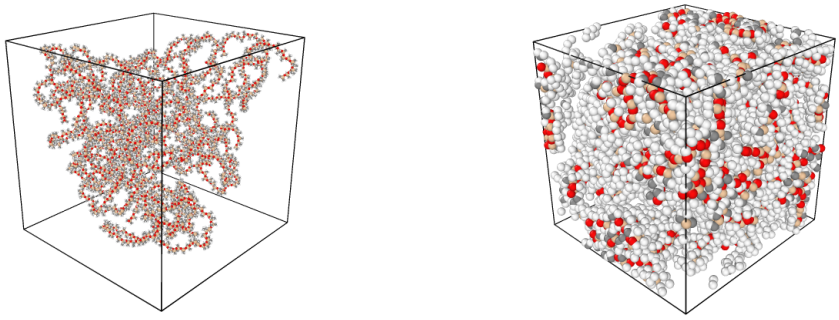

(a) (b)

Fig. 7.4 (a) Pre-equilibrium simulation box containing PDMS chains, (b) The optimized amorphous structure of the PDMS.

7.4 The Mechanical Properties

To calculate the mechanical properties (including Young modulus, tensile strength, and Poisson's ratio) of GF under different loading conditions using MD simulation in the LAMMPS platform is performed. Carbon-carbon atomic interactions were modeled using the AIREBO potential [56]. Atomic simulations were visualized using OVITO [98] or VMD [99] packages. The system is first stable under a temperature of $300\,K$ and zero pressure using a Nose-Hoover barostat and the NPT ensemble. With a uniform velocity distribution, the system equilibrates at a time of $200\,ps$ and a time step of $0.0001\,ps$. To fully describe the fracture regimes in the C-C interaction force, the cut-off parameter of the AIREBO potential is set to 2 [100]. The samples were annealed to randomize the presence of voids in their structure. The samples are heated at 3000 K and then equilibrated at this temperature for 100 ps. Finally, they are cooled down to 300 K at 100 ps using the viscous damping force. Annealing is performed in the NVE. According to the simulations in the tensile regime, all samples were equilibrated at zero pressure and 300 K temperature with a Nosé-Hoover barostat and thermostat. The equations of motion are solved by the Velocity-Verlet integration method using a time step of $0.0001\,ps$. The mechanical properties are evaluated in the ensemble (NPT), and a drag parameter is added to smooth the pressure fluctuations. By applying different strain rates, a controlled uniaxial tensile test of deformation is performed in three directions of structure. Tensile tests are performed along the x, y, and z axes to

ensure computational accuracy and the isotropic behavior of GF. Engineering strain parallel to the deformation direction is defined as follows:

$$\varepsilon = \frac{L - L_0}{L} = \frac{\Delta L}{L}$$

In which L_0 and L are the beginning and current length of the sample in the direction of loading. To define the stress, the pressure stress tensor components in reaction to the external deformation are calculated as [101] :

$$P_{ij} = \frac{\sum_k^N m_k v_{k_i} v_{k_j}}{V} + \frac{\sum_k^N r_{k_i} f_{k_j}}{V} \tag{7.1}$$

where i and j are the label of coordinates x, y, z; m_k and v_k are the mass and velocity of k th atom; r_{k_i} is the position of k th atom; f_{k_j} is the jth component of the whole force on the k th atom due to the other atoms; and, finally, V is the volume of the simulation box. In Eq. 7.1 the pressure consists of kinetic energy (temperature) and virial term. It must be mentioned that the force appears in Eq. 7.1 is the summation of the pairwise, angle, dihedral, improper, and long-range contributions. The calculate stress is the actual stress because the pressure is estimated with respect to the immediate section area of the samples. The applied strain rate is chosen equal to 0.0001, 0.0005, 0.001, and 0.01 ps^{-1}. Stress and strain were saved every 1000 time steps. In this study, Poisson's ratio is also calculated by the following equation.

$$\nu = -\frac{\varepsilon_T}{\varepsilon_L} \tag{7.2}$$

which is characterized as the negative ratio between the transverse deformation ε_T and the longitudinal deformation ε_L.

7.5 The Thermal Properties

7.5.1 Coefficient of Thermal Expansion

The coefficient of thermal expansion (CTE), which measures the change in length, area, or volume of a material with increasing temperature, is an essential parameter for many applications. Although the design of materials with a controlled CTE is crucial today, there is no precise approach to achieving this parameter in GF

materials. In this study, MD simulations are performed in order to calculate the CTE of GF by defining carbon atoms in a cubic region. The AIREBO potential has been used to express the interactions of carbon atoms. The periodic boundary condition is applied in all three directions, and the time step for the simulation is set to 0.001 ps. As the first step, the system temperature is equilibrated under the NVT ensemble at 300 K in 100 ps. In the next step, under constant pressure, the system's temperature is increased from 300 K to 700 K and by using the NPT ensemble equilibrated at 700 K. The simulation is repeated 6 million times by selecting the appropriate damping parameter in each stage. The whole system's pressure, temperature, and energy parameters are controlled during this process. Finally, the axial CTE of GFs for each temperature is calculated using the following formulation.

$$\alpha(T) = \frac{dL}{dT}.\frac{1}{L} \tag{7.3}$$

where the expression dL/dT is equal to the slope of variation of length with temperature. It should be noted that the initial length of the simulation box is at a temperature of 300 K. In order to calculate the CTE, the heating temperature of the system has been converted to linear intervals. In other words, the temperature range between 300 K to 700 K is divided into 20 temperature ranges of 20 K. During the simulation, by heating the system, the length of the simulation box is measured at different temperatures in three directions x, y, and z.

7.5.2 Specific Heat

Several methods of calculating specific heat exist, some of which have an independent temperature and others dependent. In the present study, the calculation of specific heat of GF has been investigated using a formula based on statistical mechanics [102]. Calculating specific heat is the same as calculating the CTE, except that the specific heat is calculated in thermal equilibrium cycles at different temperatures. The NVT ensemble and Nose-Hoover thermostat are applied to achieve equilibrium of simulated GF in the specific heat measurement in the MD platform. Internal energy, enthalpy, temperature, and system's pressure continuously are measured during the simulation. It is worth mentioning that the specific heat in this simulation is specific heat of isochoric ($c_{v*} = (\partial U/\partial T)_V$) [103]. The isochoric specific heat can be calculated as:

$$c_{v*} = \frac{< U^2 > - < U >^2}{k_B T^2 m} \tag{7.4}$$

in which $< ... >$ represents the mean of the variable. There is no doubt that by multiplying the density by the specific heat, heat capacity is obtained.

7.5.3 Thermal Conductivity

The two essential methods used to calculate the Thermal Conductivity (TC) of nanostructures through MD simulations are:
1. Equilibrium molecular dynamics (EMD) method
2. Non-equilibrium molecular dynamics (NEMD) method
The EMD method is based on the use of the GREEN-KUBO formulation to obtain TC, which is based on the integral of the heat flux correlation function [104]. The NEMD method calculates the TC according to Fourier's law, which computes the heat flux by defining hot and cold regions [105]. These two methods have their advantages and disadvantages. For example, the EMD method is used to calculate the TC in all directions, but the NEMD method requires the calculation of a thermal gradient that calculates the TC in only one specific direction. The NEMD method is used to calculate the TC of GF and polymer. Since the foam structure is unstable, the EMD method cannot be used. In this work, TC in the atomic phase for PDMS and GF is calculated by applying periodic boundary conditions along each direction, and the simulation time step is set to $0.0005\,ps$. As a first step in the MD simulating for TC calculations, the temperature of reached 300 K per 100 ps assuming the NPT and NVT ensembles. The simulation box is then divided into 100 parts of equal length. The first and last layers are called the cold sink and the hot source, respectively. After the equilibration step, the sample's temperature gradient is created by exchanging kinetic energy between hot and cold zones under the microcanonical (NVE) ensemble. With a temperature difference of 20 K from the initial temperature of 300 K, the energy exchange is achieved by subtracting some energy from the hot zone while adding the same energy to the cold zone. The energy exchange is performed every 25 steps for a period of 500 ps, and the unit heat flux J_x is obtained as a result of this energy exchange is calculated by Eq. (7.5):

$$Q = J_x = \frac{q}{A} = \frac{\frac{dE}{dT}}{A} \tag{7.5}$$

which, J_x is the heat flux in the x-direction, A is equal to the area. Each coordinate's average temperature can be calculated to determine the temperature profile along the heat flow direction. To calculate the temperature in different coordinates during the simulation, start with the chunk atom command with the minimum value of x (meaning length) to measure the temperature at any point in the system, then the temperature changes at any point in the simulation box are calculated.

$$q = -kA\, dT/dx \tag{7.6}$$

where in Eq. (7.6) k is the TC, $^{dT}/_{dx}$ is the thermal gradient and J_x the heat flux ,respectively. To accurately calculate the TC values, the total simulation time must be long enough that the computation time in this work is considered at 15,000 ps. It is worth being mentioned, for GF two potentials of the adaptive intermolecular reactive empirical bond order AIREBO [56], and Tersoff [106, 107] have been used to obtain the TC for three directions x, y, and z. These two allow the formation and separation of covalent chemical bonds during simulation. Although these models are classical, they do provide an accurate description of the process of covalent bonding of atoms. Several studies have investigated the different thermal properties of some filler

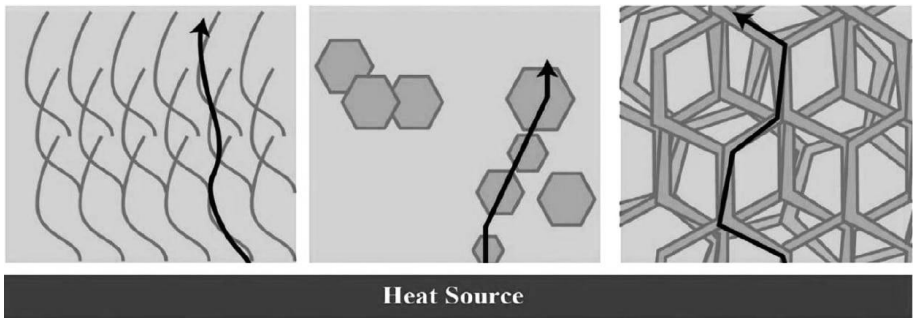

Fig. 7.5 Thermal electron transport in the composites reinforced with carbon-based nanomaterials.

materials, such as graphite, carbon nanotubes, and graphene, in polymer matrices, which improved the thermal performance of polymer nanocomposites [108, 109]. Expanding research on the injection of polymers into GF has been shown to improve the thermal properties of polymer composites. Fig. 7.5 schematically describes the thermal electron transfer process that occurs in polymer matrices reinforced with GF, 2D, and 1D carbon-based nanomaterials [110]. Phonons and electron transfer from the heat source to the reinforced composites, resulting in thermal energy transfer. It

can be stated that thermal electron transfer in one-dimensional and two-dimensional carbon requires a high volume fraction or their alignment, while foam with a low volume fraction allows thermal electron transfer to be transferred well and increases the performance of composites reinforced with GF.

Chapter 8

Results and discussion

8.1 Results and Discussion for Mechanical Properties

8.1.1 Characterization of the Experimental Morphology

The synthesized GF has a black color and porous structure. Raman spectroscopy and SEM techniques are used to determine the characteristics of synthesized GF. In all experiments, Raman spectroscopy with specifications (Teksan model) and YAG laser with a wavelength of 532 *nm* are used. Graphene oxide and GF are analyzed by Raman spectroscopy to determine the chemical properties and evaluate the transform of graphene oxide to GF. Fig. 8.1 shows that a strong peak (G-band) and a weak peak (D-band) occur in the Raman spectra. The G band is activated in sp^2 carbon hybridization of the base material and indicates in-plane vibration mode. The D band is activated when defects in the Raman scattering resonance occur near the K point in the Brillouin region and show sp^3 hybridized carbon. Therefore, the peak intensity ratio from D to G, which is often used to estimate the sp^2 domain size of carbon, i.e., $I_D \backslash I_G$, increases from 0.752 to 0.896 after converting graphene oxide to GF. This ratio shows the primary oxygen-containing groups removed from the graphene oxide sheets and the sp^2 regenerated carbon structure. In addition, the increase in the G-band peak indicates the reconstruction of a hexagonal lattice of carbon atoms.

Also, the morphology of GF is observed by the scanning electron microscope (Mira Teskon). Fig. 8.2 shows a piece of GF with SEM images at various magnifications of 200 μm, 20 μm, 1 μm, and 200 *nm*, respectively. GFs have a three-

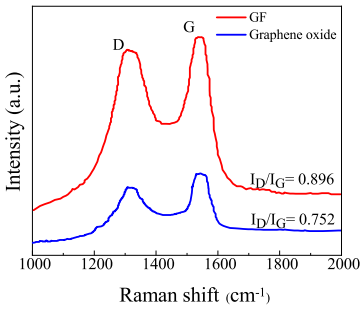

Fig. 8.1 Raman spectroscopy of graphene oxide and GF.

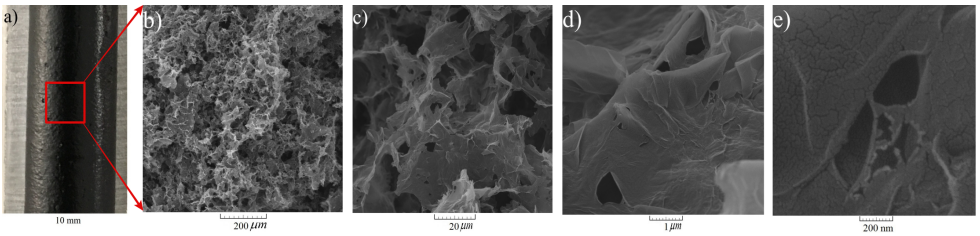

Fig. 8.2 (a) Image of synthesized GF. (b-e) SEM images at different magnification.

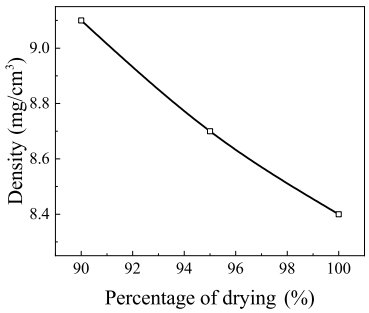

Fig. 8.3 Relation between mass density and drying percentage of synthesized GFs.

dimensional porous network with interconnected pores. In the morphology of the GF surface, the porous structure with many wrinkles is observed, indicating the formation of a three-dimensional GF structure through the accumulation and binding of reduced graphene oxide sheets. By further magnifying the images, it can be seen that the structure has many links that are expected to provide mechanical reinforcement. According to SEM images, it is found that drying of GFs at different levels did not affect the average shape of the pores. The drying percentage caused the density of the obtained samples to be different due to the rate of liquid remaining in the foam. The density of the resulting GFs with different drying percentages is shown

in Fig.8.3. Increasing the drying percentage of GF has reduced the density of the foams. SEM images and Raman spectroscopy approve the formation of GF.

8.1.2 GF/Epoxy Composite Experimental Tensile Test

In order to evaluate the effect of GF on the GF/epoxy composite, tensile tests have been performed. Fig. 8.4(a), 8.4(b), and 8.4(c) show the strain-stress curve, Young modulus, and tensile strength for epoxy and three types of composite samples reinforced with 100-GF, 95-GF, 90-GF. The maximum of Young modulus and tensile strength belong to the sample that consists of 100-GF and has increased about 138% and 48%, compared to epoxy, respectively. These increases indicate a network in the reinforcement and stress transfer from the matrix to the GF. The three-dimensional network causes regular stress and strain distribution in the whole of the composite. Therefore the synergistic effect of nanoparticles on epoxy is evident. The three-dimensional bond between the sheets causes GF to act as a barrier to the aggregation of graphene sheets in composites.

Fig. 8.4(b) shows the average drying percentage of GF relative to the Young modulus of composite reinforced with it. It can be seen that with rising drying percentage and reducing liquid volume in GFs, the resulting composite has a higher Young modulus. The 100-GF/epoxy sample has a Young modulus of 26% higher than the 95-GF/epoxy sample and 14% higher than the 90-GF/epoxy sample. It must be mentioned that to calculate the Young modulus, the criterion is placed on a strain of 1.5%. In lower strains, the Young modulus of the samples is close to each other and has similar behaviour. While in higher strains, it is the potential for failure and does not provide the necessary safeness for experimental reporting of Young modulus. Therefore, in this research, the benchmark for calculating the Young modulus of experimental tensile tests is 1.5% strain. Also, from Fig. 8.4(c), it is clear that the tensile strength of 100-GF/epoxy composite increased by 28% and 20% compared to 90-GF/epoxy and 95-GF/epoxy composites, respectively. The composite fabrication conditions and weight percentages $\sim$0.5wt% of reinforcement are the same in all samples, but the GF synthesis method is different in the drying step in the laboratory. It should be noted that the GF in these composites is obtained through pre-synthesized. In the 100-GF/epoxy composite, GF is 100% dry, and all viscous motion is minimized; it has the highest resistance to tensile stress compared to the other two types. In the 95-GF/epoxy composite, Young modulus and tensile

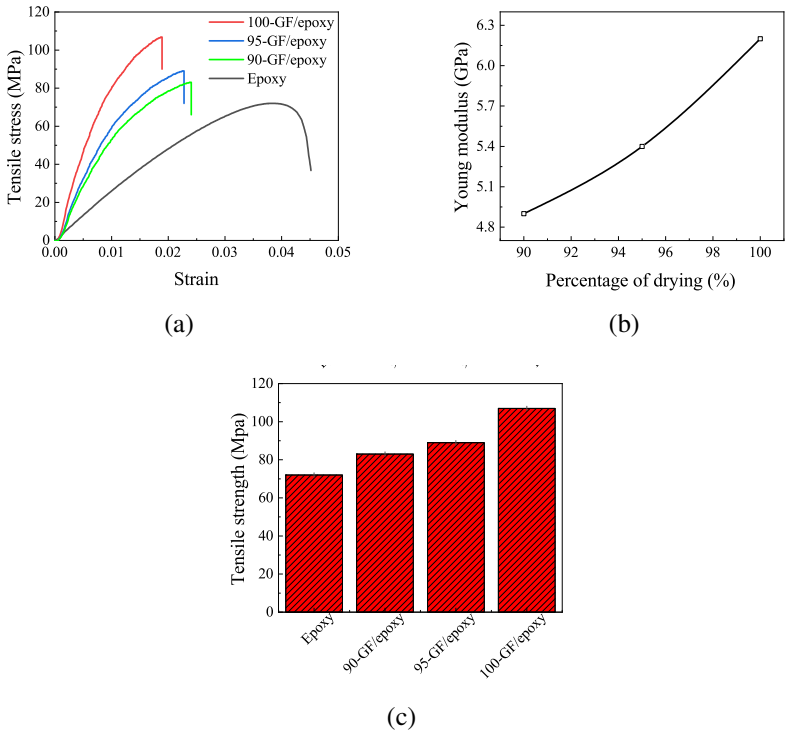

Fig. 8.4 (a) Tensile strain-stress curve of epoxy and GF/epoxy composites, (b) The average drying percentage of GFs versus the Young modulus of composite, and (c) Tensile strength of epoxy and composite with different GFs.

strength are weaker than the previous samples. In the 90-GF/epoxy composite sample, the Young modulus and tensile strength are weaker than the other samples, but the strain percentage is higher. Since 10% of water remains in the GF structure, this structure is softer than other samples. It is also inferred that the strain percentage increases for the 90-GF/epoxy samples, but the Young modulus and tensile strength decrease due to the lower weight percentage of epoxy in this type of composite. The 100-GF/epoxy sample is more brittle than the two other samples. If the goal is to increase the strain percentage of the composite, in addition to having a high Young modulus and high tensile strength, or in other words, the composite fails later; the 90-GF/epoxy sample is the best. Also, it can be recognized that increasing the Young modulus and tensile strength in GF/epoxy composite samples means they are more resistant to axial load in comparison with epoxy samples.

Table 8.1 Comparing the increase in Young modulus of GF composites to their polymer matrix.

Composite type	Increase in Young modulus (%)	Filler content (wt%)	Pore size (μm)
GF/PMMA [111]	80	~ 0.2	-
GF/Epoxy [89]	75	0.29	10-100
GF/Epoxy [112]	53	~ 0.3	10-100
GF/PDMS [90]	66	0.5	40-300
GF/Epoxy [113]	94	0.5	20-200
GF/Epoxy [this work]	138	0.5	10-200

In order to excel the method performed in this work, the results such as the Young modulus and tensile strength compared to other works are given in Table 8.1. According to the table, it can be detected that for the GF/epoxy composite, the Young modulus has a significant increase compared to the other works cited. In all the mentioned composites, the weight fraction of the reinforcement and the size of the pores had approximately similar values.

8.1.3 Characterization of the Numerical Morphology

There are some criteria like experimental tests for validating the structure of simulated GF, which can be used to ensure the simulated form. Based on these criteria for generating GF, the heating/cooling cycle is repeated in five-times. The graphene flake is compressed from the gas to the solid state by repeating. Each cycle increased the system temperature from $300\,K$ to $3000\,K$ in $250\,ps$ and equilibrated at $300\,K$. At the end of each cycle, the radial distribution function (RDF) diagram, density, and the number of carbon-carbon covalent bonds are measured. RDF diagram at the end of three first cycles with pre-cooling and heating cycle is shown in Fig. 8.10(a). This diagram shows that the first peak occurred at 1.42 Å, i.e., the C-C bond length in graphene sheets. This peak intensity increases with each heating and cooling and can also be seen in the C-C bond diagram. Fig. 8.10(b) illustrates the actual number of C-C bonds in each cycle. The total number of C-C bonds per carbon atom is converged with the criterion of the number of carbon atoms in ideal graphene (1.5 per carbon atom). In this work, the number of bonds is calculated using the distance criterion < 1.6 Å for two carbon atoms. Here the results of the three-dimensional porous structure are in agreement with the works of Qin et al. [91].

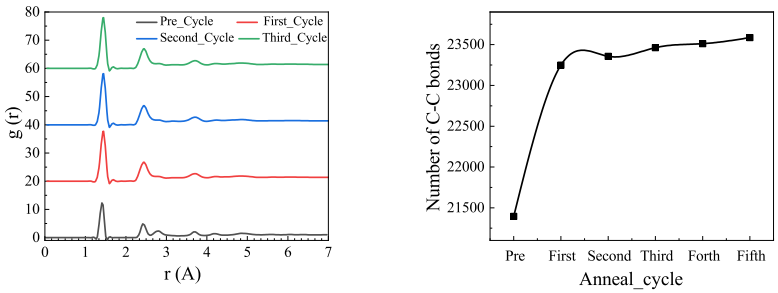

(a) (b)

Fig. 8.5 (a) Radial distribution functions (RDF) related to heating/cooling cycles of the system, (b) The total number of covalent bonds at the end of each cycle.

After the heating and cooling cycles and removing the Au atoms, a stable structure of three-dimensional GF is obtained. Fig. 8.6 shows the SEM image of one of the experimental GF-100 % dried samples compared to the simulated one at the same porosity percentage. The topology of the GF simulated is inspired by experimental synthesis GF, but it must be noted that the pore sizes in the experimental synthesis samples are larger than the simulated models. Most graphene sheets in walls are adjacent to the junction of several curved joints. Defects cause this curvature in the shape of a pentagon and a hexagon at the boundary, which appears deformation outside the surface.

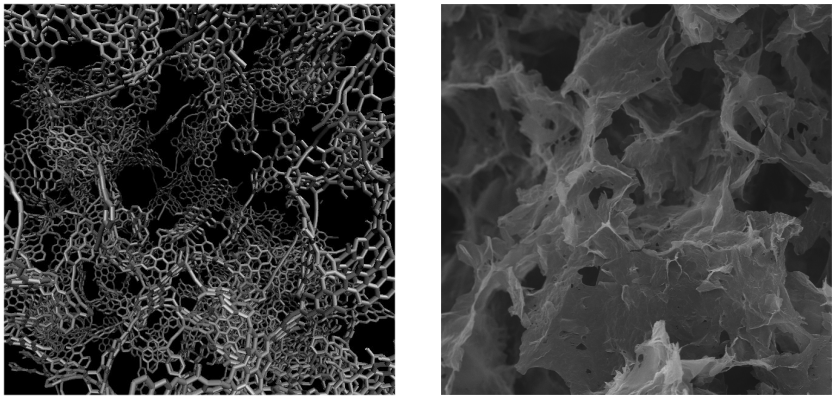

(a) (b)

Fig. 8.6 (a) GF simulated after relaxation stage in dimensions of 100×100 Å^2 compared to (b) The SEM image, in dimensions of 80×80 μm^2.

8.1.4 Tensile Response of Simulated GF under Uniaxial Loading

To investigate the mechanical properties of GF under different loading conditions, simulations are performed using LAMMPS MD. The system is first stable under a temperature of $300\,K$ and zero pressure using a Nose-Hoover barostat and the NPT ensemble. With a uniform velocity distribution, the system equilibrates at a time of $200\,ps$ and a time step of $0.0001\,ps$. Fig. 8.8(a) shows the equilibrated system structure before stretching. To fully describe the fracture regimes in the C-C interaction force, the cuts-off parameter of the AIREBO potential is set to 2 Å [100].

The graph of temperature changes is shown in Fig. 8.7(a), which converges at a temperature of 300 K, and the tensile test is performed at the same temperature after the relaxation step. Fig. 8.7(b) shows the graphs of variation in the stresses of the x, y, and z directions, and the pressure with respect to time converges around zero at the stabilization step of the GF structure. Fig. 8.7(c) shows the potential energy and total energy diagrams of the system over time that structure energy is minimized. All these diagrams show that they have converged to a single number and, as shown in the figures, the system is in a stable state and has not been aroused or broken. By converging the changes in temperature, stress, potential energy, and energy of the whole system with respect to time to a specific value, the system's stability before the employment of the strain rate is guaranteed. Fig. 8.8(b) shows a snapshot of the structure during stretching simulation after the relaxation step in the x-direction. By applying different strain rates, a controlled uniaxial tensile test of deformation is performed in three directions of structure. Fig. 8.9(a-d) show the strain-stress curves of simulated GF under uniaxial tension in 0.0001, 0.0005, 0.001, and 0.01 ps^{-1} strain rates, respectively. Tensile tests are performed along the x, y, and z axes to ensure computational accuracy and the isotropic behavior of GF. It is observed that at $300\,K$, the increase in strain rate has no significant effect on the linear Young modulus. As the strain rate increases, the tensile strength increase. In particular, for each strain rate, two or three independent simulation tests are performed with different initial configurations, and the calculations are repeated several times.

The strain parameter in the direction parallel to the deformation is defined as $\varepsilon = (L - L_0)/L_0$, where L and L_0 are the current and initial lengths of the simulation box. The pressure stress tensor on each atom in the simulation box is calculated based on relations in reference [101] to determine the system stress. Finally, the strain-stress diagram is computed to estimate the Young modulus at each strain rate.

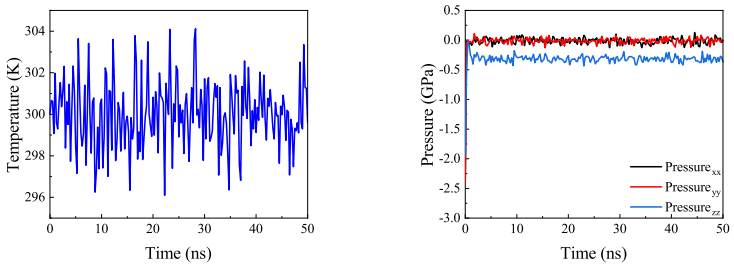

(a)

(b)

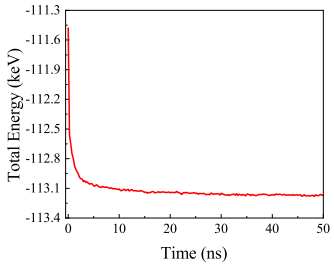

(c)

Fig. 8.7 The molecular dynamics results for the variation of (a) Temperature, (b) Pressure, and (c) Energy of GF structure by simulation time rise after relaxation and before tensile loading applied.

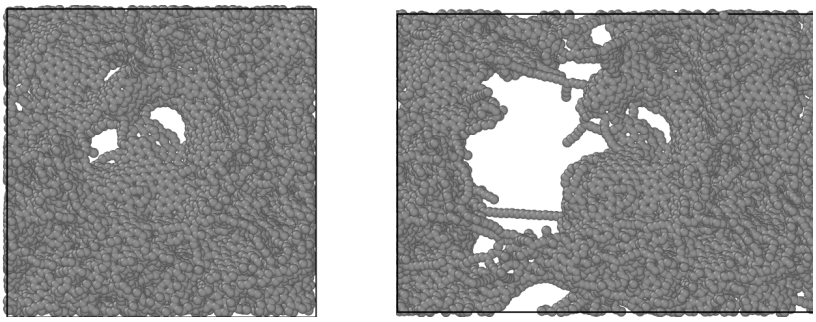

(a) (b)

Fig. 8.8 (a) GF structure simulated at equilibrium before the tensile test, (b) Snapshot of structure in the tensile test.

It should be noted that with decreasing strain rate, computational time increases, so in this study, the average strain rate of 0.001 ps^{-1} is selected because it shows the most optimal results. In addition, the Poisson ratio is calculated by defining axial and lateral deformation. The Young modulus and tensile strength of GF are equal to

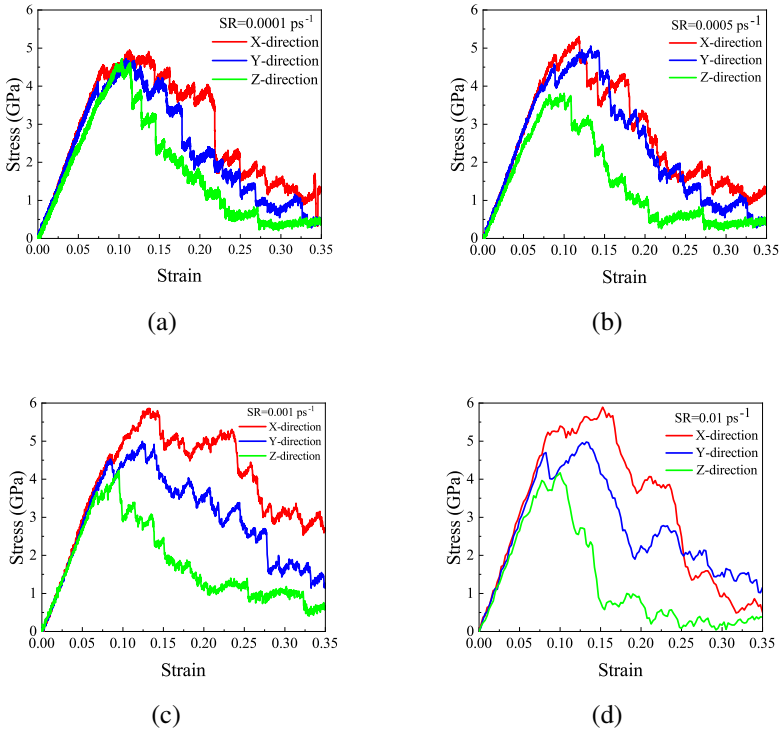

Fig. 8.9 Strain-stress diagram of simulated GF under tension along the x, y, and z axes and strain rate of (a) 0.0001 ps^{-1}, (b) 0.0005 ps^{-1}, (c) 0.001 ps^{-1}, (d) 0.01 ps^{-1}.

the value of about 36 GPa and 5.5 GPa, respectively. For completeness, the results of MD simulations validate with reference [91] (mass density: 0.83 g/cm^3, Young modulus: 36.6 GPa).

8.1.5 Multi-Scale Model of GF/Epoxy Composite based on CUF

This section performs the GF/epoxy composite tensile test analysis using a multi-scale method, CUF-MSG micromechanical code, by considering an RUC. In Table 8.2, the Young modulus and Poisson ratio of GF is calculated from the MD method in this study. These two parameters for epoxy are taken both through the experimental process in this study and MD results in reference [114]. The effective Young modulus and the Poisson ratio of GF/epoxy composite are obtained from the multi-scale approach. Finally, the results obtained from the CUF-MSG micromechanical model are compared with the experimental results. The difference between the numerical

multi-scale model output and the experimental results is about 1.5%, which is a good agreement that has been reached. The small difference between the numerical and the experimental results are for the existence of some parameters in experimental work that are still unknown in numerical methods. Also, some simplifying assumptions in numerical methods can cause differences between them.

Table 8.2 Comparison of the Young modulus and Poisson ratio of GF, epoxy and GF/epoxy composite between experimental and numerical methods

Type of matrial	Young modulus (GPa)	Poisson ratio	Method
GF	36	0.33	MD
Epoxy	2.6	0.29	MD[114]
Epoxy	2.54	-	Experimental
GF/epoxy composite	6.2	-	Experimental
GF/epoxy composite	6.3	0.29	CUF

8.1.6 Summary

In the present work, GF samples were synthesized using a highly efficient and cost-effective method with different drying percentages. The foam structure was guaranteed and observed using the Raman technique and SEM images. The density of the synthesized samples was inversely related to their drying percentage, and the lowest mass density belonged to the sample that was 100% dried. By comparing the results of tensile test for GF/epoxy composites with different mass densities GFs, it was found that the composite reinforced with 100-GF samples has a maximum Young modulus. By raising the drying percentage and reducing liquid volume in GFs, the resulting composite has a higher Young modulus. Also, as a significant result, the composites that contain wet GFs have less tensile strength, but their strain percentage is higher than fully dried GFs. The highest Young modulus and tensile strength of the composite include 100% dried GF with 0.5 wt%, which increased by 138% and 48% compared to epoxy, respectively. It can also be concluded that the liquid in 90-GF and 95-GF samples act as an obstacle to matrix transfer in all parts of the foam and do not increase the mechanical properties compared to 100-GF/epoxy composites. By adding GF to the polymer composite, the Young modulus can be increased from twofold to threefold by control of the fabrication method and synthesis of reinforcement. Furthermore, in this work, the brittleness of the composite can be controlled by the drying percentage of GF samples. Moreover, by simulating the

structure of GF in the LAMMPS software by distributing graphene sheets randomly, the results were closer to the experimental outcomes. In particular, the simulated GF was confirmed in density, the number of carbon-carbon bonds, and RDF diagrams with the experimental sample. It should be noted that the GF simulation added no chemical functional groups to the graphene structure. GF isotropic behavior was proved after simulating the tensile test at different strain rates. The Young modulus calculated by the multi-scale numerical model has a difference close to 1.5% with the experimental Young modulus, which is acceptable. The Poisson ratio of the GF/epoxy composite was also calculated numerically, a value used to evaluate the transverse response of the composite to deformation. Nevertheless, GF, in addition to preventing the accumulation of graphene sheets in polymer composites, also has a high mechanical performance as polymeric reinforcements for structural applications that require low weight as well as high tensile strength and Young modulus. Because of the remarkable properties of GFs and polymer composites reinforced with these foams, the thermal properties of them stay to be studied in forthcoming research.

8.2 Results and Discussion for Thermoelastic Properties

8.2.1 Characterization of Numerical GF Morphology

This study uses a multi-scale method to achieve the elastic and thermoelastic properties of GF reinforced composites. In this regard, four types of GF with different densities and porosity percentages are simulated to calculate their properties. The validity of the initial structures obtained from GF is ensured using criteria of density, radial distribution functions (RDF), number of carbon-carbon (C-C) bonds, and pore size distribution (PSD). Figure 8.10(a) shows the RDF diagram for the simulated GFs at the end of three heating and cooling cycles plus the pre-heating and cooling cycle. As illustrated, the first peak occurred at 1.42 Å, i.e., the C-C bond length in the graphene sheets. This peak intensity increases with each cycle which can also be seen in the C-C bond diagram. Figure 8.10(b) shows the actual number of C-C bonds per the number of atoms in each cycle. This bond number increases as the cycles increase to approximately converge with the number of bonds in ideal graphene (i.e., 1.5 per atom).

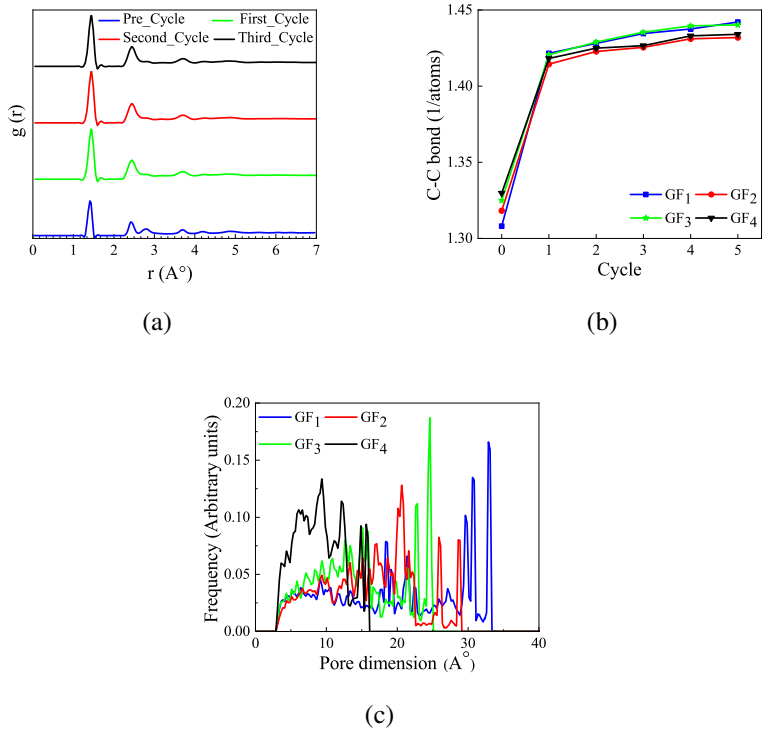

(a) (b)

(c)

Fig. 8.10 (a) Radial distribution functions related to heating/cooling cycles of the system, (b) The total number of covalent bonds per number of atoms at the end of each cycle, and (c) Pore size distribution for all groups of GF.

Geometric analysis of GFs and their porosity are performed using the PoreBlazer code [115]. The pore size in GFs structure can be obtained using the PSD, which is the same as the rate of absorption and desorption of gases in the laboratory method. PSD analysis provides a numerical description of the pore size range in samples. The PSDs for GF types are shown in Fig. 8.10(c). In this work, the specific surface area of GF has been calculated in reference to its excellent surface properties due to the 3D bonds. The PSD measurements provide a numerical description of average pore dimension, porosity percentage, and specific surface area, which are reported in Table 8.3 for all groups of GFs. Indeed, as displayed by the PSD diagram, the pore size is approximately in the range of 0.5 nm to 3 nm. The mass densities range for GFs is between 0.5 - 0.8 (g/cm^3), which is shown in Fig. 8.11(a) the relation between it and average pore dimensions. And also, Fig. 8.11(b) shows the mass density graph versus the samples' specific surface area. It is evident that the specific surface area decreases with the increase in density, implying that the pore

size also reduces with the growth in density because the pore dimension is related to the surface area. The high specific surface area in the low mass creates enough space for electrochemical and thermal reactions, which increases the capacity of electrical devices. With the decreasing porosity, the specific surface area is reduced, too. Actually, in GFs, energy can be stored more efficiently due to their low mass and high specific surface area. The PSD diagrams of the simulated GFs are compared with the experimental samples from references [5, 6], and a good agreement can be appreciated. Figure 8.12 shows a representative piece of the same size for each of the foam types that the percentage of porosity decreases from *a* to *d*, and the mass density increases. The topology of the samples simulated in this study is similar to the SEM image shown in Fig. 8.13. Of course, it should be noted that the pore size in laboratory samples is much larger, about a few micrometers.

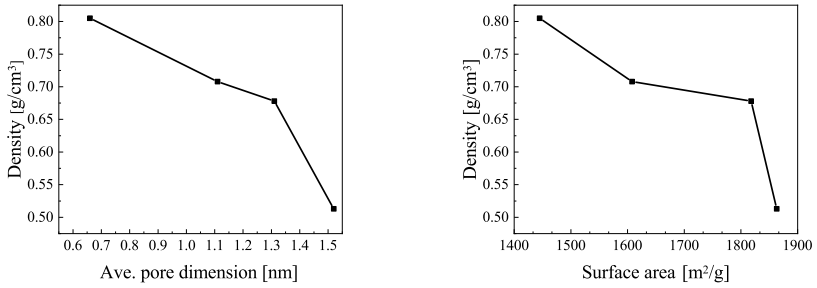

(a) (b)

Fig. 8.11 (a) The diagram of density versus average pore size and (b) Specific surface area for the GF samples.

Table 8.3 Parameters describing the four groups of GF scrutinized.

Sample	Density (g/cm^3)	Porosity (%)	Avarage pore size (nm)	Surface area (m^2/g)
GF_1	0.513	78	1.52	1863
GF_2	0.678	70	1.31	1818
GF_3	0.708	66	1.11	1608
GF_4	0.805	63	0.66	1445

The Young modulus diagram of graphene foams simulated in this work is compared with the references shown in Fig. 8.14. As the density increases, the Young modulus also increases. In this study, the Young modulus of random foams was calculated in the strain range of 5-8% and at a temperature of 300 K. In ref. [6], the Young modulus has been measured in the same range and temperature in regular

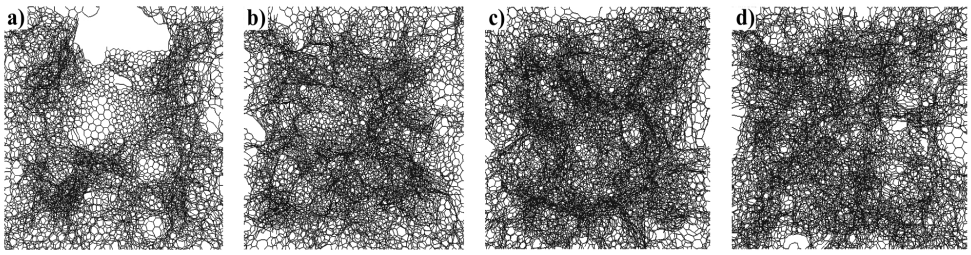

Fig. 8.12 A similar part of a UC taken from four types GF with different porosity (a) 78% (b) 70% (c) 66% (d) 63%.

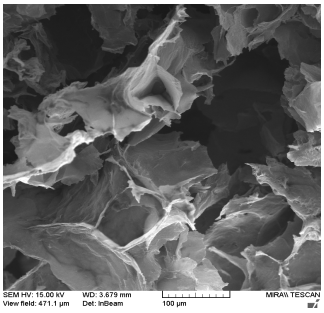

Fig. 8.13 SEM image of a 3D GF with a matching topology studied in present work [5]

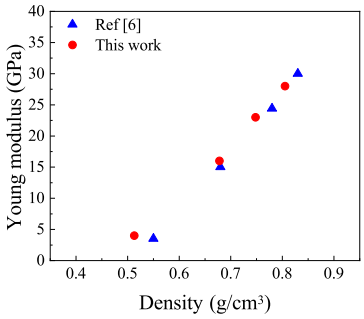

Fig. 8.14 The Young modulus of GF groups in comparison with references [6].

forms. It is clear that the foams modeled in regular form have a higher Young modulus than random foams due to the carbon atoms' connections.

8.2.2 CTE and Specific heat of GF

The variation of coefficient of thermal expansion (CTE) relative to temperature is plotted for all types of GF samples, and the results are shown in Fig. 8.15. For sample

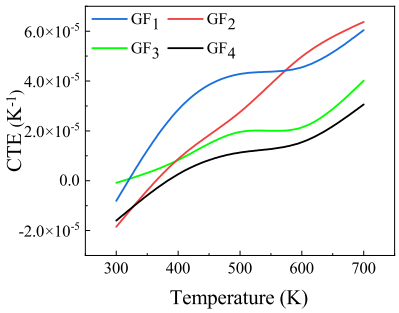

Fig. 8.15 The CTE as a function of temperature for all groups of GFs.

types of GF, the CTE starts with a negative value at a temperature of 300 K, which these values increase at higher temperatures and agree with the experimental results of references [116–118]. Also, the negative CTEs show the powerful coupling of the carbon bonds and foam connections at lower temperatures. Actually, at temperatures between 300 K to 700 K, the value of CTEs for all GFs changes with increasing trend because this temperature range is lower than the Debye temperature in graphene [119]. The value of CTE for GF_1 is more than GF_2 at lower temperatures, but at higher temperatures, the CTE's value of GF_1 is less than GF_2 while the opposite trend is valid for GF_2 and GF_3, this contrasting behavior is explained mainly due to the separated bonds of the samples in this temperatures regime. The non-linear behavior in CTE is due to the internal rearrangement of the graphene layers in GFs at different temperatures. By raising the temperature, carbon atoms in the simulation box will move more, so the CTE's value is increased. It is found that the variation of CTE in GF_1 and GF_2 is more than this value in GF_3 and GF_4. Its reason is the difference in the density and connection of the foams. The density of GF_1 and GF_2 is lower compared to GF_3 and GF_4. The behavior of CTE for GFs at different densities and porosity varies and depends on the temperature, internal energy, and coordinates of carbon atoms.
Moreover, as another explanation for the behavior of GFs' CTE, it can be pointed to CTE's relationship with intrinsic energy and the anharmonicity of the interatomic potential. Like a solid system, this manner is founded on inherent phonon energy [120].

Further, the specific heat is calculated by computing the system's internal energy for all types of GF samples. The values of the CTE, specific heat and heat capacity at 300 K and 400 K are presented in Table 8.4. It can be deduced that the value

Table 8.4 The thermoelastic properties of GFs by MD simulations.

Sample	T=300 K			T=400 K		
	SH* (J/g.K)	Heat capacity (10^6 J/m^3.K)	CTE (10^{-6} K^{-1})	SH* (J/g.K)	Heat capacity (10^6 J/m^3.K)	CTE (10^{-6} K^{-1})
GF_1	3.65	1.87	−8.08	3.78	1.94	33.3
GF_2	3.02	2.04	−18.5	3.08	2.09	8.69
GF_3	2.55	1.80	−5.13	2.69	1.90	2.62
GF_4	2.33	1.87	−1.31	2.35	1.89	0.89

* In this table, SH is used instead of specific heat.

of specific heat decreases for all samples with decreasing porosity. Additionally, it is clear that the heat capacity value for each sample depends on mass density. At 300 K, the first type GF with the lowest density has the maximum specific heat, and the fourth one with the highest density has the minimum specific heat. Also, rising temperature causes the value of specific heat increases for all samples. On the other hand, in the present numerical conditions, an attempt has been made to use the potential that is most consistent with the experimental conditions, but because quantum effects are not considered, it may cause a slight difference in the results with experimental conditions. The high specific heat of GFs shows that with low mass and high porosity, these materials are able to store high energy. Therefore, GFs are also used as batteries and energy storage in addition to structural and thermal applications.

8.2.3 Multi-scale Method of GF/PDMS based on CUF

In order to calculate the thermoelastic properties of the homogeneous GF/polymer composites by the CUF-MSG micromechanical model [63, 121], the heterogeneous UC information, including GFs and PDMS (Sylgard 184) matrix, is presented. Table 8.5 provides the values of Young modulus and Poisson ratio for the GF samples from the MD simulation in this study. The Young modulus for each GFs type in this study at temperatures between 300 K and 400 K is assumed to be constant, and the slight difference between them is ignored. Also, Poisson ratio for GFs is considered temperature-independent. The properties of the PDMS matrix are listed in Table 8.6 using references [122, 123]. It should be noted that the PDMS is a cross-linked elastomer, and its behavior is in contrast with thermoplastic polymers. The modulus of PDMS increases with temperature because of the increased Brownian motion,

leading to the stretched molecular segments tugging at their *anchor points* and taking a more likely coiled-up shape [124]. PDMS's density is 0.97 g/cm^3, and its Poisson ratio at all temperatures is 0.499.

Table 8.5 The elastic properties of GFs by MD simulations in present study.

Material	Young modulus (GPa)	Poisson ratio
GF_1	4	0.27
GF_2	19	0.27
GF_3	23	0.29
GF_4	27	0.33

Table 8.6 Properties of PDMS matrix from references.

Temperature (K)	Young modulus (MPa)	Specific heat (J/g.K)	Heat capacity $(10^6 J/m^3.K)$	CTE $(10^{-6} K^{-1})$
300 [122]	1.4	1.45	1.40	285
400 [123]	2.2	1.65	1.60	275

Table 8.7 is presented to validate the MD method for GFs as well as the micro-thermoelastic CUF-MSG model for the effective properties of the composite used in this work. For this purpose, graphite and graphite/epoxy composite properties are calculated using the MD and micro-thermoelastic CUF-MSG models, respectively. The results obtained by numerical methods are compared to those obtained by the experimental procedure in reference [8]. These comparisons demonstrate that numerical methods provide accurate results.

Table 8.7 The comparison of the MD and the micro-thermoelastic CUF methods outputs with experimental results in ref. [8].

Material	Method	Young modulus (GPa)	Poisson ratio	Specific heat (J/g.K)	CTE $(10^{-6} K^{-1})$
Graphite	Experimental	5	0.23	1.57	5
Graphite	MD	5.08	0.23	1.61	5.2
Epoxy	Experimental	2.6	0.35	1.92	82
Graphite/epoxy	Experimental	3	0.34	-	77
Graphite/epoxy	CUF	3.01	0.334	1.85	78

In the next step, GF/PDMS composites with four types of GF are investigated by the micro-thermoelastic CUF-MSG model at 300 K and 400 K. For all samples, GF has a volume fraction of 8.1%. As reported in Table 8.8, at both 300 K and

Table 8.8 The elastic properties of GF/PDMS composites by the micro-thermoelastic CUF-MSG model.

	T=300 K		T=400 K	
Composite	Young modulus (GPa)	Poisson ratio	Young modulus (GPa)	Poisson ratio
GF_1/PDMS	0.32	0.33	0.33	0.35
GF_2/PDMS	1.55	0.30	1.56	0.31
GF_3/PDMS	1.87	0.31	1.88	0.32
GF_4/PDMS	2.20	0.34	2.22	0.35

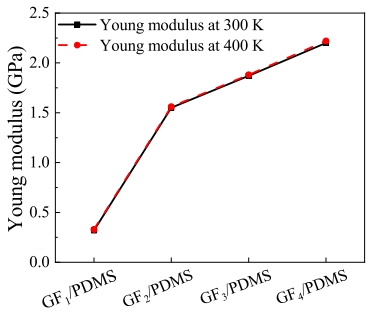

Fig. 8.16 The effective Young modulus of GF/PDMS composites at 300 K and 400 K.

400 K, the Young modulus of the composites increased as the density of the GF samples increased. Poisson ratio also increased with decreasing percentage of reinforcement's porosity. Fig 8.16 is presented for a better understanding effect of GF's Young modulus on the effective Young modulus of GF/PDMS composites. It can be seen that there is a minimal difference between the effective Young modulus at 300 K and 400 K. Because the Young modulus of GFs are assumed to be the same value at both temperatures, and the slight difference is due to the change of PDMS's Young modulus at 300 K and 400 K.

Table 8.9 The thermoelastic properties for GF/PDMS composites at 300 K.

	T=300 K		
Composite	Heat capacity (CUF) $(10^6 J/m^3.K)$	Heat capacity (rules of mixture) $(10^6 J/m^3.K)$	CTE $(10^{-6} K^{-1})$
GF_1/PDMS	1.410	1.438	210
GF_2/PDMS	1.425	1.451	35
GF_3/PDMS	1.400	1.432	30
GF_4/PDMS	1.402	1.438	26

Table 8.10 The thermoelastic properties for GF/PDMS composites at 400 K.

Composite	T=400 K		
	Heat capacity (CUF) $(10^6 J/m^3.K)$	Heat capacity (rules of mixture) $(10^6 J/m^3.K)$	CTE $(10^{-6} K^{-1})$
GF_1/PDMS	1.56	1.627	240
GF_2/PDMS	1.58	1.639	86
GF_3/PDMS	1.54	1.624	62
GF_4/PDMS	1.55	1.623	42

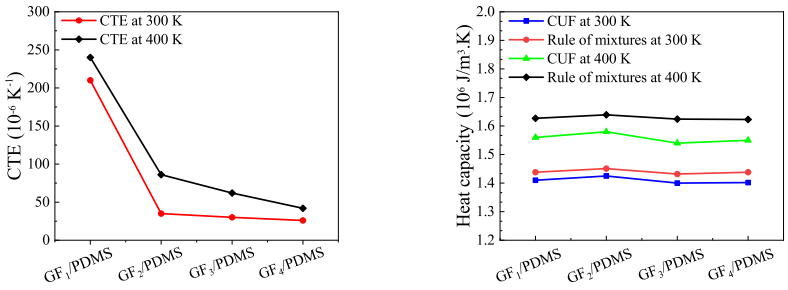

(a) (b)

Fig. 8.17 (a) The effective CTE values and, (b) The effective heat capacity quantities for GF/PDMS composite with the micro-thermoelastic CUF-MSG and rules of mixture methods at 300 and 400 K.

Likewise, Table 8.9 and 8.10 report the effective CTE and heat capacity of the GF/PDMS composites at 300 K and 400 K. Essentially, the effective CTE of composites increases with increasing porosity and temperature which signifies the effect of reinforcement's Young modulus on the effective CTE value of the composites. To put it differently, increasing the number of atoms in the simulation box in dense GF samples diminishes the space of atom motion, resulting in a drop in CTE. The effective CTE values of the GF/PDMS composites at both mentioned temperatures are also shown in Fig. 8.17(a) for further explanation. At 300 K and 400 K, the composites reinforced with the fourth type of GFs have decreased CTE by 90% and 84%, respectively, compared to the PDMS, which had the most significant reduction. GFs have high stiffness and a very low CTE, which is very promising in applications requiring high dimensional stability. This feature causes the movement limitation of polymer chains and reduces the effective CTE. Eventually, the effective CTE of the composites is validated with reference [27]. In Table, 8.9 and 8.10 and also shown in Fig. 8.17(b), the parameters of effective heat capacity calculated

by the two methods rules of mixture and the micro-thermoelastic CUF-MSG are presented at 300 K and 400 K. Alternatively, according to Eq. 5.26 in c_v, effective heat capacity consists of two terms. The first term of this relationship depends on the Young modulus, Poisson ratio, CTE, and geometry. In fact, this model concludes the effective CTE and heat capacity value by coupling the elastic and thermoelastic parameters. These effects cause the heat capacity of the GFs to have the opposite effect on the matrix and reduce the effective heat capacities in some samples. The second expression, which acts as the rules of mixture, is that the effective heat capacity value is an average value between this parameter for the matrix and the fiber. In general, it can be expressed that with growing porosity and temperature, the effective value of heat capacity expansions. It is clear that the accuracy and impact of other parameters can be seen in the micro-thermoelastic CUF-MSG method. Finally, the accuracy of these calculations is compared and confirmed with the output of the experimental measures[125].

8.2.4 Summary

In this study, the four types of GF simulated were examined in terms of CTE and specific heat relative to temperature. Calculating temperature-dependent properties improves the accuracy of the computations. A lower average dispersion in CTE was found for the last of the four GF groups with maximal density and minimal porosity. Generally, GFs' CTE increased with temperature and porosity percentage. Calculating the specific heat of GFs uncovered that increasing the temperature also increases the specific heat. By a slight change in mass density and percentage of porosity at the nanometer scale, significant changes occur in the Young modulus of GF samples, resulting in their mechanical and thermoelastic properties acting differently from each other. It was found that at 300 K and 400 K, the maximum CTE belongs to the GF reinforced composite with the highest porosity percentage, and vice versa, the composite which is reinforced with dense GF has the minimum CTE. The high specific heat of GFs makes them an excellent energy storage material. It is worth noting that the specific heat of foams on the nanoscale depends, in addition to temperature, on other parameters such as the internal energy of the simulated box, which is proposed to be considered in future works. On the other hand, the effective heat capacity of composite depends not only on the heat capacity but also on the Young modulus, CTE, and geometry of its components. Furthermore, It was

found that GFs with the highest porosity have the most significant specific surface area. The specific surface area decreases with decreasing porosity percentage. It is predicted that GF with random porosity and high specific surface area has the advantages such as fast ion diffusion rate and high electrochemical performance. For this reason, future work will be related to the computation of the electrochemical properties of these materials.

8.3 Results and Discussion for Thermal Conductivity

Thermal management is a crucial design matter in the fields of electronics, optoelectronics, and electric vehicles. The development in the miniaturization of electronic devices increases the hot area temperature, which creates the need for the fabrication and development of materials with high thermal conductivity (TC) [126, 127]. Lack of thermal management may lead to sudden or localized growth in hot areas, which not only significantly shortens the life of the device but also leads to dangerous operating conditions. Over the past decade, 2D graphenes have attracted the attention of researchers for thermal management applications of electronic devices owing to their high TC and unique properties [128]. Due to its electronic structure, graphene has a calculated TC of up to 10 KW m^{-1} K^{-1} [129]. On the other hand, polymer materials play an essential role in thermal and electronic applications thanks to their low price and high mechanical properties. For this reason, it is necessary to achieve polymer composites with higher thermal performance. Polydimethylsiloxane (PDMS) is a suitable matrix for thermal applications because of its compressibility, flexibility, and intense interaction with graphene [130]. In addition, PDMS provides a wide variety of applications due to its outstanding properties, such as low glass transition temperature, flexibility, chemical inertia, and a wide range of physical states. Initially, cheap graphite flakes and expanded graphite were used as reinforcement to improve the TC of polymer-based composites. After that, single-layer and multi-layer graphene were introduced as fillers with high TC. W. Yu et al. [131] achieved a 3000% increase in effective TC for multi-layered graphene-filled epoxy composites at a loading of $\sim 25 vol\%$. Lim and Choi [132] express that the TC of polymer nanocomposites filled with two different graphenes and boron nitride is in the range of 6.2-9.5 W m^{-1} K^{-1}. However, 2D graphene sheets have agglomeration problems when used as fillers. A possible solution is to connect two-dimensional

graphene nanosheets and convert them into a three-dimensional network to prevent aggregation. Graphene foam (GF) is one of the carbon foam structures that consist of several nanosheets of graphene and a large number of pores in its connection structure [133]. GF is used in various applications due to its properties, such as adsorbents [83], electrochemical energy storage [134], sensors [130], phase change materials [135], and polymer nanocomposites. Petts et al. [136] found that at a low volume fraction (0.45 ± 0.09) and room temperature, the TC of GFs, consisting of few-layer graphene and ultrathin graphite synthesized via chemical vapor deposition, increased from 0.26 to 1.7 W m^{-1} K^{-1} by changing the etchants. Lin et al. [135] investigated a significant reduction in GF's TC as a consequence of structural defects. They studied the thermal diffusivity of GF using the transient electro-heat method. Later, Jia et al. [112] produced GF/epoxy nanocomposites using the chemical vapor deposition method. They found in experiments that three-dimensional GF grids act as fast carriers for load transfer, and for this purpose, they investigated the electrical conductivity, strength, and flexural modulus. Furthermore, Li et al. [137] demonstrated that GFs have thermal properties that increase with a temperature above room temperature. In their study, the temperature dependence of the thermal properties of GF has been investigated using the transient electro-thermal method. As a result, a significant increase in TC and thermal diffusivity has been observed for GF. Zhang et al. [42] analyzed the thermal behavior of a polymer composite filled with GF using the finite element method. Due to the interconnected structure of GF, which forms effective thermal pathways, the polymer composite reinforced with GF has good thermal properties. They also studied the effect of geometry in GF on the TC of the composite. Sadr and Vahedi [138] employed a multiscale method using molecular dynamics and finite element method to calculate the TC of graphene hexagon-boron nitride structures. Based on the results obtained from the atomic scale, they developed a finite element model for the larger-grained material to calculate the heat conduction effect of the macroscopic sample. Finally, Menci and Kirka [139] investigated the thermal properties of a hybrid nanostructure composed of GFs with covalent bonding. The analysis considered fullerene's presence and absence by performing reverse non-equilibrium molecular dynamics simulations. The simulation results indicate that the proposed nanostructure offers significant TC performance with isotropic thermal performance. The use of molecular dynamics methods is an attractive way to compute the properties of this type of material due to the complete representation of all interatomic interactions. However, the performance of GFs has

yet to be significantly recognized for competition as a porous carbon material for large-scale use in energy storage devices. On the other hand, calculating the properties of GFs in nano-dimensions can only be compared with the nano-dimensions model. Then, multiscale simulations should be involved to compare them at the macroscopic level. Nevertheless, calculating the thermal properties of nanoscale GFs and PDMS matrices and pairing these results with macroscopic methods can lead to good thermal properties. In this study, the TC of PDMS nanocomposites reinforced with GF has been investigated. The effects of volume fraction, density, and porosity percentage of GF and the length of PDMS chains on the effective TC of GF/PDMS nanocomposites have been investigated by using the concept of repeating unit cells. The RUC is considered a distribution according to SEM images. This model shows more realistic results than the representative volume element with one particle. The estimations of the reinforcing part (GF) and the matrix (PDMS) are performed by molecular dynamics. The interatomic forces between carbon atoms in GF are computed by the Airebo and Tersoff potential. Also, all interatomic forces in the PDMS polymer are calculated by the Charmm force field [140], a force field that provides an accurate representation of the bonding and non-bonding interactions for the material and has previously been used for PDMS in some applications [141]. The non-bonding interactions between PDMS atoms are modeled with the Lennard-Jones (LJ) potential, and a cutoff of 10 is defined with all combined pair interactions for Si, O, H, sp^2 C, and sp^3 C. The equilibrium distance and depth of the potential energy well were calculated using the Lorentz-Berthelot mixing rules. After calculating the effective TC, next, the obtained results are compared with the experimental results.

8.3.1 TC of graphene foam

After the equilibration step, the sample's temperature gradient is created by exchanging kinetic energy between hot and cold zones. The energy exchange is achieved by subtracting some energy from the hot zone while adding the same energy to the cold zone. Since the system's total linear momentum and energy are constantly maintained, an opposite physical heat flow is artificially generated from the cold layers to the hot layers. Figure 8.19 show the energy subtracted from the hot zone is equal to the energy added to the cold zone for three directions and increases linearly with time, indicating that the heat exchange has been properly established in the system. Figure 8.18 shows the temperature changes in different coordinates of the simulated

box length in the direction of x, y, and z, respectively. The heat flux applied to the NVE ensemble can be calculated based on the gradient of energy changes in the system over time. In addition, a study of the temperature profiles after the recorded energy exchange shows that the temperature changes almost linearly in areas except for the neighborhood of cold and hot areas. As can be seen, it can be expressed that the energy changes versus time and the length changes with temperature are equal for all three directions. It should be noted that these diagrams are for the first group of GF, which is computed in the same way for all samples.

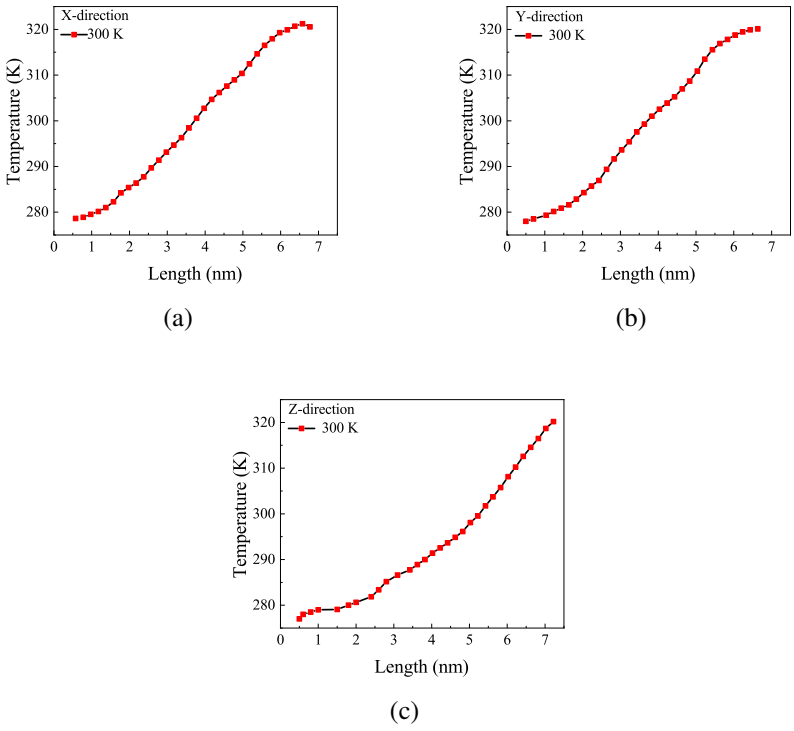

Fig. 8.18 Diagram of temperature profile variation with length in (a) x-direction, (b) y-direction, and (c) z-direction.

8.3.2 TC of PDMS

This study has tried using the non-equilibrium molecular dynamics (NEMD) method to calculate the TC of PDMS polymers at 300 K using LAMMPS software. An amorphous PDMS structure with different chain units is created using Moltemplate. The first group of PDMS's structure box is created of 6120 atoms and density

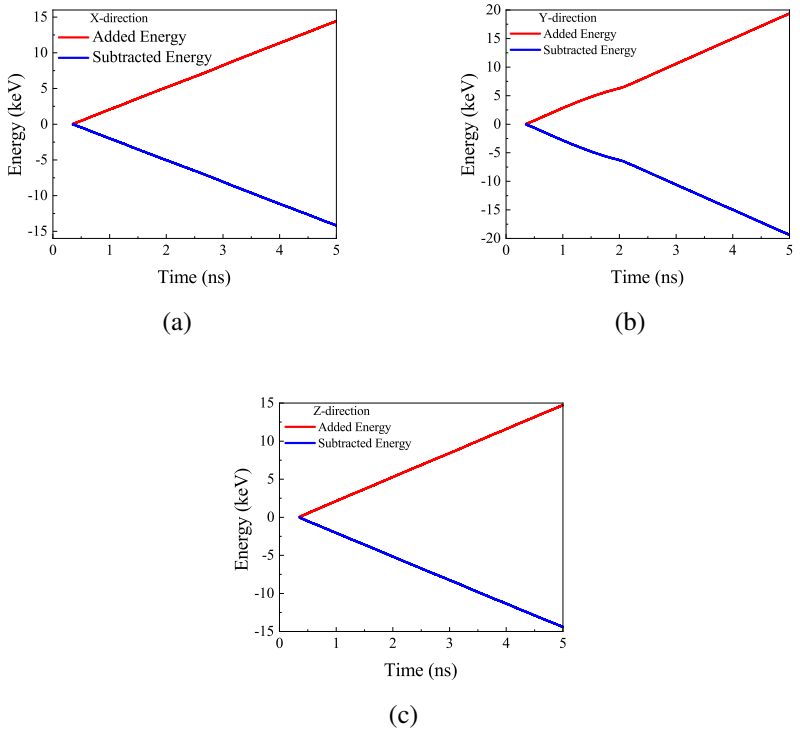

Fig. 8.19 Energy profiles added to the cold zone and subtracted from the hot zone in (a) x-direction, (b) y-direction, and (c) z-direction.

0.97 ± 0.05 g/cm^3. The cross-sectional area of PDMS is approximately 60×60 Å^3. This method calculates TC by defining the hot and cold zones and adding and subtracting energy from these two regions. The diagram of change energy against temperature is shown in Fig. 8.20(a). The amount of energy added to the cold area equals the amount of energy subtracted from the hot zone. Also, the graph of temperature changes in different coordinates for PDMS is shown in Fig. 8.20(b). It should be mentioned that this diagram is equal in three directions. The volume of the polymer simulation box is equal to 216×10^{-24} Å^3. After the annealing operation, the total energy and temperature of the PDMS simulated box are presented in Fig. 8.21(a), demonstrating the system achieves a suitable structure. It worth be noted that these diagrams are for the first sample of PDMS with chains of 50 -Si-(CH_3)2-O- units, and the same is calculated for the 55 and 60 units samples. Fig. 8.21(b) shows the simulation box of the PDMS structure, which is heat flows along the x-axis from the hot region (320 K) to the cold region (280 K). Red areas indicate high

temperatures, and blue areas indicate low temperatures. To confirm the accuracy of the results obtained with the results in the literature validated [141].

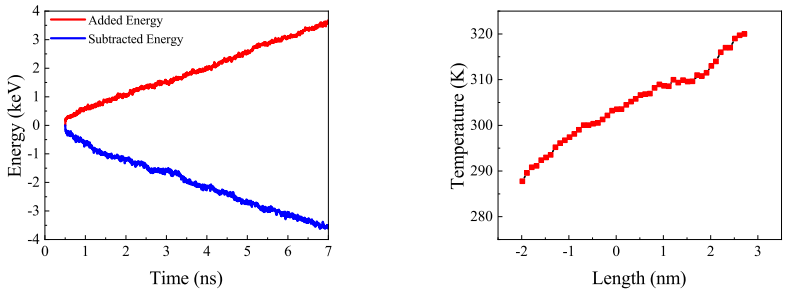

(a) (b)

Fig. 8.20 (a) Energy profiles added to the cold zone and subtracted from the hot zone, (b) Temperature profile variation with length.

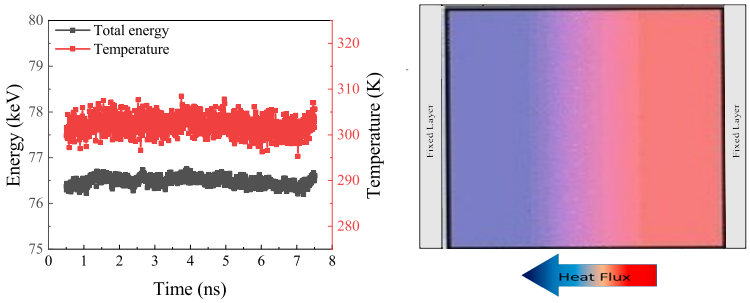

(a) (b)

Fig. 8.21 (a) The energy and temperature of the simulated PDMS box, and (b) The schematic temperature profile in NEMD method.

8.3.3 TC Result

Efforts to combine GF fibers with polymeric materials such as PDMS, which are thermal insulators, are increasing due to the high thermal efficiency of composite materials as a result of the immense heat transfer path created by the carbon joints in the foam. In this study, the TC of PDMS nanocomposites reinforced with GF has been investigated. In addition, the effects of volume ratio, density, and porosity percentage of GF and the length of PDMS chains on the effective TC of PDMS/GF nanocomposites have been investigated using the CUF-MSG. For the CUF-MSG

micromechanical analysis, the fiber and matrix distribution taken to the SEM images are modeled and represented as RUC. Fig. 5.4(a) and 5.4(b) show how the RUC model is built starting from the SEM image in which the distribution of the fiber and the matrix over the volume can be approximated with a particular geometry. The MD platform accomplishes computations of the reinforcing part (GF) and the matrix (PDMS). Since GF/PDMS also have a low thermal surface resistance of 0.04 cm^2K/W, which is one time smaller than conventional thermal paste and grease [142], in the present study, the bond between GF and PDMS is considered a perfect interface. After computing the effective TC, the results are compared with those in the references. The TC values for GF and PDMS with the mentioned conditions have been calculated by considering the temperature of the hot and cold zone at 320 K and 280 K, respectively. Using the NEMD method, the TC values are calculated for all groups of GF and PDMS. For this purpose, GF simulation uses the two potentials of Airebo and Tersoff. TC values for all groups of GF K_{GF} considering two different potentials are presented in Table 8.11. The values of TC of compressed solid sheets of graphene K_G, which are the constituents of GFs, are also shown in Table 8.11. Definitely, these values are much higher for solid graphene sheets than GFs because the effects of folding, defects, and pores are not present in compressed solid graphene samples, which have been verified with [136].

Table 8.11 TC of GFs simulated by Airebo and Tersoff potential and solid TC of graphene sheet-based GF at 300 K.

Foam types	K_{GF} [W/mK] Airebo	K_{GF} [W/mK] Tersoff	K_G [W/mK]
GF_1	0.76	0.84	520
GF_2	0.91	0.97	622
GF_3	1.14	1.19	775
GF_4	1.21	1.34	818

It was noted that two main factors affect the TC of GFs: the number of foam connections and the presence of defects. In fact, the groups of GF in this study with different connectivity (see Fig. 8.12) and various numbers of defects show different values of TC (TC per unit mass density). Several reasons can account for this, but in the present study, it is discovered that smaller pore size generally means higher density, as reported in Table 8.3, which indicates higher TC linked to the high number of connections. In contrast, in graphene with a lower density, the

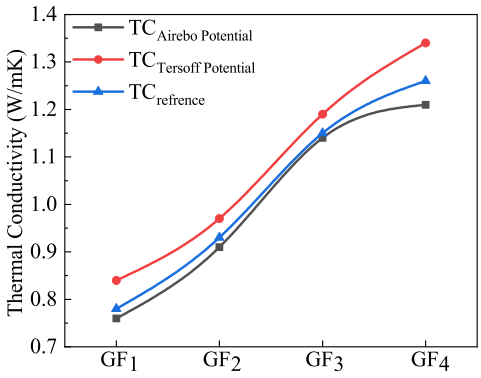

Fig. 8.22 Comparison of TC calculated using the NEMD method with Tersoff and Airebo potentials in this research with reference [6].

size of the pores is more significant, and the number of three-coordinated carbon atoms is lower; this aspect reduces the TC's value. It should be noted that GF, due to its particular topology, has a very high TC, so it is clear that the high level of three-coordinated carbon is connected to the large TC. Conversely, the presence of more defects in high-density foams with few pores should reduce TC. Therefore, the mass density (or pore size) and the number of defects in determining the TC almost cover each other. Precisely, in Fig. 8.22, the TC is plotted as a function of mass density for four different foam groups at 300 K as the reference, which increases the TC with the increase in density. The high simulated TC value of GF depends on the high specific surface area of graphene in the form of foam. Also, this material's network structure creates an excellent TC while being lightweight and low-density and causing good heat transfer. The contacts of the graphene sheets in the foam act as bridges for TC and improve the TC of GF, as shown in Fig. 8.2. The effect of CTE at high temperatures makes the very porous structure much more substantial and is responsible for reducing the resistance to thermal contact [143]. On the other hand, in the present numerical conditions, an attempt has been made to use the most consistent potential with the experimental conditions. After using different values of potentials, it was concluded that two potentials, Airebo and Tersoff, have the best compatibility with carbon atoms. Regarding the precision of potential calculations, Airebo is more reasonable, and the results are closer to the outcomes of experimental works [6, 137], but the calculation volume is expanded.

Table 8.12 TC of PDMS polymer matrix groups at 300 K.

PDMS chain units	Number of atoms	TC [W/m·K]	Standard deviation [W/m·K]
$PDMS_{50}$	102	0.19	0.011
$PDMS_{55}$	112	0.22	0.018
$PDMS_{60}$	122	0.24	0.015

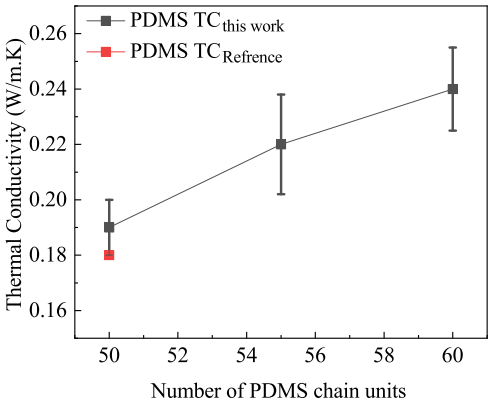

Fig. 8.23 Comparison of TC of PDMS versus the number of chain units with reference [7].

In real synthesis, PDMS polymers are mixed with chains of different unit lengths, so studying the effect of the chain unit lengths on the TC significantly impacts comprehending the polymers' heat conduction. Here, PDMS with various chain units is used to calculate the TC between its chains in three directions. The length of the simulation box is considered equal in three directions. According to references [141], the hot and cold regions should be specified at both ends of the box so that the heat flux can transmit between the two parts. Moreover, a particular fixed layer is kept at both ends of the two regions to keep the heat flux unobstructed. Table 8.12 reported the TC values of PDMS with different chain units, the number of atoms, and the standard deviation for each PDMS chain. Fig. 8.23 shows the change in the TC of PDMS versus the number of polymer chain units in detail, which is compared and confirmed with reference [7] in the number of 50 chain units. Generally, the TC increases with the expansion of the chain units, which is the same change trend of PDMS reported in reference [141]. Therefore, more extended chain units are beneficial for PDMS TC.

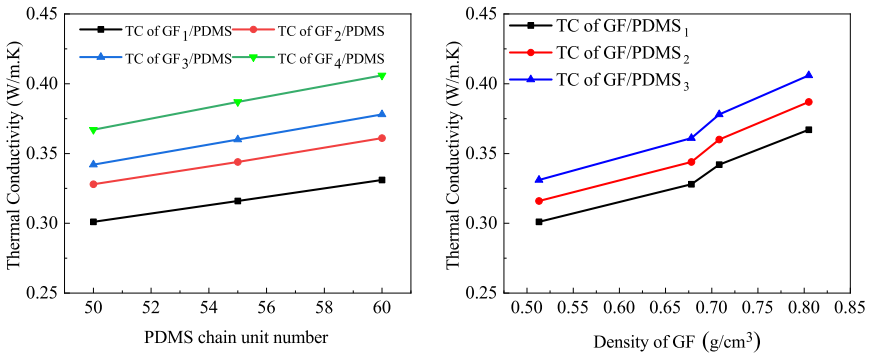

Fig. 8.24 (a) Effective TC of GF/PDMS versus the number of chain units of PDMS, and (b) Versus the density of GF for Tersoff potential.

The effective TC values of PDMS composites reinforced with 14 vol% GF simulated by Airebo and Tersoff potentials are presented below graphs. Fig. 8.24(a) and 8.24(b) show the effective TC of GF/PDMS composites versus the number of chain units of PDMS, and the density of GF for Tersoff potential, respectively. As can be seen, the effective TC of the composite is calculated using the CUF-MSG method. According to Fig 8.24(a), the value of effective TC improves with the extension of polymer chain units. By increasing the length of the polymer chains, the heat transfer from the matrix to the polymer and vice versa is accomplished more efficiently. Increasing the density of GF as reinforcement has also caused an addition in the effective TC of the composite, which is shown in Fig. 8.24(b). Due to the continuous network structure of GFs, with increasing mass density and decreasing porosity, TC is enhanced; this is also improved by expanding the polymer chain units. It should be noted that the synergistic effect enriches GF composites due to the three-dimensional structure and less accumulation. The same trend is also confirmed for GF simulated with Tersoff potential based on PDMS composites. The only difference is that GFs simulated with Tersoff potential show higher TC; as a result, the effective TC is also increased as depicted in Fig. 8.25(a) and 8.25(b). Since GF also has a low interfacial thermal resistance of about $10^{-6\sim-9}\ Km^2/W$ [142, 110], in this study, the bond between GF and PDMS is considered complete and perfect.

According to the literature, [110], the TC of PDMS-based composite reinforced by GF with a density between 0.5 and 0.9 g/cm^3 presents a value between 0.26 and 0.55 W/mK. In addition, the gradual expansion in the gap between GF/PDMS and

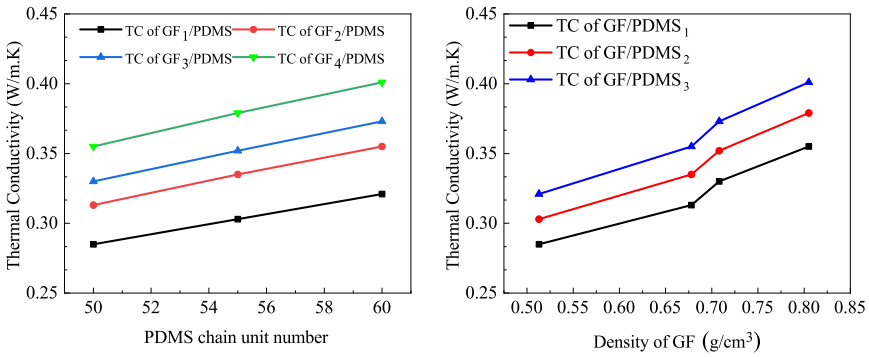

(a) (b)

Fig. 8.25 (a) Effective TC of GF/PDMS computed with the CUF-MSG method versus the number of chain units of PDMS and (b) Versus the density of GF for Airebo potential.

graphene sheet/PDMS composites reveals an increase in the synergistic effect of GF in GF/PDMS composites. Zhao et al. [90] obtained a TC of 0.58 W/mK for a GF composite with 10 wt% of fiber volume fraction, which is about 27% higher than that of pure PDMS (the TC of pure PDMS is 0.455 W/mK in their work). Zhao et al. [144] acquired a TC of 0.41 W/mK for 15 vol% of GF to GF/PDMS composite. In the present work, quantitative characterization of the synergistic effect between GF can be supplied using 14% of fiber volume fraction in GF/PDMS composite. Compared to pure PDMS, the increase in TC of GF/PDMS, by 0.406 W/mK, is 1.691 times bigger than PDMS's TC, which shows a noticeable improvement. Table 8.13 presents a comparison between the effective TC of some references and its validation with the micromechanical method used in this research. This table includes the type of composite, TC of composites, and TC of composites per TC of PDMS matrix, as well as the amount of GF loading. According to the data in the table, it can be expressed that the accuracy of the used method is confirmed with a difference of 1.2%. This table first validates the micromechanical model used in this work. Then it shows the maximum increase in the effective TC of the GF/PDMS composites. This advantage is attributed to the high continuous between GF struts and the large specific area between the fillers and the polymer matrix, enabling effective TC development. By comparing the values presented in Table 8.13 with those reported in [145], it can be seen that by adding the same amount of filler to the polymer base composite in this work, the effective TC of the composite compared to the pure PDMS has increased by 1.691 times. This value shows the correct selection of the unit cell and GF's synergistic effect on the polymer matrix's TC. Based on the SEM images, it can

Table 8.13 TC of GF/polymer composites in comparison with experimental outputs from references.

Composite	loading vol%	TC of Composite [W/mK]	TC of Composite/TC of PDMS [-]	Reference
GF/PDMS	8	0.940	3.350	[42]
GF/PDMS	8	0.938	3.310	CUF-MSG
GF/PDMS	14	0.406	1.691	CUF-MSG
GF/PDMS	14	0.402	1.675	CUF-MSG
GF/PDMS	14	0.388	1.616	CUF-MSG
GF/PDMS	15	0.410	1.708	[144]
GF/PDMS	18	0.364	1.915	[146]
GF/PDMS	18	0.361	1.900	CUF-MSG

be seen that the graphene arms in GF are entirely connected, and a network structure is formed. By injecting the matrix into the GF, in reality, the space between the graphenes is filled, and the space inside the struts is filled with polymer, which shows the uniform structure of the GF/polymer composites compared to the composites containing graphene sheets. This interconnected and uniform space increases the effective thermal properties of these composites.

8.3.4 Summary

This work uses a multi-scale model based on CUF-MSG formulation to simulate the heat transfer behavior of GF composites filled with polydimethylsiloxane (PDMS). GF geometry and volume fraction are taken into account when simulating heat transfer. Due to the minor thermal resistance between GF and PDMS, the effect of it on the TC of the composite has been neglected. In this study, the TC of three types of PDMS-matrix and four groups of GF has been investigated. The TC of the PDMS-matrix increased with the increasing number of chain units. Also, by reducing the percentage of porosity, GF's TC has improved significantly. Then, employing the CUF-MSG micromechanics method, the effective TC of the composites obtained from GF and PDMS has been calculated. The effective TC of the composite is increased by expanding the chains of the polymer matrix and decreasing the porosity of the three-dimensional network of GF. The volume percentage of reinforcement in the composite can be directly controlled by the density of GF. In GFs, due to lack of agglomeration, the TC increases with increasing volume fraction. In

contrast, in individual graphene composites, the accumulation phenomenon occurs with increasing volume percentage, and the effective TC decreases. The effect of different potentials and the similarity of their results with experimental works are also investigated. It should be mentioned that although the simulated GFs with Tersoff potential have shown higher TC, the accuracy of Airebo potential is more elevated in considering all interatomic interactions in carbon atoms. So, Airebo's potential is preferred. On the other hand, however, GF has a continuous structure; it has not shown significant TC, which can be due to the pores or the presence of unconventional defects created in their structures. The thermal properties of GFs can be improved by increasing another reinforcing material, such as carbon black, with higher TC, which is suggested to be considered in future works. Which also increases the effectiveness of GFs.

8.4 Conclusion and Future Works

8.4.1 Conclusion

In the present work, GF samples were synthesized using a highly efficient and cost-effective method with various drying percentages. The foam structure was guaranteed using the Raman spectroscopy technique and SEM images. The density of the synthesized samples was inversely related to their drying percentage, and the lowest mass density belonged to the sample that was 100% dried. By comparing the results of the tensile test for GF/polymer composites with different mass densities of GFs, it was found that the composite reinforced with 100% dried GF samples has a maximum Young modulus. By raising the drying percentage and decreasing liquid volume in GFs, the resulting composite has a higher Young modulus. Also, as a significant result, the composites that contain wet GFs have less tensile strength, but their strain percentage is higher than fully dried GFs. The highest Young modulus and tensile strength of the composite include 100% dried GF with 0.5 wt%, which increased by 138% and 48% compared to neat polymer, respectively. A tensile test was conducted in this study to determine the Young modulus of neat polymer and its validity was assessed by its standard. It can also be concluded that the liquid in 90-GF and 95-GF samples act as a barrier to matrix transfer in all parts of the foam and do not increase the mechanical properties compared to 100-GF/epoxy

composites. By adding GF to the polymer composite, the Young modulus can be increased from twofold to threefold by control of the fabrication method and synthesis of reinforcement. Furthermore, in this work, the brittleness of the composite can be controlled by the drying percentage of GF samples. Moreover, by simulating the structure of GF in the LAMMPS software, the different types of GF were examined in terms of Young modulus, CTE, specific heat, and TC relative to temperature. In particular, the one simulated GF was confirmed in density, the number of carbon-carbon bonds, and RDF diagrams with the experimental sample. It should be noted that the GF simulation added no chemical functional groups to the graphene structure. GF isotropic behavior was proved after simulating the tensile test at different strain rates. The Young modulus calculated by the CUF-MSG micromechanical numerical model has a difference close to 1.5% with the experimental Young modulus, which is acceptable and validates the utilized numerical method. On the other hand, calculating temperature-dependent properties improves the accuracy of the computations. Generally, GFs' CTE increased with temperature and porosity percentage. Calculating the specific heat of GFs uncovered that increasing the temperature also increases the specific heat. A lower average dispersion in CTE was found for the last of the four GF groups with maximal density and minimal porosity. By a slight change in mass density and percentage of porosity at the nanometer scale, significant changes occur in the Young modulus of GF samples, resulting in their mechanical and thermoelastic properties acting differently from each other. It was found that at 300 K and 400 K, the maximum CTE belongs to the GF-reinforced composite with the highest porosity percentage, and vice versa, the composite which is reinforced with dense GF has the minimum CTE. The high specific heat of GFs makes them an excellent energy storage material. It is worth noting that the specific heat of foams on the nanoscale depends, in addition to temperature, on other parameters, such as the internal energy of the simulated box. On the other hand, the effective heat capacity of the composite depends not only on the heat capacity but also on the Young modulus, CTE, and geometry of its components. It was found that GFs with the highest porosity has the most significant specific surface area. The specific surface area decreases with decreasing porosity percentage. Moreover, the Poisson ratio of the GF/polymer composite was also calculated numerically, a value used to evaluate the transverse response of the composite to deformation. Nevertheless, GF, in addition to preventing the accumulation of graphene sheets in polymer composites, has a high mechanical performance as polymeric reinforcements for structural appli-

cations that require low weight as well as high tensile strength and Young modulus. Because of the remarkable properties of GFs and polymer composites reinforced with these foams, their thermal properties of them to be studied in this research. This study investigates the TC of three types of PDMS-matrix and four groups of GF. The TC of the PDMS-matrix increased with the increasing number of chain units. Also, by reducing the percentage of porosity, GF's TC has improved significantly. GF geometry and volume fraction are taken into account when simulating heat transfer. Then, employing the CUF-MSG micromechanics method, the effective TC of the composites obtained from GF and PDMS has been calculated. Due to the minor thermal resistance between GF and PDMS, the effect of it on the TC of the composite has been neglected. The effective TC of the composite is increased by expanding the chains of the polymer matrix and decreasing the porosity of the three-dimensional network of GF. The density of GF can directly control the volume percentage of reinforcement in the composite. In GFs, due to lack of agglomeration, the TC increases with increasing volume fraction. In contrast, in individual graphene composites, the accumulation phenomenon occurs with increasing volume percentage, and the effective TC decreases. The effect of different potentials and the similarity of their results with experimental works are also investigated. It should be mentioned that although the simulated GFs with Tersoff potential have shown higher TC, the accuracy of Airebo potential is more elevated in considering all interatomic interactions in carbon atoms. So, Airebo's potential is preferred. The TC values are similar to those of glass (1 W/mK) for lower-density foams, with a slight increase of TC up to 1:5 W/mK for higher-density foams. Finally, it was proved that the CUF-MSG micromechanical model used in this study is very efficient and accurate for calculating the composite's elastic and thermal properties using their constituents' properties.

8.4.2 Future Works

In this study, the multi-step molecular dynamics method has been done continuously to calculate the properties of GF/ polymer composites. First, the GF structure was synthesized in the laboratory, and then the GF/polymer composite was produced to perform the tensile test. Using image processing methods, the structure of GF has been produced in molecular dynamics with a new method. Employing a cross-platform text-based molecule builder for LAMMPS called Moltemplate software,

the structure of polymer chains with different chain lengths has been simulated. After creating the GF structure and obtaining the elastic and thermal properties, we utilized the multi-scale methods to calculate these properties on a macro scale. In this study, a high-precision MSG-CUF micromechanical method was used to compute the effective properties of the composite by the properties of its components. Finally, the results of numerical calculations have been compared with the experimental results, and the accuracy of the employed model has been confirmed. According to the activities carried out, some suggestions for future work are provided. The results obtained from Fig. 8.9 showed that the behavior of GF samples after failure was different in each direction, which is suggested the failure of GF materials to be investigated in future research. Considering the extremely high TC of GFs, it is suggested to study the electrical conductivity of this type of composite. Adding some functional groups on graphene sheets is suggested to prevent folding in GF to increase their thermal properties. Calculating interface thermal resistance in GF and polymer can increase the knowledge of the basic parameters affecting the effective TC of the composite. Adding an insignificant volume percentage of some materials, such as carbon black, can also increase the effective TC of the composite, which is suggested to be investigated in the case of GFs.

References

[1] Vladimir Pokropivny, Rynno Lohmus, Irina Hussainova, Alex Pokropivny, and Sergey Vlassov. *Introduction to nanomaterials and nanotechnology*, volume 1. Tartu University Press Ukraine, 2007.

[2] Tokio Yamabe and Kenichi Fukui. *The science and technology of carbon nanotubes*. Elsevier, 1999.

[3] G Maitland, M Rigby, E Smith, W Wakeham, and Douglas Henderson. Intermolecular forces: their origin and determination. *Physics Today*, 36(4):57, 1983.

[4] Erasmo Carrera, Maria Cinefra, Marco Petrolo, and Enrico Zappino. *Finite element analysis of structures through unified formulation*. John Wiley & Sons, 2014.

[5] Sajedeh Khosravani, Mohammad Homayoune Sadr, Erasmo Carrera, and Alfonso Pagani. Synthesis, experimental testing and multi-scale modelling of graphene foam/epoxy composite. *Mechanics of Advanced Materials and Structures*, pages 1–10, 2022.

[6] Andrea Pedrielli, Simone Taioli, Giovanni Garberoglio, and Nicola Maria Pugno. Mechanical and thermal properties of graphene random nanofoams via molecular dynamics simulations. *Carbon*, 132:766–775, 2018.

[7] Alessandro Di Pierro, Bohayra Mortazavi, Hamidreza Noori, Timon Rabczuk, and Alberto Fina. A multiscale investigation on the thermal transport in polydimethylsiloxane nanocomposites: Graphene vs. borophene. *Nanomaterials*, 11(5):1252, 2021.

[8] Shiren Wang, Madhava Tambraparni, Jingjing Qiu, John Tipton, and Derrick Dean. Thermal expansion of graphene composites. *Macromolecules*, 42(14):5251–5255, 2009.

[9] MC Roco, RS Williams, and AP Alivisatos. Nanotechnology research directions, national science & technology council report, 2000.

[10] Richard W Siegel and Evelyn Hu. *Nanostructure science and technology: R & D status and trends in nanoparticles, nanostructured materials and nanodevices*. Springer Science & Business Media, 1999.

[11] Alan S Edelstein and RC Cammaratra. *Nanomaterials: synthesis, properties and applications*. CRC press, 1998.

[12] Michael J O'connell. *Carbon nanotubes: properties and applications*. CRC press, 2018.

[13] Yury Gogotsi and Volker Presser. *Carbon nanomaterials*. CRC press, 2006.

[14] Javad Jeddi, Ali Asghar Katbab, and Mahsa Mehranvari. Investigation of microstructure, electrical behavior, and emi shielding effectiveness of silicone rubber/carbon black/nanographite hybrid composites. *Polymer Composites*, 40(10):4056–4066, 2019.

[15] Matthew J Allen, Vincent C Tung, and Richard B Kaner. Honeycomb carbon: a review of graphene. *Chemical reviews*, 110(1):132–145, 2010.

[16] Owen C Compton, Bonny Jain, Dmitriy A Dikin, Ali Abouimrane, Khalil Amine, and SonBinh T Nguyen. Chemically active reduced graphene oxide with tunable c/o ratios. *ACS nano*, 5(6):4380–4391, 2011.

[17] Simone Quaranta, Mauro Giorcelli, and Patrizia Savi. Graphene and mwcnt thick films: preparation and rf electrical properties study. 2020.

[18] Bhaskar Garg, Tanuja Bisht, and Yong-Chien Ling. Graphene-based nanomaterials as heterogeneous acid catalysts: a comprehensive perspective. *Molecules*, 19(9):14582–14614, 2014.

[19] Chris Binns. *Introduction to nanoscience and nanotechnology*. John Wiley & Sons, 2021.

[20] Gabor L Hornyak, Harry F Tibbals, Joydeep Dutta, and John J Moore. *Introduction to nanoscience and nanotechnology*. CRC press, 2008.

[21] Sumio Iijima. Helical microtubules of graphitic carbon. *nature*, 354(6348):56–58, 1991.

[22] Chun Li and Gaoquan Shi. Three-dimensional graphene architectures. *Nanoscale*, 4(18):5549–5563, 2012.

[23] Pingan Song, Zhenhu Cao, Yuanzheng Cai, Liping Zhao, Zhengping Fang, and Shenyuan Fu. Fabrication of exfoliated graphene-based polypropylene nanocomposites with enhanced mechanical and thermal properties. *Polymer*, 52(18):4001–4010, 2011.

[24] Alireza Chogani, Ali Moosavi, Amirhossein Bagheri Sarvestani, and Maryam Shariat. The effect of chemical functional groups and salt concentration on performance of single-layer graphene membrane in water desalination process: A molecular dynamics simulation study. *Journal of Molecular Liquids*, 301:112478, 2020.

[25] Jun Yan, Tong Wei, Bo Shao, Zhuangjun Fan, Weizhong Qian, Milin Zhang, and Fei Wei. Preparation of a graphene nanosheet/polyaniline composite with high specific capacitance. *Carbon*, 48(2):487–493, 2010.

[26] Siaw Fui Kiew, Lik Voon Kiew, Hong Boon Lee, Toyoko Imae, and Lip Yong Chung. Assessing biocompatibility of graphene oxide-based nanocarriers: A review. *Journal of Controlled Release*, 226:217–228, 2016.

[27] Yun-Hong Zhao, Zhen-Kun Wu, and Shu-Lin Bai. Study on thermal properties of graphene foam/graphene sheets filled polymer composites. *Composites Part A: Applied Science and Manufacturing*, 72:200–206, 2015.

[28] Michio Inagaki, Jieshan Qiu, and Quangui Guo. Carbon foam: Preparation and application. *Carbon*, 87:128–152, 2015.

[29] Qingyu Peng, Yibin Li, Xiaodong He, Xuchun Gui, Yuanyuan Shang, Chunhui Wang, Chao Wang, Wenqi Zhao, Shanyi Du, Enzheng Shi, et al. Graphene nanoribbon aerogels unzipped from carbon nanotube sponges. *Advanced Materials*, 26(20):3241–3247, 2014.

[30] Pierre Trinsoutrot, Hugues Vergnes, and Brigitte Caussat. Three dimensional graphene synthesis on nickel foam by chemical vapor deposition from ethylene. *Materials Science and Engineering: B*, 179:12–16, 2014.

[31] Zhihong Tang, Shuling Shen, Jing Zhuang, and Xun Wang. Noble-metal-promoted three-dimensional macroassembly of single-layered graphene oxide. *Angewandte Chemie*, 122(27):4707–4711, 2010.

[32] Sungjin Park and Rodney S Ruoff. Chemical methods for the production of graphenes. *Nature nanotechnology*, 4(4):217–224, 2009.

[33] Alexandr V Talyzin, Ilya V Anoshkin, Arkady V Krasheninnikov, Risto M Nieminen, Albert G Nasibulin, Hua Jiang, and Esko I Kauppinen. Synthesis of graphene nanoribbons encapsulated in single-walled carbon nanotubes. *Nano letters*, 11(10):4352–4356, 2011.

[34] Bo Han, Hongyun Chen, Te Hu, Huijian Ye, and Lixin Xu. High electrical conductivity in polydimethylsiloxane composite with tailored graphene foam architecture. *Journal of Molecular Structure*, 1203:127416, 2020.

[35] Suyoung Yu, Seunghwa Yang, and Maenghyo Cho. Multi-scale modeling of cross-linked epoxy nanocomposites. *Polymer*, 50(3):945–952, 2009.

[36] Jian-Ping Cao, Xiaodong Zhao, Jun Zhao, Jun-Wei Zha, Guo-Hua Hu, and Zhi-Min Dang. Improved thermal conductivity and flame retardancy in polystyrene/poly (vinylidene fluoride) blends by controlling selective localization and surface modification of sic nanoparticles. *ACS applied materials & interfaces*, 5(15):6915–6924, 2013.

[37] JC Maxwell Garnett. Xii. colours in metal glasses and in metallic films. *Philosophical Transactions of the Royal Society of London. Series A, Containing Papers of a Mathematical or Physical Character*, 203(359-371):385–420, 1904.

[38] Hugo Fricke. The maxwell-wagner dispersion in a suspension of ellipsoids. *The Journal of Physical Chemistry*, 57(9):934–937, 1953.

[39] DPH Hasselman and Lloyd F Johnson. Effective thermal conductivity of composites with interfacial thermal barrier resistance. *Journal of composite materials*, 21(6):508–515, 1987.

[40] AG Every, Yl Tzou, DPH Hasselman, and R Raj. The effect of particle size on the thermal conductivity of zns/diamond composites. *Acta metallurgica et materialia*, 40(1):123–129, 1992.

[41] Chunyu Li and Tsu-Wei Chou. Multiscale modeling of compressive behavior of carbon nanotube/polymer composites. *Composites science and technology*, 66(14):2409–2414, 2006.

[42] Ya-Fei Zhang, Yun-Hong Zhao, Shu-Lin Bai, and Xiaowen Yuan. Numerical simulation of thermal conductivity of graphene filled polymer composites. *Composites Part B: Engineering*, 106:324–331, 2016.

[43] XL Chen and YJ Liu. Square representative volume elements for evaluating the effective material properties of carbon nanotube-based composites. *Computational Materials Science*, 29(1):1–11, 2004.

[44] PK Valavala and GM Odegard. Modeling techniques for determination of mechanical properties of polymer nanocomposites. *Reviews on Advanced Materials Science*, 9(1):34–44, 2005.

[45] K. D. Sen. Reviews of modern quantum chemistry : a celebration of the contributions of robert g. parr. 2002.

[46] Thomas C Clancy, Sarah-Jane V Frankland, Jeffrey A Hinkley, and Thomas S Gates. Multiscale modeling of thermal conductivity of polymer/carbon nanocomposites. *International Journal of Thermal Sciences*, 49(9):1555–1560, 2010.

[47] Hongyu Tang, Huaiyu Ye, Xianping Chen, Xuejun Fan, and Guoqi Zhang. Thermal conductivity of functionalized graphene-polymer nanocomposite: A non-equilibrium molecular dynamics study. In *2017 18th International Conference on Thermal, Mechanical and Multi-Physics Simulation and Experiments in Microelectronics and Microsystems (EuroSimE)*, pages 1–5. IEEE, 2017.

[48] Roham Rafiee, Amirali Eskandariyun, Claudio Larosa, and Marco Salerno. Multi-scale modeling of polymeric composites including nanoporous fillers of milled anodic alumina. *Arabian Journal for Science and Engineering*, 47(7):8189–8198, 2022.

[49] Bohayra Mortazavi, Fatima Hassouna, Abdelghani Laachachi, Ali Rajabpour, Said Ahzi, David Chapron, Valérie Toniazzo, and David Ruch. Experimental and multiscale modeling of thermal conductivity and elastic properties of pla/expanded graphite polymer nanocomposites. *Thermochimica Acta*, 552:106–113, 2013.

[50] JB Gibson, An N Goland, M Milgram, and GoHo Vineyard. Dynamics of radiation damage. *Physical Review*, 120(4):1229, 1960.

[51] Scott J Weiner, Peter A Kollman, David A Case, U Chandra Singh, Caterina Ghio, Guliano Alagona, Salvatore Profeta, and Paul Weiner. A new force field for molecular mechanical simulation of nucleic acids and proteins. *Journal of the American Chemical Society*, 106(3):765–784, 1984.

[52] Sahar Rabet, Hamid Reza Ovesy, and Ali Ramazani. Mechanical properties and failure behavior of hexagonal boron nitride–graphene van der waals heterostructures through molecular dynamics simulation. *Preprints*, 2019.

[53] Berni J Alder and Thomas Everett Wainwright. Studies in molecular dynamics. i. general method. *The Journal of Chemical Physics*, 31(2):459–466, 1959.

[54] AJ Stone. The theory of intermolecular forces, clarendon press, 1996.

[55] Simon W de Leeuw, John W Perram, and Henrik G Petersen. Hamilton's equations for constrained dynamical systems. *Journal of statistical physics*, 61(5):1203–1222, 1990.

[56] Steven J Stuart, Alan B Tutein, and Judith A Harrison. A reactive potential for hydrocarbons with intermolecular interactions. *The Journal of chemical physics*, 112(14):6472–6486, 2000.

[57] Donald W Brenner, Olga A Shenderova, Judith A Harrison, Steven J Stuart, Boris Ni, and Susan B Sinnott. A second-generation reactive empirical bond order (rebo) potential energy expression for hydrocarbons. *Journal of Physics: Condensed Matter*, 14(4):783, 2002.

[58] Murray S Daw and Michael I Baskes. Embedded-atom method: Derivation and application to impurities, surfaces, and other defects in metals. *Physical Review B*, 29(12):6443, 1984.

[59] Steve Plimpton. Fast parallel algorithms for short-range molecular dynamics. *Journal of computational physics*, 117(1):1–19, 1995.

[60] Wenbin Yu. A unified theory for constitutive modeling of composites. *Journal of Mechanics of Materials and Structures*, 11(4):379–411, 2016.

[61] Wenbin Yu, Dewey H Hodges, and Jimmy C Ho. Variational asymptotic beam sectional analysis–an updated version. *International Journal of Engineering Science*, 59:40–64, 2012.

[62] Wenbin Yu and Dewey H Hodges. Asymptotic approach for thermoelastic analysis of laminated composite plates. *Journal of Engineering Mechanics*, 130(5):531–540, 2004.

[63] Alberto Garcia De Miguel, Alfonso Pagani, W Yu, and Erasmo Carrera. Micromechanics of periodically heterogeneous materials using higher-order beam theories and the mechanics of structure genome. *Composite Structures*, 180:484–496, 2017.

[64] Erasmo Carrera, Alberto García de Miguel, and Alfonso Pagani. Micro-, meso-and macro-scale analysis of composite laminates by unified theory of structures. In *ASME International Mechanical Engineering Congress and Exposition*, volume 58448, page V009T12A060. American Society of Mechanical Engineers, 2017.

[65] E Carrera, AG de Miguel, and A Pagani. Component-wise analysis of laminated structures by hierarchical refined models with mapping features and enhanced accuracy at layer to fiber-matrix scales. *Mechanics of Advanced Materials and Structures*, 25(14):1224–1238, 2018.

[66] E. Carrera, A.G. de Miguel, and A. Pagani. Hierarchical theories of structures based on legendre polynomial expansions with finite element applications. *International Journal of Mechanical Sciences*, 120:286–300, 2017.

[67] A. Pagani, A.G. de Miguel, and E. Carrera. Cross-sectional mapping for refined beam elements with applications to shell-like structures. *Computational Mechanics*, 59(6):1031–1048, 2017.

[68] Barna Szabó, Alexander Düster, and Ernst Rank. The p-version of the finite element method. *Encyclopedia of computational mechanics*, 2004.

[69] W. Yu. A Unified Theory for Constitutive Modeling of Composites. *Journal of Mechanics of Materials and Structures*, pages 379–411, 2016.

[70] A. G. de Miguel, A. Pagani, W. Yu, and E. Carrera. Micromechanics of periodically heterogeneous materials using higher-order beam theories and the mechanics of structure genome. *Composite Structures*, 180:484–496, 2017.

[71] A. R. Sanchez-Majano, R. Masia, A. Pagani, and E. Carrera. Microscale themo-elastic analysis of composite materials by high order geometrically accurate finite elements. *Composite Structures*, 2022.

[72] Wenbin Yu and Tian Tang. Variational asymptotic method for unit cell homogenization of periodically heterogeneous materials. *International Journal of Solids and Structures*, 44(11-12):3738–3755, 2007.

[73] VL Berdichevskii. On averaging of periodic systems: Pmm vol. 41, n 6, 1977, pp. 993–1006. *Journal of Applied Mathematics and Mechanics*, 41(6):1010–1023, 1977.

[74] E. Carrera, M. Cinefra, M. Petrolo, and E. Zappino. *Finite Element Analysis of Structures through Unified Formulation*. John Wiley and Sons, Ltd, Hoboken, New Jersey, USA, 2014.

[75] Sunil Kumar, Rajesh Purohit, and MM Malik. Properties and applications of polymer matrix nano composite materials. *Materials Today: Proceedings*, 2(4-5):3704–3711, 2015.

[76] Zheng Zheng, Xianhua Zheng, Haitao Wang, and Qiangguo Du. Macroporous graphene oxide–polymer composite prepared through pickering high internal phase emulsions. *ACS applied materials & interfaces*, 5(16):7974–7982, 2013.

[77] Changgu Lee, Xiaoding Wei, Jeffrey W Kysar, and James Hone. Measurement of the elastic properties and intrinsic strength of monolayer graphene. *science*, 321(5887):385–388, 2008.

[78] Ali Vahedi, Mohammad Homayoune Sadr Lahidjani, and Saeed Shakhesi. Multiscale modeling of thermal conductivity of carbon nanotube epoxy nanocomposites. *Physica B: Condensed Matter*, 550:39–46, 2018.

[79] Long-Cheng Tang, Yan-Jun Wan, Dong Yan, Yong-Bing Pei, Li Zhao, Yi-Bao Li, Lian-Bin Wu, Jian-Xiong Jiang, and Guo-Qiao Lai. The effect of graphene dispersion on the mechanical properties of graphene/epoxy composites. *Carbon*, 60:16–27, 2013.

[80] SG Prolongo, R Moriche, M Sánchez, and A Ureña. Self-stratifying and orientation of exfoliated few-layer graphene nanoplatelets in epoxy composites. *Composites science and technology*, 85:136–141, 2013.

[81] Liang Yue, Gholamreza Pircheraghi, Seyed Ali Monemian, and Ica Manas-Zloczower. Epoxy composites with carbon nanotubes and graphene nanoplatelets–dispersion and synergy effects. *Carbon*, 78:268–278, 2014.

[82] Jun Yin, Xuemei Li, Jianxin Zhou, and Wanlin Guo. Ultralight three-dimensional boron nitride foam with ultralow permittivity and superelasticity. *Nano letters*, 13(7):3232–3236, 2013.

[83] Shervin Kabiri, Diana NH Tran, Tariq Altalhi, and Dusan Losic. Outstanding adsorption performance of graphene–carbon nanotube aerogels for continuous oil removal. *Carbon*, 80:523–533, 2014.

[84] Jiali Wang, Xueli Gao, Yuhong Wang, and Congjie Gao. Novel graphene oxide sponge synthesized by freeze-drying process for the removal of 2, 4, 6-trichlorophenol. *RSC Advances*, 4(101):57476–57482, 2014.

[85] Xiehong Cao, Yumeng Shi, Wenhui Shi, Gang Lu, Xiao Huang, Qingyu Yan, Qichun Zhang, and Hua Zhang. Preparation of novel 3d graphene networks for supercapacitor applications. *small*, 7(22):3163–3168, 2011.

[86] Karolina Olszowska, Jinbo Pang, Pawel S Wrobel, Liang Zhao, Huy Q Ta, Zhongfan Liu, Barbara Trzebicka, Alicja Bachmatiuk, and Mark H Rummeli. Three-dimensional nanostructured graphene: synthesis and energy, environmental and biomedical applications. *Synthetic Metals*, 234:53–85, 2017.

[87] Yuanqing Li, Yarjan Abdul Samad, Kyriaki Polychronopoulou, Saeed M Alhassan, and Kin Liao. Highly electrically conductive nanocomposites based on polymerinfused graphene sponges. *Scientific reports*, 4(1):1–6, 2014.

[88] Jihye Bong, Taekyung Lim, Keumyoung Seo, Cho-Ah Kwon, Ju Hyun Park, Sang Kyu Kwak, and Sanghyun Ju. Dynamic graphene filters for selective gas-water-oil separation. *Scientific reports*, 5(1):1–6, 2015.

[89] Ya Ni, Lei Chen, Kunyue Teng, Jie Shi, Xiaoming Qian, Zhiwei Xu, Xu Tian, Chuansheng Hu, and Meijun Ma. Superior mechanical properties of epoxy composites reinforced by 3d interconnected graphene skeleton. *ACS applied materials & interfaces*, 7(21):11583–11591, 2015.

[90] Yun-Hong Zhao, Ya-Fei Zhang, Shu-Lin Bai, and Xiao-Wen Yuan. Carbon fibre/graphene foam/polymer composites with enhanced mechanical and thermal properties. *Composites Part B: Engineering*, 94:102–108, 2016.

[91] Zhao Qin, Gang Seob Jung, Min Jeong Kang, and Markus J Buehler. The mechanics and design of a lightweight three-dimensional graphene assembly. *Science advances*, 3(1):e1601536, 2017.

[92] Farzin Rahmani, Sasan Nouranian, and Yee C Chiew. 3d graphene as an unconventional support material for ionic liquid membranes: Computational insights into gas separations. *Industrial & Engineering Chemistry Research*, 59(5):2203–2210, 2020.

[93] ASTM international. Standard test method for tensile properties of plastics astm d 638-03. *Annual book of ASTM standards*, 8, 2008.

[94] Lorna J Gibson and Michael F Ashby. Thermal, electrical and acoustic properties of foams. *Cellular Solids: Structure and Properties, 2nd ed.; Cambridge University Press: Cambridge, UK*, pages 283–308, 1997.

[95] Kristien Bonroy, Jean-Michel Friedt, Filip Frederix, Wim Laureyn, Steven Langerock, Andrew Campitelli, Margit Sára, Gustaaf Borghs, Bruno Goddeeris, and Paul Declerck. Realization and characterization of porous gold for increased protein coverage on acoustic sensors. *Analytical chemistry*, 76(15):4299–4306, 2004.

[96] Pierre Hirel. Atomsk: A tool for manipulating and converting atomic data files. *Computer Physics Communications*, 197:212–219, 2015.

[97] DV Howe and JE Mark. Polymer data handbook, 1999.

[98] Alexander Stukowski. Visualization and analysis of atomistic simulation data with ovito–the open visualization tool. *Modelling and Simulation in Materials Science and Engineering*, 18(1):015012, 2009.

[99] William Humphrey, Andrew Dalke, and Klaus Schulten. Vmd: visual molecular dynamics. *Journal of molecular graphics*, 14(1):33–38, 1996.

[100] OA Shenderova, DW Brenner, A Omeltchenko, X Su, and LH Yang. Atomistic modeling of the fracture of polycrystalline diamond. *Physical Review B*, 61(6):3877, 2000.

[101] Aidan P Thompson, Steven J Plimpton, and William Mattson. General formulation of pressure and stress tensor for arbitrary many-body interaction potentials under periodic boundary conditions. *The Journal of chemical physics*, 131(15):154107, 2009.

[102] Robert Floyd Sekerka. *Thermal physics: thermodynamics and statistical mechanics for scientists and engineers*. Elsevier, 2015.

[103] Runfeng Zhou, Xinyi Ma, Haoxun Li, Chengzhen Sun, and Bofeng Bai. Specific heat capacity of confined water in extremely narrow graphene nanochannels. *Frontiers in Energy Research*, page 540, 2021.

[104] Masoud H Khadem and Aaron P Wemhoff. Comparison of green–kubo and nemd heat flux formulations for thermal conductivity prediction using the tersoff potential. *Computational materials science*, 69:428–434, 2013.

[105] Florian Müller-Plathe. A simple nonequilibrium molecular dynamics method for calculating the thermal conductivity. *The Journal of chemical physics*, 106(14):6082–6085, 1997.

[106] L Lindsay and DA Broido. Optimized tersoff and brenner empirical potential parameters for lattice dynamics and phonon thermal transport in carbon nanotubes and graphene. *Physical Review B*, 81(20):205441, 2010.

[107] J Tersoff. Empirical interatomic potential for carbon, with applications to amorphous carbon. *Physical Review Letters*, 61(25):2879, 1988.

[108] Jenniffer Bustillos, Cheng Zhang, Benjamin Boesl, and Arvind Agarwal. Three-dimensional graphene foam–polymer composite with superior deicing efficiency and strength. *ACS applied materials & interfaces*, 10(5):5022–5029, 2018.

[109] H Fukushima, LT Drzal, BP Rook, and MJ Rich. Thermal conductivity of exfoliated graphite nanocomposites. *Journal of thermal analysis and calorimetry*, 85(1):235–238, 2006.

[110] Adeyinka Idowu, Benjamin Boesl, and Arvind Agarwal. 3d graphene foam-reinforced polymer composites–a review. *Carbon*, 135:52–71, 2018.

[111] Zeng Fan, Feng Gong, Son T Nguyen, and Hai M Duong. Advanced multifunctional graphene aerogel–poly (methyl methacrylate) composites: experiments and modeling. *Carbon*, 81:396–404, 2015.

[112] Jingjing Jia, Xinying Sun, Xiuyi Lin, Xi Shen, Yiu-Wing Mai, and Jang-Kyo Kim. Exceptional electrical conductivity and fracture resistance of 3d interconnected graphene foam/epoxy composites. *ACS nano*, 8(6):5774–5783, 2014.

[113] Zhenyu Wang, Xi Shen, Mohammad Akbari Garakani, Xiuyi Lin, Ying Wu, Xu Liu, Xinying Sun, and Jang-Kyo Kim. Graphene aerogel/epoxy composites with exceptional anisotropic structure and properties. *ACS applied materials & interfaces*, 7(9):5538–5549, 2015.

[114] S Faragi, A Hamedani, Gh Alahyarizadeh, A Minuchehr, M Aghaie, and B Arab. Mechanical properties of carbon nanotube-and graphene-reinforced araldite ly/aradur hy 5052 resin epoxy composites: a molecular dynamics study. *Journal of molecular modeling*, 25(7):1–12, 2019.

[115] Lev Sarkisov, Rocio Bueno-Perez, Mythili Sutharson, and David Fairen-Jimenez. Materials informatics with poreblazer v4. 0 and the csd mof database. *Chemistry of Materials*, 32(23):9849–9867, 2020.

[116] Wenzhong Bao, Feng Miao, Zhen Chen, Hang Zhang, Wanyoung Jang, Chris Dames, and Chun Ning Lau. Controlled ripple texturing of suspended graphene and ultrathin graphite membranes. *Nature nanotechnology*, 4(9):562–566, 2009.

[117] Sarita Mann, Ranjan Kumar, and VK Jindal. Negative thermal expansion of pure and doped graphene. *RSC advances*, 7(36):22378–22387, 2017.

[118] Hamid Ghasemi and Ali Rajabpour. Thermal expansion coefficient of graphene using molecular dynamics simulation: A comparative study on potential functions. In *Journal of Physics: Conference Series*, volume 785, page 012006. IOP Publishing, 2017.

[119] Tetsuya Tohei, Akihide Kuwabara, Fumiyasu Oba, and Isao Tanaka. Debye temperature and stiffness of carbon and boron nitride polymorphs from first principles calculations. *Physical Review B*, 73(6):064304, 2006.

[120] Stephan Figge, Hanno Kröncke, Detlef Hommel, and Boris M Epelbaum. Temperature dependence of the thermal expansion of aln. *Applied Physics Letters*, 94(10):101915, 2009.

[121] A.R. Sanchez-Majano, R. Masia, A. Pagani, and E. Carrera. Microscale thermo-elastic analysis of composite materials by high order geometrically accurate finite elements. *Composite Structures*, 300:116105, 2022.

[122] ID Johnston, DK McCluskey, CKL Tan, and MC Tracey. Mechanical characterization of bulk sylgard 184 for microfluidics and microengineering. *Journal of Micromechanics and Microengineering*, 24(3):035017, 2014.

[123] Guiguan Zhang, Yuli Sun, Bingkun Qian, Hang Gao, and Dunwen Zuo. Experimental study on mechanical performance of polydimethylsiloxane (pdms) at various temperatures. *Polymer Testing*, 90:106670, 2020.

[124] Dirk Willem Van Krevelen and Klaas Te Nijenhuis. *Properties of polymers: their correlation with chemical structure; their numerical estimation and prediction from additive group contributions*. Elsevier, 2009.

[125] Yun-Hong Zhao, Zhen-Kun Wu, and Shu-Lin Bai. Thermal resistance measurement of 3d graphene foam/polymer composite by laser flash analysis. *International Journal of Heat and Mass Transfer*, 101:470–475, 2016.

[126] Ke Chu, Cheng-chang Jia, and Wen-sheng Li. Effective thermal conductivity of graphene-based composites. *Applied physics letters*, 101(12):121916, 2012.

[127] Khan MF Shahil and Alexander A Balandin. Thermal properties of graphene and multilayer graphene: Applications in thermal interface materials. *Solid state communications*, 152(15):1331–1340, 2012.

[128] Alexander A Balandin. Phononics of graphene and related materials. *ACS nano*, 14(5):5170–5178, 2020.

[129] Giorgia Fugallo, Andrea Cepellotti, Lorenzo Paulatto, Michele Lazzeri, Nicola Marzari, and Francesco Mauri. Thermal conductivity of graphene and graphite: collective excitations and mean free paths. *Nano letters*, 14(11):6109–6114, 2014.

[130] Conor S Boland, Umar Khan, Gavin Ryan, Sebastian Barwich, Romina Charifou, Andrew Harvey, Claudia Backes, Zheling Li, Mauro S Ferreira, Matthias E Möbius, et al. Sensitive electromechanical sensors using viscoelastic graphene-polymer nanocomposites. *Science*, 354(6317):1257–1260, 2016.

[131] Aiping Yu, Palanisamy Ramesh, Mikhail E Itkis, Elena Bekyarova, and Robert C Haddon. Graphite nanoplatelet- epoxy composite thermal interface materials. *The Journal of Physical Chemistry C*, 111(21):7565–7569, 2007.

[132] H Liem and HS Choy. Superior thermal conductivity of polymer nanocomposites by using graphene and boron nitride as fillers. *Solid State Communications*, 163:41–45, 2013.

[133] Seema Ansari, Antonios Kelarakis, Luis Estevez, and Emmanuel P Giannelis. Oriented arrays of graphene in a polymer matrix by in situ reduction of graphite oxide nanosheets. *Small*, 6(2):205–209, 2010.

[134] Jing Kong, Zheng Bo, Huachao Yang, Jinyuan Yang, Xiaorui Shuai, Jianhua Yan, and Kefa Cen. Temperature dependence of ion diffusion coefficients in nacl electrolyte confined within graphene nanochannels. *Physical Chemistry Chemical Physics*, 19(11):7678–7688, 2017.

[135] Huan Lin, Shen Xu, Xinwei Wang, and Ning Mei. Significantly reduced thermal diffusivity of free-standing two-layer graphene in graphene foam. *Nanotechnology*, 24(41):415706, 2013.

[136] Michael Thompson Pettes, Hengxing Ji, Rodney S Ruoff, and Li Shi. Thermal transport in three-dimensional foam architectures of few-layer graphene and ultrathin graphite. *Nano letters*, 12(6):2959–2964, 2012.

[137] Man Li, Yi Sun, Huying Xiao, Xuejiao Hu, and Yanan Yue. High temperature dependence of thermal transport in graphene foam. *Nanotechnology*, 26(10):105703, 2015.

[138] Ali Vahedi and Mohammad Homayoune Sadr Lahidjani. Tunable thermal conductivity along graphene/hexagonal boron-nitride polycrystalline heterostructures. *The European Physical Journal Plus*, 132(10):1–7, 2017.

[139] Unal Degirmenci and Mesut Kirca. Reverse non-equilibrium molecular dynamics simulations on the thermal conductivity of three-dimensional graphene nano-ribbon foams. *Journal of Physics and Chemistry of Solids*, 136:109130, 2020.

[140] Tonglei Li, Dane O Kildsig, and Kinam Park. Computer simulation of molecular diffusion in amorphous polymers. *Journal of controlled release*, 48(1):57–66, 1997.

[141] Yingzhe Du, Shasha Liu, Shideng Yuan, Heng Zhang, and Shiling Yuan. A study of influence factors to improve the heat transfer of pure-polydimethylsiloxane (pdms): A molecular dynamics study. *Colloids and Surfaces A: Physicochemical and Engineering Aspects*, 618:126409, 2021.

[142] Xinfeng Zhang, Kan Kan Yeung, Zhaoli Gao, Jinkai Li, Hongye Sun, Huansu Xu, Kai Zhang, Min Zhang, Zhibo Chen, Matthew MF Yuen, et al. Exceptional thermal interface properties of a three-dimensional graphene foam. *Carbon*, 66:201–209, 2014.

[143] S. Khosravani, M. H. Sadr, E. Carrera, A. Pagani, and A. R. Sanchez-Majano. Multi-scale analysis of thermoelastic properties of graphene foam/PDMS composites. *Computational Materials Science*, 216:111842, 2023.

[144] Yun-Hong Zhao, Ya-Fei Zhang, Zhen-Kun Wu, and Shu-Lin Bai. Synergic enhancement of thermal properties of polymer composites by graphene foam and carbon black. *Composites Part B: Engineering*, 84:52–58, 2016.

[145] Chin-Teh Sun and Rajesh S Vaidya. Prediction of composite properties from a representative volume element. *Composites science and Technology*, 56(2):171–179, 1996.

[146] Haoming Fang, Yunhong Zhao, Yafei Zhang, Yanjuan Ren, and Shu-Lin Bai. Three-dimensional graphene foam-filled elastomer composites with high thermal and mechanical properties. *ACS Applied Materials & Interfaces*, 9(31):26447–26459, 2017.